TECHNISCHE UNIVERSITÄT
BERGAKADEMIE FREIBERG
The University of Resources. Since 1765.

Institut
Experimentelle
Physik

Applications of resonant hard x-ray diffraction for characterization of structural modifications in crystals

By the Faculty of Chemistry and Physics
of the Technische Universität Bergakademie Freiberg

approved

Thesis

to attain the academic degree of

Doktor der Naturwissenschaften
(Dr. rer. nat.)

submitted by **Dipl.-Phys. Carsten Richter**

born on the 14th of July, 1984 in Wurzen

Assessor: Prof. Dr. Dirk C. Meyer
Prof. Dr. Vladimir E. Dmitrienko

Date of the award: Freiberg, April 12th, 2017

Versicherung

Hiermit versichere ich, dass ich die vorliegende Arbeit ohne unzulässige Hilfe Dritter und ohne Benutzung anderer als der angegebenen Hilfsmittel angefertigt habe; die aus fremden Quellen direkt oder indirekt übernommenen Gedanken sind als solche kenntlich gemacht.

Die Hilfe eines Promotionsberaters habe ich nicht in Anspruch genommen. Weitere Personen haben von mir keine geldwerten Leistungen für Arbeiten erhalten, die nicht als solche kenntlich gemacht worden sind. Die Arbeit wurde bisher weder im Inland noch im Ausland in gleicher oder ähnlicher Form einer anderen Prüfungsbehörde vorgelegt.

12. April 2017 Dipl.-Phys. Carsten Richter

Declaration

I hereby declare that I completed this work without any improper help from a third party and without using any aids other than those cited. All ideas derived directly or indirectly from other sources are identified as such.

I did not seek the help of a professional doctorate-consultant. Only those persons identified as having done so received any financial payment from me for any work done for me. This thesis has not previously been published in the same or a similar form in Germany or abroad.

April 12^{th}, 2017 Dipl.-Phys. Carsten Richter

Contents

Statements of the thesis (Abstract)

Resonant x-ray diffraction provides a very diverse set of techniques that represent unique keys for solving problems of crystal structure analysis in materials science. This is based on a combination of the advantages of diffraction and spectroscopic methods.

The *diffraction anomalous fine structure* (DAFS) method allows to characterize the local structure of the selected element separately for different crystallographic phases as well as for ordered and disordered fractions in a material. The application of DAFS on polycrystalline samples has been developed further in the course of this work. The phase problem in diffraction is solved for DAFS based on the knowledge of the asymptotic behavior of x-ray scattering far from absorption edges and using the recently proposed *logarithmic dispersion relations* (LDR). Although there are high demands on experimental setup and data quality, DAFS represents a reliable procedure.

The technique has been applied to refine the crystal structure of the recently synthesized layered hydrazinium titanate (LHT) – a new advanced reductive adsorbent. It has been found that the published structure model needs improvement: it does not explain the appearance of 5-fold titanium coordination geometry as well as a short Ti=O titanyl bond which have been determined using DAFS. This also may explain the titanium deficiency resulting from previous structure refinement.

The adsorption of foreign atoms into the structure of LHT has been studied with resonant diffraction on the example of selenium. An analysis of the energy dependence of several Bragg reflections at the selenium edge allowed the determination of the selenium position after intercalation.

A new method of crystal structure analysis has been presented which is based on resonant suppression of Bragg diffraction (RSD) through variation of the photon energy near an absorption edge. The obtained destructive interference is highly sensitive to slight variations of the internal structural parameters. The method has been formulated within this work for the first time and goes beyond the analyses of energy profiles of Bragg intensity that were presented in literature before.

The RSD technique can be used to precisely quantify thermal motion induced atomic displace-

ment using few reflections. An application to a well understood test system – cubic strontium titanate ($SrTiO_3$) – yields anisotropic atomic displacement parameters that are very close to literature values. This proves the suitability of the new method.

Certain regions in single crystals of cubic strontium titanate undergo a structural transition under influence of an external electric field. The new structure corresponds to the lead titanate ($PbTiO_3$) type and the atomic positions have been resolved with a precision of $\approx 1\,\mathrm{pm}$ using the RSD method. These results explain the observation of new polar properties in the crystals such as piezoelectricity and pyroelectricity.

The breaking of Friedel's law based on resonant dispersion provides access to the determination the absolute polarization state of polar materials. An observation of the Friedel contrast as a function of time allows characterization of dynamics of polarization switching or domain wall propagation. An application of both techniques to ultra thin, epitaxial $BaTiO_3$ layers has been demonstrated in this work.

In *anisotropy in anomalous scattering* (AAS), the wavevector and polarization dependence in resonant x-ray diffraction is considered. This may lead to the violation of crystallographic selection rules and therefore to the appearance of "forbidden" reflections. These only exist in a small energy range and, in certain cases, are especially sensitive to thermal vibrations and point defects. This is based on an atomic displacement correlated with the defects and results in an additional dependence on wavevectors and therefore in a reduction of symmetry.

The sensitivity of AAS to local distortions can been utilized to characterize the local geometry of transient hydrogen configurations in hydrogen bonded crystals. The spectral shape of forbidden reflections can be analyzed to assess the origin of the various contributions. This allowed to conclude the occurence of nonpolar, "Slater"-type hydrogen configurations in rubidium dihydrogen phosphate RbH_2PO_4.

Thesen der Arbeit (Kurzfassung)

Resonante Röntgenbeugung ermöglicht eine sehr vielfältige Reihe von Messverfahren welche einzigartige Lösungsansätze für Kristallstrukturanalyse in der Materialwissenschaft darstellen. Diese beruhen auf einer Kombination der Vorteile aus Beugungs- und Spektroskopiemethoden.

Die Methode der *diffraction anomalous fine structure* (DAFS) ermöglicht eine gesonderte Untersuchung der lokalen Struktur eines gewählten Elements vorliegend in verschiedenen kristallographischen Phasen oder aber in geordneten und ungeordneten Bereichen des Materials. Der Einsatz von DAFS für die Untersuchung polykristalliner Proben wurde im Rahmen dieser Arbeit weiterentwickelt. Dabei wird das Phasenproblem der Beugung für DAFS basierend auf der Kenntnis des asymptotischen Verhaltens der Röntgenstreuung fernab von Absorptionskanten sowie unter Nutzung der jüngst vorgeschlagenen logarithmischen Dispersionsrelationen gelöst. Obwohl hohe Anforderungen an den experimentellen Aufbau sowie an die Datenqualität bestehen, stellt DAFS ein verlässliches Methode dar.

Die Methode wurde eingesetzt um die Kristallstruktur eines vor Kurzem synthetisierten Hydrazinium-Schichttitanats (LHT) zu verfeinern, ein neues Material mit ausgezeichneten Reduktions- und Adsorptionseigenschaften. So wurde gezeigt, dass das veröffentlichte Strukturmodell einer Erweiterung bedarf, da es die fünffache TiO_5 Koordinationen sowie Titanylgruppen (Ti=O), welche mittels DAFS beobachtet wurde, nicht beschreibt. Dies ist auch eine mögliche Erklärung für die geringe Belegung der Titanlage welche Resultat vorausgegangener Strukturuntersuchungen war.

Ferner wurde die Einlagerung von Fremdatomen in die Struktur von LHT am Beispiel von Selen mittels resonanter Röntgenbeugung untersucht. Anhand der Analyse der Energieabhängigkeiten mehrerer Bragg-Reflexe nahe der Selen-Absorptionskante konnten die bevorzugten Positionen des eingelagerten Selenatoms bezüglich des LHT Gitters bestimmt werden.

Eine neue Methode der Kristallstrukturanalyse, basierend auf resonanter Unterdrückung von Beugungsintensität (RSD) durch gezieltes Variieren der Energie der Röntgenstrahlung nahe einer Absorptionskante, wurde vorgestellt. Die dadurch realisierte destruktive Interferenz ist äußerst sensitiv auf kleinste Änderungen interner Strukturparameter, die so charakter-

isiert werden können. Die Methode wurde in dieser Arbeit erstmalig ausgearbeitet und geht über bisherige, in der Literatur dokumentierte, Untersuchungen energieabhängiger Bragg-Intensitäten hinaus.

Das RSD Messverfahren kann, basierend auf der Vermessung weniger Reflexe, zur präzisen Bestimmung thermischer Auslenkung von Atomen aus ihrer Ruhelage eingesetzt werden. Die Anwendung auf ein gut verstandenes Testsystem – kubisches Strontiumtitanat – liefert anisotrope atomare Auslenkungsparameter welche nahe an den Literaturwerten liegen. Dies zeigt die Eignung der neuen Methode.

Gewisse Gebiete in Strontiumtitanat-Einkristallen erfahren eine strukturelle Umwandlung bei dauerhafter Einwirkung eines externen, elektrischen Felds. Die sich dabei ergebende Kristallstruktur ist vom Bleititanat-Typ und die neuen Atompositionen konnten mithilfe der RSD Methode auf $\approx 1\,\mathrm{pm}$ genau bestimmt werden. Diese Ergebnisse erklären außerdem das Auftreten neuer physikalischer Eigenschaften in den Einkristallen wie Piezoelektrizität und Pyroelektrizität.

Die Verletzung des Friedelschen Gesetzes durch resonante Anregung gibt Zugang zur Bestimmung der absoluten (strukturellen) Polarisation polarer Materialien. Eine Messung des Friedel-Kontrasts als Funktion der Zeit ermöglicht die Untersuchung von Umschaltdynamiken oder der Ausbreitung von Domänengrenzen. Die Möglichkeit der Anwendung dieser Verfahren auf ultradünne, epitaktische $BaTiO_3$ Filme wurde in dieser Arbeit aufgezeigt.

Im Rahmen der *anisotropy in anomalous scattering* (AAS) muss die Abhängigkeit der resonanten Röntgenbeugung von Wellenzahlvektor und Polarisation der Röntgenstrahlung beachtet werden. Dies kann zur Verletzung kristallographischer Auslöschungsregeln und dem damit verbundenen Auftreten von „verbotenen“ Reflexen führen. Diese existieren nur in einem schmalen Energiebereich und sind in manchen Fällen besonders empfindlich auf thermische Anregung und Punktdefekte. Dies basiert auf einer korrelierten Auslenkung der Atome wodurch eine zusätzliche Abhängigkeit des Streuvorgangs von den Wellenzahlvektoren entsteht und damit zu einer verringerten Symmetrie führt.

Die Empfindlichkeit der AAS auf lokale Strukturabweichungen kann eingesetzt werden um vorübergehende Wasserstoffkonfigurationen in wasserstoffverbrückten Molekülkristallen zu untersuchen. Eine Analyse der Spektren verbotener Reflexe kann Aufschluss über den Ursprung verschiedener Beiträge liefern. Auf diesem Wege konnten nichtpolare Wasserstoffkonfigurationen vom „Slater“-Typ in Rubidiumdihydrogenphosphat (RbH_2PO_4) nachgewiesen werden.

1. Introduction

Most of the advances in technology of the past decades relied on the development of new, functional materials. Some of these technologies had an enormous impact on our society. Examples include modern electronic devices like computer chips and data storage but also the progress in superconducting materials, alloys and polymers. Knowing the structure of materials enables the understanding of their production and their processing. The structure also defines the properties of materials. Therefore, a modification of the structure may, in turn, allow material engineering to optimize the performance of these properties. In many cases, the average structure of a material cannot explain its characteristics. Obvious examples are resistance in doped semiconductors, light emitting diodes or mechanic properties of alloys. Therefore studies of structural modifications or deviations are necessary to explain the interesting phenomena. This can involve a local characterization using small probes but also averaging methods that are solely sensitive to interesting fractions of the sample.

Many of the functional materials exist in a crystalline form, e. g. superconductors, magnets, ceramics, alloys, etc. These show a high degree of order in the atomic arrangement on very large length scales. The order can lead to a strong coupling of the material with external fields (e. g. electric, magnetic, strain). The response to the external influences is defined by the symmetry of the arrangement or rather of the crystal structure. Often a strong response is only observed for certain orientations of the crystal which is due to a low symmetry and the consequential anisotropy. Therefore, even small structural changes can lead to a reduced symmetry that gives rise to new or enhanced physical properties of a crystalline material.

The study of crystal structure is nowadays carried out by means of a large set of different techniques using different probes. However, x-rays have been the first probe that was used for crystal structure analysis and x-ray diffraction is still amongst the most popular methods today. This is due to the relatively easy generation of x-rays, their ability to penetrate through matter, their typical wavelength matching atomic distances, etc.

This thesis will outline and extend the opportunities which are gained in the field of x-ray diffraction by adjusting the x-ray energy to excite electronic resonances. This *resonant* diffraction forms the basis for a variety of new techniques that shall be placed in historic and scientific context here. Later, a description of own developments and examples of applications will follow.

1.1. Development of resonant x-ray diffraction

Without doubt, the diffraction of x-rays from ordered crystals, as it was discovered by Laue in 1913 [FKL13], formed the basis for crystal structure analysis in the last century and remains one of the most important tools in materials science, chemistry and biology to date. X-rays are unique for the characterization of atomic structure of matter not only because their wavelength is in the range of typical interatomic distances. The fact that their energy range covers the binding energies of core level electrons for almost all chemical elements makes x-rays very attractive for spectroscopy and allows *resonant x-ray diffraction* (RXD) experiments where the scattering characteristics of selected elements are modified due to electronic transitions. This way the scattering process grows in complexity but also opens the door to new research fields. However, a long time has passed before scientists started to explore these fields. The reason can be found in the low intensity of x-rays as they were generated by an electron beam hitting a target (*Bremsstrahlung*) after their discovery by Röntgen [Rön98]. The situation was improved by using x-ray emission lines with an energy characteristic for each element in the target (anode). This provided an order of magnitude higher intensities in the corresponding energy intervals. The drawback of this approach was that the x-ray energy is fixed to a certain value depending on which target metal is used. Hence, resonant x-ray experiments were exotic for a long time.

Nevertheless, already in 1920, a first comprehensive x-ray spectroscopy of core electrons was carried out by Fricke [Fri20] on a series of elements ranging from magnesium to chromium. If the x-ray energy is close to the binding energy of an electron (*i.e.* at resonance), the absorption spectra exhibit pronounced features which are referred to as *fine structure*. They are characteristic for the local structure – bond distances and coordination geometry – of the atom which is resonantly excited. Moreover, the sudden increase of absorption, that can typically be observed when the photon energy is increased over such resonance, is usually called *absorption edge*. In the following years, diffraction experiments under resonant conditions were merely limited to the study of x-rays [MS25] themselves. The first application of resonant x-ray diffraction for crystal structure analysis was the determination of the "side" or polarity of the 111 faces of zincblende by Coster in 1930 [CKP30]. It was based on complex corrections for the atomic scattering amplitude which are necessary due to absorption effects and cause a breaking of Friedel's law [Fri13][1]. These corrections are never zero but are only very strong near absorption edges. About 20 years later, Bijvoet pointed out how to use this effect to determine the absolute configuration of molecules as well as to solve the phase problem of crystallography [BPB51]. The latter result laid the foundation for direct crystal structure determination from diffraction data even for large molecules – a method developed in the

[1] Friedels law states that the intensity of opposing reflections is equal and is based on the Fourier transform of real quantities which does only change in phase after inversion.

early 1980s [HT81; Arn+82] and later referred to as *multi-wavelength anomalous dispersion* (MAD). It is probably the method among resonant x-ray diffraction techniques that has the highest impact on modern society.

In parallel, another branch of resonant diffraction was formed on the basis of fine structure oscillations which were observed in the intensity of x-ray reflections for the first time by Cauchois [Cau56] on a mica crystal. As in the above mentioned absorption spectroscopy, these oscillations occur in the vicinity of an absorption edge of a selected atom and depend on the local structure. However, using the diffracted intensity for interpretation yields information only of those resonant atoms which are present in a certain spatial periodicity that is defined by the reflection. Hence, it allows to separately study atoms occupying different crystallographic sites. This method will later be named *diffraction anomalous fine structure* (DAFS). The two fields of resonant x-ray diffraction that emerged last are *resonant magnetic scattering* (RMS) and *anisotropy in anomalous scattering* (AAS). Both are based not only on the energy dependence of the x-rays but on their full state including wavevector and polarization. The major difference is that the former method describes the scattering by magnetic moments (spin and orbital) while the latter is focused on scattering by charge. Brunel and de Bergevin presented a thorough description and first experimental data on RMS which was observed through the appearance of additional, "magnetic" reflections [BB72; BB81] allowing to study the magnetic structure. The wavevector and polarization dependence (*i.e.* anisotropy) of charge scattering can only be observed in a very narrow energy region near the absorption edge. It can lead to a violation of certain selection rules for x-ray reflections and, hence, also give rise to additional, so called "forbidden" reflections. These provide an access to study exclusively the anisotropic part of charge density (e. g. spherical harmonics). These reflections are, in contrast to magnetic scattering, strictly related to the crystallographic lattice and fulfill all symmetry restrictions of the space group when taking the anisotropy into account. Forbidden reflections have been predicted by Dmitrienko in 1983 [Dmi83] and observed on sodium bromate at the bromine K edge two years later by Templeton and Templeton [TT85].

Certainly, the development of all the described resonant x-ray methods would not have been possible without the invention of new sources for x-rays. Laboratory sources based on characteristic radiation from metal anodes where usually used at a fixed wavelength. The flux could be increased an order of magnitude by using rotating anodes which tolerate a higher heat load caused by the electrons. However, a significant leap in the development of new sources was only possible with the discovery of synchrotron radiation at the General Electric Research Laboratory in 1947. It is emitted when highly energetic, charged particles are accelerated perpendicular to the direction of movement. Therefore, it could be observed at synchrotrons and later at storage rings. The parasitic use of synchrotron radiation started in the early 1960s (at DESY 1966). About ten years later, the first storage rings dedicated and designed

for the use of synchrotron radiation have been constructed. Already then, the brilliance – a measure of flux density per solid angle and energy interval – has been increased by over 7 orders of magnitude compared to conventional x-ray sources. A trend which has continued ever since.

1.2. Outline of the thesis

The thesis will start with a detailed introduction into the theoretical foundations of RXD focused on the study of crystallographic charge density. This will contain the basic interactions of photons and matter and proceed with the specific case of x-ray diffraction from crystals. Different approximations for the scattering behavior will be outlined. In Section 3, practical aspects of x-ray diffraction measurements and data interpretation are discussed. This includes the description of x-ray sources and experimental end stations as well as the algorithms for data correction and modeling. Finally, applications on different kinds of material classes – polycrystals, thin films and singlecrystals – will be presented in Section 4. There, methodological developments of this work as well as results of structure refinement will be described. This also includes practical details of the experiments and data interpretation specific for each applied RXD method.

2. Basics of resonant x-ray diffraction

2.1. Interaction of photons and matter

In order to understand the basic principles of RXD, one has to have a look into the two different fields which it is comprised of – x-ray spectroscopy and elastic x-ray scattering. Diffraction is, in this sense, a branch of elastic scattering where interference of the scattered waves becomes significant. The underlying process for both cases is the scattering of photons on charged particles. We will see in the following that the scattering probability is proportional to the inverse square of the charged particle's mass. Therefore and because the electron is the least massive charged particle, the calculations are focused on the scattering by electrons in most cases and also within this work. A quite general and yet concise quantum mechanical derivation of the cross section was published by Blume [Blu94; Blu85] for scattering of photons on nonrelativistic charged particles taking into account magnetic effects. The essence of this formalism will be outlined in the following whereas a classical description of x-ray scattering can be found in [Jac99; Ric10].

2.1.1. Scattering of a photon by a bound electron

Within the second quantization, the Hamiltonian for a system consisting of an electron and a photon can be decomposed into a sum of three terms describing the energy of the electron (0), the radiation (R) and their interaction (int):

$$\mathscr{H} = \mathscr{H}_0 + \mathscr{H}_\mathrm{R} + \mathscr{H}_\mathrm{int}. \tag{2.1}$$

If one considers $\mathscr{H}_\mathrm{int}$ a small perturbation, the new eigenstates as well as transition amplitudes can be developed in terms of orders of $\mathscr{H}_\mathrm{int}$. Therefore, we shall have a closer look at it. Let $\mathbf{A}$ be the vector potential of the photon, $\mathbf{s}$ the spin and $\mathbf{p}$ the momentum of the electron. Then the interaction part is locally (at position $\mathbf{r}$) given as

$$\mathscr{H}_\mathrm{int} = \underbrace{\frac{e^2}{2m}\mathbf{A}^2(\mathbf{r})}_{\mathscr{H}_1} - \underbrace{\frac{e}{m}\mathbf{A}(\mathbf{r})\cdot\mathbf{p}}_{\mathscr{H}_2} - \underbrace{\frac{e\hbar}{m}\mathbf{s}\cdot[\nabla\times\mathbf{A}(\mathbf{r})]}_{\mathscr{H}_3} - \underbrace{\frac{e^2\hbar}{2m^2c^2}\mathbf{s}\cdot\left[\dot{\mathbf{A}}(\mathbf{r})\times\mathbf{A}(\mathbf{r})\right]}_{\mathscr{H}_4}. \tag{2.2}$$

We will see that the magnetic scattering contribution will be produces by the latter two terms being proportional to the spin. The vector potential of the quantized field of a photon confined to a volume V can be written as a Fourier series [Sch07]

$$\mathbf{A}(\mathbf{r}) = \sum_{\mathbf{k},\zeta=1,2} \sqrt{\frac{2\pi\hbar}{ckV}} \left(c_{\mathbf{k},\zeta} \boldsymbol{\varepsilon}_{\mathbf{k},\zeta} \mathrm{e}^{\mathrm{i}\mathbf{k}\mathbf{r}} + c^{\dagger}_{\mathbf{k},\zeta} \boldsymbol{\varepsilon}^{*}_{\mathbf{k},\zeta} \mathrm{e}^{-\mathrm{i}\mathbf{k}\mathbf{r}} \right), \tag{2.3}$$

where $c^{\dagger}_{\mathbf{k},\zeta}$ and $c_{\mathbf{k},\zeta}$ are the creation and annihilation operator for the photon mode $(\mathbf{k},\zeta)$, respectively and the polarization vectors $\boldsymbol{\varepsilon}$ are defined according to the Jones formalism [Jon41]: since they are perpendicular to the wavevector $\mathbf{k}$ and normalized the only degree of freedom is the rotation around $\mathbf{k}$. Therefore, they are usually parameterized into a component perpendicular ($\zeta = \sigma$) or parallel ($\zeta = \pi$) to the scattering plane which is spanned by both wavevectors (see Fig. 2.2). If these components are weighted with a complex number, they undergo a phaseshift resulting in elliptical or circular polarization. In quantization, the vector field described in Eq. (2.3) represents either the creation of a photon or the annihilation of the corresponding, existing antiphoton. The scattering process, on the other hand, naturally involves the annihilation as well as the creation of another photon. From Eq. 2.3, it is now clear that only perturbation terms which are quadratic in the vector potential can give rise to scattering. The transition rate according to second order perturbation theory from state $|i\rangle$ to state $|f\rangle$ takes the form

$$W_{i\to f} = \frac{2\pi}{\hbar} \left| \langle f| \mathscr{H}_{\mathrm{int}} |i\rangle + \sum_{n} \frac{\langle f| \mathscr{H}_{\mathrm{int}} |n\rangle \langle n| \mathscr{H}_{\mathrm{int}} |i\rangle}{E_i - E_n} \right|^2 \cdot \delta(E_i - E_f), \tag{2.4}$$

where E_ξ denotes the energy of state $|\xi\rangle$ and the sum only includes unoccupied states $|n\rangle$ due to the Pauli exclusion principle. Here, we can see that only the interaction terms $\mathscr{H}_1$ and $\mathscr{H}_4$ (quadratic in $\mathbf{A}$) can give rise to scattering within the 1$^{\mathrm{st}}$ order perturbation whereas the terms $\mathscr{H}_2$ and $\mathscr{H}_3$ (linear in $\mathbf{A}$) will only contribute to scattering within the 2$^{\mathrm{nd}}$ order – the part which is enhanced under resonant conditions. Also, we can already conclude with help of Eq. (2.3) that there will be two different resonant scattering processes. Depending on the order of annihilation and creation operators, a photon will either first be absorbed followed by the emission of another photon or vice versa. Certainly, the scattering process is coherent and the virtual intermediate state cannot be observed, but the participating energy levels will be different. The Feynman diagrams for the perturbations up to second order are shown in Fig. 2.1 for those matrix elements which yield scattering. Before looking at the explicit forms of matrix elements, let us consider the following special case of the above. The initial and final states are the many particle wave function including the electron as well as the photon. Only interference of elastically scattered photons shall take part in diffraction which is why we assume the initial and the final state of the electron to be the same (the photon energy will be unchanged as a result). This way we obtain

$$\begin{aligned} |i\rangle &= |a, \mathbf{k}\zeta\rangle \\ |f\rangle &= |b, \mathbf{k}'\zeta'\rangle \stackrel{!}{=} |a, \mathbf{k}'\zeta'\rangle . \end{aligned} \tag{2.5}$$

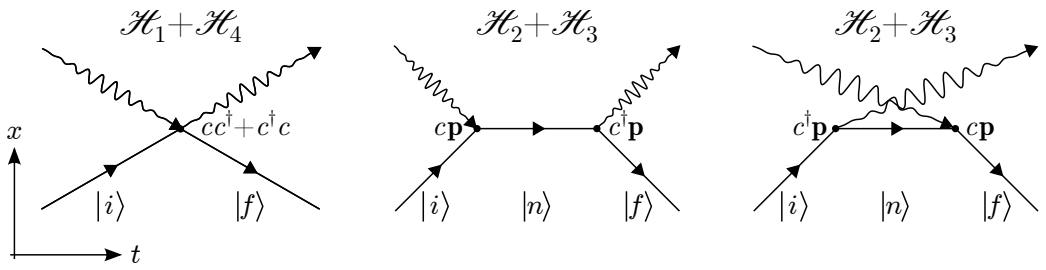

Fig. 2.1.: Feynman diagrams for photon scattering from charged particles obtained from perturbation theory up to second order.

For the energies, we get that $E_i = E_f = E_a + \hbar\omega$ where ω is the angular frequency of the x-rays and $|\mathbf{k}| = |\mathbf{k}'| = \omega/c =: k$. This way, the time dependent phase factor in the equations for time dependent perturbation theory up to second order can be dropped [Sch07]. By insertion of $\mathscr{H}_1 + \mathscr{H}_4$ into the first order term and $\mathscr{H}_2 + \mathscr{H}_3$ into the second order term and neglecting those parts which don't result in annihilation as well as creation of a photon (i.e. are not proportional to $\mathbf{c}^\dagger$ and $\mathbf{c}$), we obtain the scattering amplitude for the special case of *resonant elastic x-ray scattering* (REXS) as

$$w_{if}^{1+2}(\boldsymbol{\varepsilon}, \boldsymbol{\varepsilon}', \mathbf{k}, \mathbf{k}', \hbar\omega) = -\frac{e^2}{mc^2}\Bigg(\langle a|\, \mathrm{e}^{\mathrm{i}\mathbf{K}\mathbf{r}}\, |a\rangle\, \boldsymbol{\varepsilon}'^{*} \cdot \boldsymbol{\varepsilon} \tag{2.6}$$

$$-\mathrm{i}\frac{\hbar\omega}{mc^2}\, \langle a|\, \mathbf{s} \cdot \mathrm{e}^{\mathrm{i}\mathbf{K}\mathbf{r}}\, |a\rangle \cdot \boldsymbol{\varepsilon}'^{*} \times \boldsymbol{\varepsilon} \tag{2.7}$$

$$+\frac{1}{m}\sum_n \Bigg\{ \frac{\langle a|\, \boldsymbol{\varepsilon}'^{*} \cdot \mathbf{O}^\dagger(\mathbf{k}')\, |n\rangle\, \langle n|\, \boldsymbol{\varepsilon} \cdot \mathbf{O}(\mathbf{k})\, |a\rangle}{E_a - E_n + \hbar\omega - \mathrm{i}\Gamma/2} \tag{2.8}$$

$$+ \frac{\langle a|\, \boldsymbol{\varepsilon} \cdot \mathbf{O}(\mathbf{k})\, |n\rangle\, \langle n|\, \boldsymbol{\varepsilon}'^{*} \cdot \mathbf{O}^\dagger(\mathbf{k}')\, |a\rangle}{E_a - E_n - \hbar\omega + \mathrm{i}\Gamma/2} \Bigg\} \Bigg) \tag{2.9}$$

where $\mathbf{K} = \mathbf{k} - \mathbf{k}'$ is the wavevector transfer and the perturbation operator was defined as

$$\mathbf{O}(k) = \mathrm{e}^{\mathrm{i}\mathbf{k}\mathbf{r}}\left[\mathbf{p} - \mathrm{i}\hbar(\mathbf{k} \times \mathbf{s})\right]. \tag{2.10}$$

Here the annihilation and creation operators have been replaced with their eigenvalues. The equations (2.6...2.9) describe most x-ray scattering phenomena. To take into account inelastic scattering, initial and final electron states need to be distinguished including additional terms for energy conservation. The first two terms, (2.6) and (2.7), contain the nonresonant charge (Thomson) and magnetic scattering, respectively, and are proportional to the corresponding Fourier transform. One can see that the nonresonant magnetic contribution is weaker (in amplitude) by a factor equal to the energy ratio of the x-ray probe to that of the electron. The resonant scattering parts are found in the latter two terms (2.8) and (2.9). They are enhanced when the photon energy $\hbar\omega$ is close to the transition energy of two states ($|a\rangle$ and $|n\rangle$), since the denominator becomes very small. To avoid this fraction to diverge, the term $-\mathrm{i}\Gamma/2$ is added to $\hbar\omega$ which is taking into account the limited life time of the electron levels and the corresponding core level width. It is on the order of 1 eV for hard x-rays. The essence

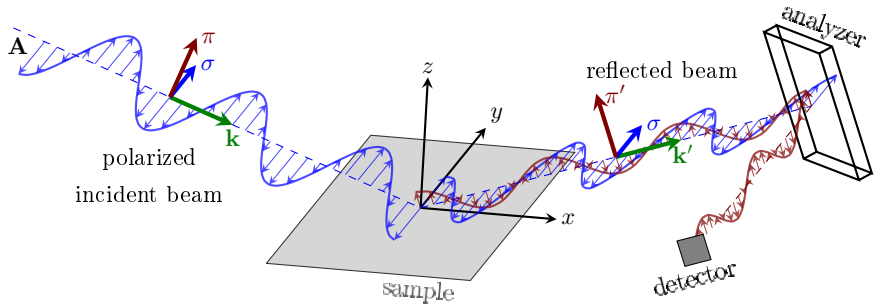

Fig. 2.2.: The scattering geometry. Incident and scattered waves can carry σ and π components of polarization both being perpendicular to the corresponding wavevector. The σ component points by definition in the same direction before and after scattering. Here the incident beam was chosen to be linearly (σ) polarized. A π component can be observed after scattering and filtered out using an analyzer. The incident and scattered waves are nearly out of phase in x-ray scattering. An analyzer can be realized via additional scattering in the plane perpendicular to the polarization of interest by $90\,^\circ$. This relies on the dominant scattering term which is proportional to the scalar product of polarizations ($\propto \boldsymbol{\varepsilon}'^{*} \cdot \boldsymbol{\varepsilon}$).

of resonant scattering is defined by the term (2.8), since it is large when the photon energy approximates the energy difference between initial and an intermediate, unoccupied state $|n\rangle$ which is higher in energy. The last term (2.9), on the other hand, is only resonant in the opposite case – if a considerable fraction of electrons is in the excited state (population inversion). Since this is practically never satisfied, the last term is usually treated as an additional nonresonant contribution, in particular for magnetic scattering. It's important to note that resonant scattering depends on the wavevectors and polarization states of both incident and scattered wave whereas nonresonant scattering is only scaled by the scalar product of polarization vectors. Far from an absorption edge, however, the sum over n results in an average over complete atomic subshells and, hence, is isotropic. Only the resonance like energy dependence remains. This is why resonant contributions are taken account of by a scalar correction in most cases of x-ray scattering. Fig. 2.2 illustrates the basic resonant scattering experiment including the polarization dependence.

2.1.2. Optical theorem

Considering only forward scattering ($\mathbf{O}(\mathbf{k}) = \mathbf{O}(\mathbf{k}')$ and $\boldsymbol{\varepsilon}' = \boldsymbol{\varepsilon}$), the matrix elements for creation and annihilation of the photon are the same and, hence, the third and fourth part (Eqs. (2.8,2.9)) can be combined the following way:

$$\begin{aligned}
&\frac{1}{m}\sum_n \left\{ \frac{\langle a|\, \boldsymbol{\varepsilon}^* \cdot \mathbf{O}^\dagger(\mathbf{k})\, |n\rangle \langle n|\, \boldsymbol{\varepsilon} \cdot \mathbf{O}(\mathbf{k})\, |a\rangle}{E_a - E_n + \hbar\omega - \mathrm{i}\Gamma/2} + \frac{\langle a|\, \boldsymbol{\varepsilon} \cdot \mathbf{O}(\mathbf{k})\, |n\rangle \langle n|\, \boldsymbol{\varepsilon}^* \cdot \mathbf{O}^\dagger(\mathbf{k})\, |a\rangle}{E_a - E_n - \hbar\omega + \mathrm{i}\Gamma/2} \right\} \\
&= \frac{1}{m}\sum_n \left\{ |\, \langle n|\, \boldsymbol{\varepsilon} \cdot \mathbf{O}(\mathbf{k})\, |a\rangle\, |^2 \frac{1}{E_a - E_n + \hbar\omega - \mathrm{i}\Gamma/2} + \frac{1}{E_a - E_n - \hbar\omega + \mathrm{i}\Gamma/2} \right\} \\
&= \frac{1}{m}\sum_n |\, \langle n|\, \boldsymbol{\varepsilon} \cdot \mathbf{O}(\mathbf{k})\, |a\rangle\, |^2 \frac{2(E_a - E_n)}{(E_a - E_n)^2 - (\hbar\omega - \mathrm{i}\Gamma/2)^2}
\end{aligned}$$

In forward scattering, this term alone contributes an imaginary part to the scattering amplitude. For small Γ, this imaginary part converges to

$$\operatorname{Im} w_{if}^{1+2}(\boldsymbol{\varepsilon} = \boldsymbol{\varepsilon}', \mathbf{k} = \mathbf{k}', \hbar\omega) \xrightarrow{\Gamma \to 0} \frac{\pi e^2}{m^2 c^2} \sum_n |\, \langle n|\, \boldsymbol{\varepsilon} \cdot \mathbf{O}(\mathbf{k})\, |a\rangle\, |^2 \delta(E_a + \hbar\omega - E_n). \tag{2.11}$$

One can see that the result is closely related to the transition rate of photoabsorption (*cf.* Eq. 2.4) which can be obtained from the annihilation parts of $\mathscr{H}_2$ and $\mathscr{H}_3$ (which reduce $|i\rangle$ to $|a\rangle$):

$$\begin{aligned}
W^{\mathrm{abs}} &= \frac{2\pi}{\hbar} \sum_n |\langle n|\, \mathscr{H}_2 + \mathscr{H}_3\, |i\rangle|^2 \cdot \delta(E_i - E_n) \\
&= \frac{4\pi^2 e^2}{m^2 c k V} \sum_n \left| \langle n|\, \mathrm{e}^{\mathrm{i}\mathbf{k}\mathbf{r}} \left[\boldsymbol{\varepsilon} \cdot \mathbf{p} + \mathrm{i}\hbar \mathbf{s} \cdot (\mathbf{k} \times \boldsymbol{\varepsilon}) \right] |a\rangle \right|^2 \cdot \delta(E_a + \hbar\omega - E_n) \\
&= \frac{4\pi^2 e^2}{m^2 c k V} \sum_n |\langle n|\, \boldsymbol{\varepsilon} \cdot \mathbf{O}(\mathbf{k})\, |a\rangle|^2 \cdot \delta(E_a + \hbar\omega - E_n).
\end{aligned} \tag{2.12}$$

Therefore, with the incident flux of photons $\Phi_0 = c/V$, we obtain

$$W^{\mathrm{abs}} = \frac{4\pi\Phi_0}{k} \operatorname{Im} w_{if}^{1+2}(\boldsymbol{\varepsilon} = \boldsymbol{\varepsilon}', \mathbf{k} = \mathbf{k}', \hbar\omega). \tag{2.13}$$

This is the well known **optical theorem** of scattering theory and represents an important link between RXD and *x-ray absorption fine structure* (XAFS) where it relates the imaginary part of the form factors with the linear absorption coefficient as we will see later.

In the following, we shall discuss the elastic scattering obtained by an atom. Before doing that, let us restrict the derivations on the special case of neglecting the scattering by spin. It will be sufficient for the applications in this work, since it aims for the characterization of structural modifications that are accompanied with atomic rearrangement. Magnetic scattering can usually be observed when the magnetic symmetry of the structure is lower than that of the charge and, hence, additional reflections occur. Otherwise, electric (charge) scattering dominates.

2.1.3. Scattering by an atom – form factors

To obtain the elastic charge scattering of an atom, we need to sum the scattering amplitudes in Eqs. (2.6,2.8,2.9) of all electrons. In the picture of electron density, we can instead perform a selected sum over all occupied initial states and unoccupied intermediate states $|a\rangle$ and $|n\rangle$, respectively. The resulting atomic scattering amplitude for charge scattering can be expressed as[1]

$$\begin{aligned} w^{1+2}_{\text{atomic}}(\boldsymbol{\varepsilon}, \boldsymbol{\varepsilon}', \mathbf{k}, \mathbf{k}', \hbar\omega) &= -\frac{e^2}{mc^2}\varepsilon'^{*}_{\alpha}\varepsilon_{\beta}\left(f_0\delta^{\alpha\beta} + f'^{\alpha\beta} + \mathrm{i}f''^{\alpha\beta}\right) \\ &=: -\frac{e^2}{mc^2}\varepsilon'^{*}_{\alpha}\varepsilon_{\beta}f^{\alpha\beta}(\mathbf{k}, \mathbf{k}', \hbar\omega) \end{aligned} \tag{2.14}$$

where we defined the conventional, nonresonant charge form factor (the Fourier transform of the whole electron density)

$$f_0 = \sum_a P_a \langle a| \mathrm{e}^{\mathrm{i}\mathbf{K}\mathbf{r}} |a\rangle , \tag{2.15}$$

and the "anomalous" dispersion correction

$$\begin{aligned} f'^{\alpha\beta} + \mathrm{i}f''^{\alpha\beta} = \frac{1}{m}\sum_{a,n} P_a(1-P_n)\Bigg(&\frac{\langle a| \mathrm{e}^{-\mathrm{i}\mathbf{k}'\mathbf{r}}\cdot p^{\alpha} |n\rangle \langle n| \mathrm{e}^{\mathrm{i}\mathbf{k}\mathbf{r}}\cdot p^{\beta} |a\rangle}{E_a - E_n + \hbar\omega - \mathrm{i}\Gamma/2} \\ &+ \frac{\langle a| \mathrm{e}^{\mathrm{i}\mathbf{k}\mathbf{r}}\cdot p^{\beta} |n\rangle \langle n| \mathrm{e}^{-\mathrm{i}\mathbf{k}'\mathbf{r}}\cdot p^{\alpha} |a\rangle}{E_a - E_n - \hbar\omega + \mathrm{i}\Gamma/2}\Bigg). \end{aligned} \tag{2.16}$$

The factors P_ξ denote the probability to find the state $|\xi\rangle$ occupied. The equations (2.15) and (2.16) are the central quantities to describe elastic x-ray scattering from charge. They describe the amplitude of x-rays scattered by an atom when neglecting scattering by spin and nuclei. The latter becomes significant if nuclear resonances are excited. Then, the nuclear scattering takes place on longer timescales and, therefore, can be observed after a certain time delay when the electronically scattered photons have passed. Eq. (2.16) takes account of resonant scattering. It carries the energy dependence and can be rewritten as an integral over energy when introducing the density of unoccupied electron states as before. The dependence on wavevector and polarization gives unique access to probe certain electronic transitions and perform orbital-sensitive measurements. Also it can contain a magnetic contribution even though we neglected the scattering by spins. This can be caused by a reduced symmetry in the electronic wave function due to the Zeeman effect or magnetic ordering. We will later (in Section 3.3.2) discuss the symmetry restrictions on the scattering amplitude as they play a central role when studying crystals.

The polarization and wavevector dependence of the form factors is usually only observed very close to the absorption edge – where the denominator in Eq. (2.16) is small. In many cases

[1] The Einstein notation is generally used in this thesis.

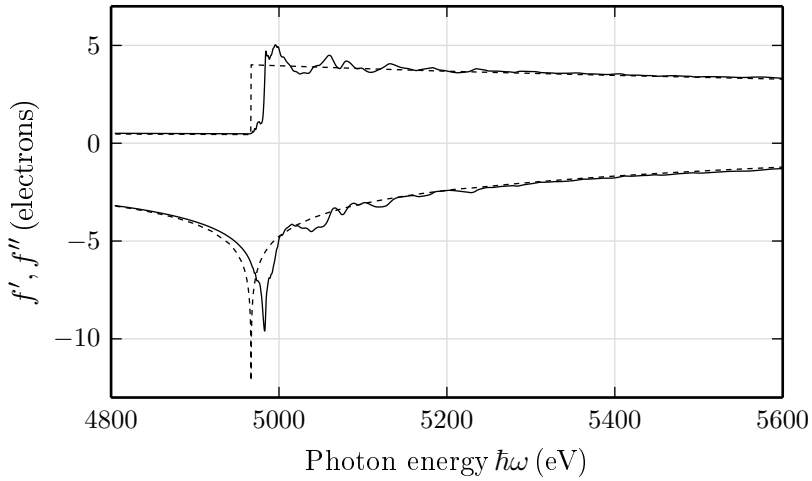

Fig. 2.3.: The real (negative curves) and imaginary (positive curves) parts of the dispersion corrections f', f'' of titanium without chemical environment (dashed lines) and in $SrTiO_3$ (solid lines) near the titanium K-edge. Pronounced fine structure oscillations can be seen in the latter case as well as an edge-shift which can be explained with a lower energy state of the 1s electrons when the titanium atom is in a chemical bond and has the corresponding formal valence state $4+$. The values for the smooth parts (dashed) have been taken from the Sasaki database [Sas89].

(e. g. in DAFS, XAFS) it is neglected and the form factors only carry an energy dependence and are expressed as scalars according to

$$f'^{\alpha\beta} + \mathrm{i}f''^{\alpha\beta} \xrightarrow{\text{off-edge}} \big(f'(E) + \mathrm{i}f''(E)\big) \cdot \delta^{\alpha\beta}. \tag{2.17}$$

This complex quantity typically includes a step-like increase in its imaginary part at each absorption edge, since the density of unoccupied states abruptly increases with energy and the imaginary part is linked with absorption according to the optical theorem (Eq. (2.13)). The real part, on the other hand, undergoes a gradual decrease before but an increase after the edge. This general progression is modulated with oscillations which are due to an inhomogeneous density of unoccupied states caused by the chemical environment of the considered atom. It is these oscillations which are referred to as *fine structure*.

Further simplifications are done when the energy is far from the edge based on the following reasons: *i*) the fine structure oscillations are only observed beyond the edge and they decay within a few 100 eV to a negligible magnitude (see Fig. 2.3), *ii*) the fine structure is different for each compound and its calculation is time consuming, rarely accurate and needs fitting of several unknown parameters. The most simple resonant correction is therefore obtained by neglecting the chemical environment of the resonant atom and to assume it to be isolated and in vacuum. Then, the unoccupied density of states is simply the continuum of vacuum states and is constant for energies above the absorption threshold. Hence, the correction terms f', f'' don't feature any fine structure and only the so-called "smooth" part can be observed. This can be easily calculated and is also deposited in databases for the majority of elements. Both

cases, including and neglecting chemical environment, are shown for the example of titanium in strontium titanate ($SrTiO_3$) in Fig. 2.3 near the K-edge.

2.1.4. Multipole expansion of the scattering amplitude

For the application of symmetry restrictions, it is very helpful to express all spatial dependencies of the atomic scattering amplitude as a tensor. In Eq. (2.16), a nonlinear dependence on the position vector $\mathbf{r}$ is obvious. A Taylor expansion of the exponential function is performed to obtain a sum of components linear to incremental powers of $\mathbf{r}$

$$\mathrm{e}^{\mathrm{i}\mathbf{kr}} \simeq 1 + \mathrm{i}\mathbf{kr} - \frac{1}{2}(\mathbf{kr})^2 \ldots, \tag{2.18}$$

referred to as dipole, quadrupole, octupole term etc. Additionally, the momentum vector of the electron can be replaced by its position vector with the help of the following commutator relation obtained from Schrödingers equation:

$$\frac{\mathrm{i}}{\hbar}\left[\mathscr{H}_0, \mathbf{r}\right] = \frac{1}{m}\mathbf{p}. \tag{2.19}$$

Functions that are linear to the n-th power of $\mathbf{r}$ can be written as a tensor of rank n. Through insertion into Eq. (2.16) we obtain the matrix elements

$$\langle n|\, \mathrm{e}^{\mathrm{i}\mathbf{kr}} p^\beta \,|a\rangle \simeq \frac{\mathrm{i}m}{\hbar}(E_n - E_a)\, \langle n|\, (1 + \mathrm{i}\mathbf{kr} - \frac{1}{2}(\mathbf{kr})^2 \ldots) r^\beta \,|a\rangle \tag{2.20}$$

and, thus, the tensor series expansion for the atomic scattering amplitude (omitting octupole terms)

$$\begin{aligned} w_{\mathrm{atomic}}^{1+2}(\boldsymbol{\varepsilon}, \boldsymbol{\varepsilon}', \mathbf{k}, \mathbf{k}', \hbar\omega) = \\ -\frac{e^2}{mc^2}\varepsilon_\alpha'^* \varepsilon_\beta \left(f_0 \delta^{\alpha\beta} + D^{\alpha\beta} + \mathrm{i}\left(k_\gamma I^{\alpha\beta\gamma} - k'_\gamma I^{*\beta\alpha\gamma} \right) + k_\gamma k'_\delta Q^{\alpha\beta\gamma\delta} + \ldots \right). \end{aligned} \tag{2.21}$$

Each tensor element in Eq. (2.21) represents certain excitation and relaxation processes ($D^{\alpha\beta}$ – dipole-dipole transitions, $Q^{\alpha\beta\gamma\delta}$ – quadrupole-quadrupole transitions and $I^{\alpha\beta\gamma}$ – dipole-quadrupole interference) and has a different rank. The big advantage of such decomposition is that each order of the transitions can be studied separately using the different behavior when applying symmetry operations: the components of a tensor of rank n undergo an n-times transformation during a change of basis. Later we will see that, in crystallography, it is possible to find reflections which are only containing contributions of one or few of these tensor components due to the space group symmetries.

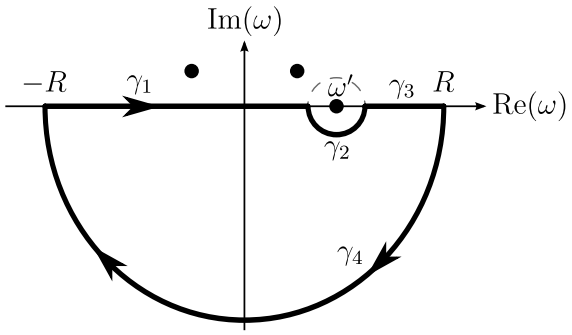

Fig. 2.4.: Path γ for integration in the complex plane which is used to apply Cauchy's integral theorem. The simple poles are indicated by black dots.

2.1.5. The Kramers-Kronig relations

We will now derive relations between real and imaginary part of the dispersion correction terms in Eq. (2.16). From the mathematical point of view, they are a superposition of complex functions of the kind

$$\eta^{\pm}(\hbar\omega) := \frac{1}{\pm(\hbar\omega - \mathrm{i}\Gamma/2) - \Delta E} \qquad \text{with} \qquad \Delta E = E_n - E_a. \tag{2.22}$$

One can directly verify that these functions fulfill the Cauchy-Riemann equations on the complete lower half of the complex plane of ω and, hence, are holomorphic there. They only contain simple poles at $\hbar\omega = \pm\Delta E + \mathrm{i}\Gamma/2$. This allows the application of Cauchy's integral formula,

$$\eta^{\pm}(\hbar\omega') = \frac{1}{2\pi\mathrm{i}} \oint_{\partial U} \frac{\eta^{\pm}(\hbar\omega)}{\omega - \omega'} \mathrm{d}\omega, \tag{2.23}$$

where U is any closed disc inside which $\eta^{\pm}$ is holomorphic (does not contain the pole) and $\omega' \in U$. This formula already gives a link between real and imaginary part of $\eta^{\pm}(\hbar\omega)$. However, we have no access to it since we can only perform measurements on the real axis of ω. The trick is to take the integral on a special contour including the real axis as it is sketched in Fig. 2.4. Inside the domain encompassed by this contour, the integrand in Eq. (2.23) is again holomorphic, since we excluded all poles. Therefore, we can make use of Cauchy's integral theorem, which states that in such domains, closed curve line integrals give zero and we obtain

$$\oint_{\gamma} \frac{\eta^{\pm}(\hbar\omega)}{\omega - \omega'} \mathrm{d}\omega = 0. \tag{2.24}$$

The integration contour γ can be decomposed into four characteristic parts: the mentioned parts along the real axis, both below (γ_1) and above (γ_3) the point of evaluation ω', a small semicircle (γ_2) around this point and a semicircle of radius R (γ_4) in the negative half of the complex plane. It is the straight sections of γ_1 and γ_3 which we can access experimentally. Furthermore, we extend the integration over the complete real axis ($R \to \infty$). Then, the integral over the large semicircle γ_4 can be found to be zero as well, since the integrand in

Eq. (2.24) decays with $|\omega|^{-2}$ while the contour length of γ_4 only increases with $|\omega|$. For the small circle, we can finally make use of Eq. (2.23). It tells us that the integral of the full circle (completed by a dashed grey semicircle in Fig. 2.4) would yield $2\pi\mathrm{i}\eta^{\pm}(\hbar\omega')$. This result does not change as the radius of the small circle is decreased allowing us to let it approach zero. In this case, the integrals along the real axis turn into the Cauchy principal value and the integral along the semicircle γ_2 will give half of that of the full circle:

$$\int_{\gamma_1}\frac{\eta^{\pm}(\hbar\omega)}{\omega-\omega'}\mathrm{d}\omega+\underbrace{\int_{\gamma_2}\frac{\eta^{\pm}(\hbar\omega)}{\omega-\omega'}\mathrm{d}\omega}_{\to\frac{1}{2}\cdot 2\pi\mathrm{i}\eta^{\pm}(\hbar\omega')}+\int_{\gamma_3}\frac{\eta^{\pm}(\hbar\omega)}{\omega-\omega'}\mathrm{d}\omega+\underbrace{\int_{\gamma_4}\frac{\eta^{\pm}(\hbar\omega)}{\omega-\omega'}\mathrm{d}\omega}_{\to 0}=0$$

$$\Rightarrow\mathcal{P}\int_{-\infty}^{\infty}\frac{\eta^{\pm}(\hbar\omega)}{\omega-\omega'}\mathrm{d}\omega=-\mathrm{i}\pi\eta^{\pm}(\hbar\omega').$$

The factor i results in a relation between real and imaginary part, which we need to identify:

$$\mathcal{P}\int_{-\infty}^{\infty}\frac{\mathrm{Re}\,\eta^{\pm}(\hbar\omega)+\mathrm{i}\,\mathrm{Im}\,\eta^{\pm}(\hbar\omega)}{\omega-\omega'}\mathrm{d}\omega=-\mathrm{i}\pi\left(\mathrm{Re}\,\eta^{\pm}(\hbar\omega')+\mathrm{i}\,\mathrm{Im}\,\eta^{\pm}(\hbar\omega')\right).$$

We obtain

$$\begin{aligned}\mathrm{Re}\,\eta^{\pm}(\hbar\omega')&=-\frac{1}{\pi}\mathcal{P}\int_{-\infty}^{\infty}\frac{\mathrm{Im}\,\eta^{\pm}(\hbar\omega)}{\omega-\omega'}\mathrm{d}\omega\\ \mathrm{Im}\,\eta^{\pm}(\hbar\omega')&=\frac{1}{\pi}\mathcal{P}\int_{-\infty}^{\infty}\frac{\mathrm{Re}\,\eta^{\pm}(\hbar\omega)}{\omega-\omega'}\mathrm{d}\omega.\end{aligned}\tag{2.25}$$

The negative energy region $\hbar\omega<0$ cannot be accessed experimentally but we can make use of symmetries in the calculation of the dispersion correction. On inversion $\hbar\omega\to-\hbar\omega$ the two additive terms in Eq. (2.16) exchange their denominator and, hence, the resonance behavior. The same can be achieved by doing a time reversal: $\boldsymbol{\varepsilon}'^{*}\leftrightarrow\boldsymbol{\varepsilon}$ and $\mathbf{k}'\leftrightarrow-\mathbf{k}$ (see also Eq. (2.8)+(2.9)). If we assume time reversal symmetry which corresponds to a neglect of magnetic contributions [Blu94], Eq. 2.16 can be rewritten as

$$f'^{\alpha\beta}+\mathrm{i}f''^{\alpha\beta}\overset{\text{non-mag.}}{=}\frac{1}{m}\sum_{a,n}P_a(1-P_n)\left\langle a\right|\mathrm{e}^{-\mathrm{i}\mathbf{k}'\mathbf{r}}\cdot p^{\alpha}\left|n\right\rangle\left\langle n\right|\mathrm{e}^{\mathrm{i}\mathbf{k}\mathbf{r}}\cdot p^{\beta}\left|a\right\rangle(\eta^{+}_{an}+\eta^{-}_{an}).\tag{2.26}$$

It can easily be verified that the function $\eta:=\eta^{+}+\eta^{-}$ is even in the real part and odd in the imaginary part. We can use that to obtain the integral of the negative half of frequencies in (2.25) by expanding the integrand with $\omega+\omega'$:

$$\mathrm{Re}\,\eta(\hbar\omega')=-\frac{1}{\pi}\mathcal{P}\int_{-\infty}^{\infty}\frac{\omega\,\mathrm{Im}\,\eta(\hbar\omega)}{\omega^2-\omega'^2}\mathrm{d}\omega-\frac{\omega'}{\pi}\mathcal{P}\int_{-\infty}^{\infty}\frac{\mathrm{Im}\,\eta(\hbar\omega)}{\omega^2-\omega'^2}\mathrm{d}\omega.$$

The second term gives zero since the imaginary part of η is odd as mentioned before. For the same reason, the first term can be reduced to twice the integral over the positive half and we get

$$\mathrm{Re}\,\eta(\hbar\omega')=-\frac{2}{\pi}\mathcal{P}\int_{0}^{\infty}\frac{\omega\,\mathrm{Im}\,\eta(\hbar\omega)}{\omega^2-\omega'^2}\mathrm{d}\omega.\tag{2.27}$$

The same reasoning for the second equation in (2.25) yields

$$\operatorname{Im}\eta(\hbar\omega') = \frac{2\omega'}{\pi}\mathcal{P}\int_0^\infty \frac{\operatorname{Re}\eta(\hbar\omega)}{\omega^2-\omega'^2}\mathrm{d}\omega. \tag{2.28}$$

Equations (2.27) and (2.28) are the well known **Kramers-Kronig** relations. They are valid for the dispersion correction $\Delta f := f' + \mathrm{i}f''$ if all coefficients in the sum of Eq. (2.26) are real. This is the case for example in forward scattering ($\mathbf{k} = \mathbf{k}'$) or in the dipole-dipole scattering approximation ($\mathrm{e}^{\mathrm{i}\mathbf{kr}} \approx 1$). The equations (2.25) are certainly valid in the more general case. An important fact for practice is the linearity of the integration. Therefore, the Kramers-Kronig (KK) relations commute with other operations such as convolution (broadening) with integrable functions and are valid also for superpositions of KK-consistent complex functions. This allows to overcome the problem of limited range of the measurement. If one has found a KK pair (real and imaginary part) which describes asymptotically the general progression of the resonant function outside the resonance region, this pair can be simply subtracted leaving some band-limited component allowing to perform the integral only within the "interesting" region. There are other ways to overcome the band limitation for experimental data, e. g., using the convolution theorem [Bru+02], decomposition of the spectrum into Laurent polynomials [Wat14] or into a Fourier series [Col77]. If certain points of the target spectrum (either real or imaginary part) are known, one can introduce these as "anchor" points into the *multiply subtractive Kramers-Kronig* (MSKK) algorithm [LSP03; PWB98]. The latter work describes a form of KK-relations which relates phase and intensity of the scattered wave.

2.1.6. Absorption of x-rays

Let us consider here the attenuation of the x-ray beam by matter. A photon can be absorbed by each atom on its path. Although it is difficult in practice to understand how large the photon amplitude is for each atom in the object, absorption can be described rather simply by statistical process considering a *homogeneous* beam of a large set of photons and a cross section much larger than the atoms. In this case, one just needs to sum up all atoms in the volume of the beam path weighted with their atomic absorption characteristics which have been obtained in Eq. (2.12). The attenuation of the beam is linked to the absorption coefficient μ via the Lambert–Beer law as

$$\mathrm{d}\Phi = -\Phi(z)\mu(z)\,\mathrm{d}z, \tag{2.29}$$

if the z coordinate describes the direction of propagation. From Eq. (2.12) we know, that the amount of absorbed photons per time in the illuminated volume $\mathrm{d}V = S\,\mathrm{d}z$ corresponds to

$$\sum_i n_i W_i^{\mathrm{abs}} = -\frac{\mathrm{d}\dot{N}}{\mathrm{d}V} = -\frac{\mathrm{d}\Phi}{\mathrm{d}z} = \Phi\mu,$$

where n_i is the number density of the atom i. With definition of the total scattering cross section σ_{int}, this can be written as

$$\mu(z) = \sum_i n_i(z)\sigma_{\text{int},i} = \sum_i \frac{n_i(z)W_i^{\text{abs}}}{\Phi(z)}. \tag{2.30}$$

However, not only the photoabsorption contributes to the integral scattering cross section – coherent, incoherent or Compton scattering and pair production losses to the beam intensity are not taken into account in W^{abs} [Car06]. Although photoabsorption is the dominant process in the x-ray regime, Compton scattering becomes more and more important at higher energies. To take account of the other processes attenuating the beam, the cross sections can be summed up:

$$\sigma_{\text{int},i}^{\text{tot}} = \sigma_{\text{int},i} + \sigma_{\text{int},i}^{\text{coh}} + \sigma_{\text{int},i}^{\text{compt}} + \sigma_{\text{int},i}^{\text{pair}} + \dots$$

Pair production is possible for photon energies larger than $\hbar\omega \geq 2mc^2 = 1022\,\text{keV}$ and was therefore not relevant for this work.

2.1.7. Scattering by many atoms – Born approximation

In this work scattering objects are treated within the independent atom model which means that their electron density can be described by a superposition of atomic (or ionic) electron densities

$$\rho^{\text{el}}(\mathbf{r}) = \sum_j (\rho_j^{\text{atom}} * \delta)(\mathbf{r}_j), \tag{2.31}$$

where $*$ denotes a convolution. Here, the anisotropy of the electron density with respect to polarization and wavevectors, which requires to take into account a reorientation of each atom in the sum, was neglected. Also we did not include resonant dispersion yet. To correct for this, it is possible to define an "effective" electron density having the same dependencies as the atomic scattering amplitude in (2.14). The electron density then represents the scattering potential for photons. Since the electromagnetic wave-equation is linear, using the Green's function method, one can describe the final state as a sum of initial state and the integral over all elementary scatterers (e. g. atoms) multiplied by the amplitude [Ric10]. The result is the Lippmann-Schwinger equation[2]

$$A'^{\alpha}(\mathbf{r}) = A^{\alpha}(\mathbf{r}) - \frac{e^2}{mc^2k^2}\int \mathrm{d}^3r' G^{\alpha\beta}(\mathbf{r},\mathbf{r}')\rho^{el}(\mathbf{r}')A'_{\beta}(\mathbf{r}')$$

which, according to Eq. (2.31) decomposes to the sum of integrals over all single atoms

$$A'^{\alpha}(\mathbf{r}) = A^{\alpha}(\mathbf{r}) - \frac{e^2}{mc^2k^2}\sum_j \int_{V_{\text{atom}}^j} \mathrm{d}^3r_j \rho_j^{\text{atom}}(\mathbf{r}_j)G^{\alpha\beta}(\mathbf{r},\mathbf{r}_j)A'_{\beta}(\mathbf{r}_j).$$

[2] Here, contravariant and covariant vectors have been introduced. This has no effect in cartesian coordinates but we will discuss it more thoroughly when introducing symmetry in crystallographic lattices in Ch. 2.2.4.

Here we use that we already know the response of an atom to the radiation (Eq. (2.14)). This is also where we reintroduce the anisotropy and resonance behavior. Using the definition of the scattering amplitude from an elementary scatterer at $\mathbf{r}'$

$$A'^{\alpha}(\mathbf{r}) = \delta^{\alpha\beta}A_\beta(\mathbf{r}) + \frac{e^2}{mc^2}f^{\alpha\beta}(\mathbf{k},\mathbf{k}',\hbar\omega)A'_\beta(\mathbf{r}')\cdot\frac{\mathrm{e}^{\mathrm{i}\mathbf{k}'(\mathbf{r}-\mathbf{r}')}}{|\mathbf{r}-\mathbf{r}'|}, \tag{2.32}$$

and assuming that the studied object is small with respect to the sample to detector distance ($|\mathbf{r}-\mathbf{r}'| \approx r$) we get

$$A'^{\alpha}(\mathbf{r}) = A^{\alpha}(\mathbf{r}) + \frac{e^2}{mc^2}\frac{\mathrm{e}^{\mathrm{i}kr}}{r}\sum_j f_j^{\alpha\beta}(\mathbf{k},\mathbf{k}',\hbar\omega)A'_\beta(\mathbf{r}_j)\mathrm{e}^{-\mathrm{i}\mathbf{k}'\mathbf{r}_j}. \tag{2.33}$$

One approach to solve this set of linear equations is by iteration [Blü12]: starting with insertion of the unperturbed field $\mathbf{A} = A_0\boldsymbol{\varepsilon}\,\mathrm{e}^{\mathrm{i}\mathbf{k}\mathbf{r}}$ for the field A' on the right hand side of the equation yields the first order approximation $\mathbf{A}^{(1)}$; subsequent insertion of the n-th order result yields $\mathbf{A}^{(n+1)}$. $\mathbf{A}^{(n)}$ is called the Born-expansion. Due to the rather weak interaction of x-rays and atoms, it is very common to abort the expansion after the first iteration, that is to say, to neglect multiple scattering events and, hence, to approximate

$$\mathbf{A}' \approx \mathbf{A}^{(1)}. \tag{2.34}$$

Eq. (2.34) is called the **Born approximation**. It also defines the *kinematical theory of diffraction* which is the norm in crystallography. The Born approximation is not valid only in rare cases like the diffraction from highly perfect crystals or stratified media. For these cases, special theories, like the *distorted wave Born approximation (DWBA)* or *dynamical theory of diffraction*, have been developed. The explicit form to calculate $\mathbf{A}^{(1)}$ then reduces to

$$A^{\alpha(1)}(\mathbf{r}) = A_0\Bigg(\varepsilon^{\alpha}\,\mathrm{e}^{\mathrm{i}\mathbf{k}\mathbf{r}} + \underbrace{\frac{e^2}{mc^2}\frac{\mathrm{e}^{\mathrm{i}kr}}{r}\sum_j f_j^{\alpha\beta}(\mathbf{k},\mathbf{k}',\hbar\omega)\varepsilon_\beta\mathrm{e}^{\mathrm{i}(\mathbf{k}-\mathbf{k}')\mathbf{r}_j}}_{=:A_{\mathrm{sc}}^{\alpha(1)}}\Bigg),$$

where A_0 denotes a scaling factor for the incoming radiation. The second term in the sum is the scattered wave we are interested in. Finally the amplitude ratio for scattered to incoming x-rays takes the form

$$\frac{A_{\mathrm{sc}}^{(1)}}{A_0} = \frac{\varepsilon'^{*}_{\alpha}\varepsilon'^{\alpha}A_{\mathrm{sc}}^{(1)}}{A_0} = \frac{\varepsilon'^{*}_{\alpha}A_{\mathrm{sc}}^{\alpha(1)}}{A_0} =: \frac{e^2}{mc^2}\frac{\mathrm{e}^{\mathrm{i}kr}}{r}\varepsilon'^{*}_{\alpha}\varepsilon_\beta F^{\alpha\beta}(\mathbf{k},\mathbf{k}',\hbar\omega) \tag{2.35}$$

where the F was defined as

$$F^{\alpha\beta}(\mathbf{k},\mathbf{k}',\hbar\omega) = \sum_j f_j^{\alpha\beta}(\mathbf{k},\mathbf{k}',\hbar\omega)\mathrm{e}^{\mathrm{i}\mathbf{K}\mathbf{r}_j}. \tag{2.36}$$

Since F describes the amplitude ratio which is caused by an arrangement of atoms, it is called the *structure amplitude*. Another common name is *structure factor* but the word amplitude points out more clearly that it carries a phase. It is the central quantity for the description

of scattering from extended objects within the Born approximation. Since it has the form of a Fourier series, the convolution theorem can often be applied when the studied object can be described by a convolution of particle distributions like, e. g., in case of crystals, as will be shown in the next section. On the other hand, the atomic composition of the studied object can be reconstructed with knowledge of the structure amplitude by means of inverse Fourier transform. However, in most cases, not the amplitude of the scattered radiation itself but only its intensity can be measured leading to the loss of phase information. This is also called the "phase problem" in x-ray diffraction. The measured beam intensity will then be proportional to the absolute square of the scattered amplitude and, therefore, also of the structure amplitude

$$\frac{I}{I_0} \propto \left| \frac{A_{\mathrm{sc}}^{(1)}}{A_0} \right|^2 \propto \left| \varepsilon_\alpha'^* \varepsilon_\beta F^{\alpha\beta} \right|^2 . \tag{2.37}$$

2.2. X-ray diffraction from crystals

Most inorganic solids are found in form of crystals which exhibit a high degree of spatial order. Except in the case of quasicrystals, this order means spatial periodicity of a certain set (unit cell, molecule) of atoms, usually in three dimensions. This set is called *basis* of a crystal. For each atom j of the basis, the positions of all associated atoms in an ideal 3D crystal are

$$\mathbf{r}_j^{(n_1,\ldots,n_D)} = x_j^i \mathbf{e}_i + n^i \mathbf{e}_i = \mathbf{r}_j + \mathbf{R}^{(n_1,\ldots,n_D)} \;\Big|\; 0 \le x_j^i < 1; n^i \in \mathbb{Z}; i = 1,\ldots,D \tag{2.38}$$

where $D = 3$ is the number of dimensions and $\mathbf{e}_i$ are the basis vectors defining the lattice. The first term corresponds to the position in the unit cell while the second term adds all positions equivalent due to spatial periodicity. The structure amplitude of such arrangement contains the sum over all these positions:

$$F^{\alpha\beta} = \sum_j \sum_{(n_1,n_2,n_3)\in\mathbb{Z}^3} f_j^{\alpha\beta} \mathrm{e}^{\mathrm{i}\mathbf{K}\mathbf{r}_j^{(n_1,n_2,n_3)}} = \underbrace{\sum_j f_j^{\alpha\beta} \mathrm{e}^{\mathrm{i}\mathbf{K}\mathbf{r}_j}}_{\text{basis}} \underbrace{\sum_{(n_1,n_2,n_3)\in\mathbb{Z}^3} \mathrm{e}^{\mathrm{i}\mathbf{K}\mathbf{R}^{(n_1,n_2,n_3)}}}_{\text{lattice}\to N_{\mathrm{uc}}} . \tag{2.39}$$

It can be seen that the structure amplitude can be separated in two parts – the first factor describes the contribution of the basis whereas the second factor is independent of the atomic composition of the crystal and is just a result of the crystal periodicity. Let us consider the more realistic case of a limited periodicity. The sum over all lattice points is then not taken over the whole integer numbers $\mathbb{Z}$ but on a certain rectangular box. Each summand is a complex number with absolute value of 1. Fig. 2.5 shows the $\mathbf{K}$-dependent diffraction intensity from a cubic lattice where $\mathbf{K} \parallel \mathbf{e}_3$ for a different number of lattice points in this dimension (n_3). It can be seen that lattice diffraction yields maxima when the projection of $\mathbf{K}$ on the basis vectors yields a multiple of 2π. The maximum intensity of the maxima is

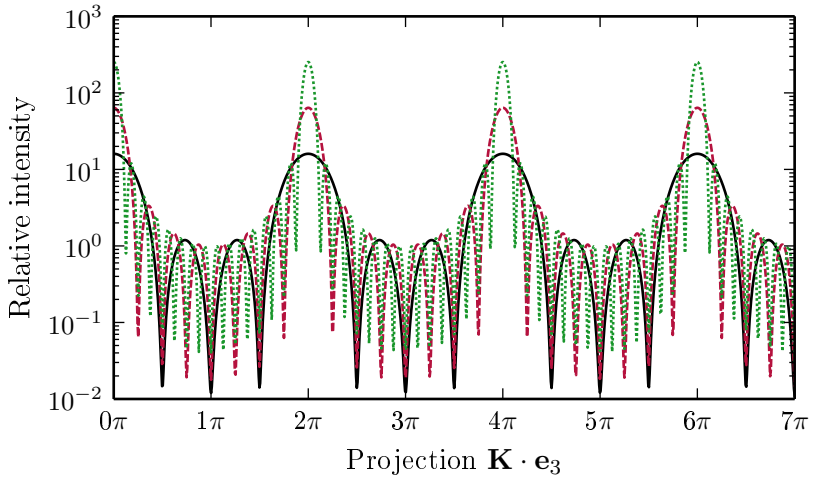

Fig. 2.5.: Calculated diffraction profiles of a monoatomic crystal slab with different number of layers for each line (black solid: 4, red dashed: 8, green dotted: 16). The scattering vector $\mathbf{K}$ is directed perpendicular to the surface.

proportional to the square of the number of lattice points. The general condition for these maxima to occur is

$$\mathrm{e}^{\mathrm{i}\mathbf{K}\mathbf{R}^{(n_1,n_2,n_3)}} = 1 \qquad \forall n_1, n_2, n_3. \tag{2.40}$$

It is equivalent to both Laue and Bragg condition. As the number of crystalline layers approaches infinity, the diffraction pattern takes the form of equidistant delta functions referred to as *Bragg reflections*. If the Laue condition Eq. (2.42) is fulfilled, the lattice part of the structure amplitude in Eq. (2.39) corresponds to the number of unit cells N_{uc} contained in the coherently illuminated sample volume. It is therefore often replaced with the crystallite volume.

2.2.1. Reciprocal lattice

The set of vectors $\mathbf{K}$ fulfilling the condition (2.42) is called the *reciprocal lattice*. It is spanned by discrete multiples of the basis vectors of the dual lattice $\mathbf{e}^i$ according to

$$\left\{ \mathbf{K} \middle| \, \mathbf{K} = 2\pi h_i \mathbf{e}^i; h_i \in \mathbb{Z} \right\}. \tag{2.41}$$

This is an alternative form of the Laue condition. To proof it, we make use of the definition of the dual vector space:

$$\mathrm{e}^{2\pi\mathrm{i}h_i n^j \mathbf{e}^i \mathbf{e}_j} \overset{\mathbf{e}^i\mathbf{e}_j=\delta^i_j}{=} \mathrm{e}^{2\pi\mathrm{i}h_i n^i} = 1. \tag{2.42}$$

The dual basis vectors can be obtained with help of the metric tensor g_{ij}

$$\mathbf{e}^i = g^{ij}\mathbf{e}_j \qquad \text{where} \qquad g_{ij} = \mathbf{e}_i\mathbf{e}_j \qquad \text{and} \qquad g_{ij}g^{jk} = \delta^k_i.$$

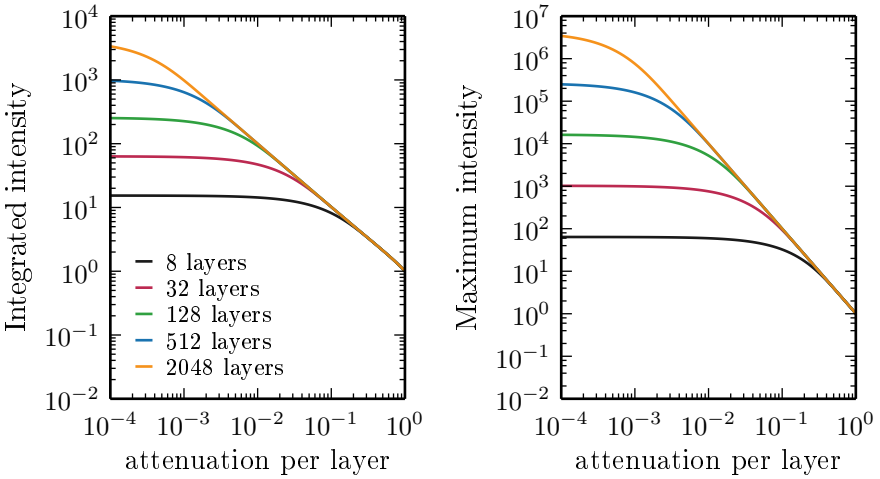

Fig. 2.6.: Influence of an beam attenuation per layer taken into account for calculation of the diffraction intensity for a system as in Fig. 2.5 and different numbers of diffracting layers. Left: integrated intensity. Right: maximum intensity of the first, symmetric Bragg reflection. For small absorption, the beam is simply attenuated according to the exponential decay in Lambert-Beer's law.

In other words, g^{ij} is the inverse of the metric tensor. The coefficients h_i define the Bragg reflection and are commonly named *Miller indices*: $h_i = (h, k, l)$.

2.2.2. Influence of absorption

We can see from Eq. (2.29), that the beam intensity is decreasing exponentially when passing through a homogeneous object. This is also true for crystals on typical absorption length scales ($\approx 1\,\mu\text{m}$). In reflection geometry for x-ray diffraction, this means that each diffracting layer contributes with a fixed fraction smaller than 1 with respect to the previous one. The effect on the diffraction peaks is easily calculated and illustrated in Fig. 2.6 as a function of attenuation per layer and for different numbers of layers. It can be seen that for crystal thicknesses much larger than the attenuation length the dependence of the diffracted intensity follows a power law with exponents 1 for the integrated intensity and 2 for the peak intensity. This is caused by a reduced amount of layers that contribute to diffraction and the resulting peak broadening. For low absorption the intensity loss can be simply explained by the exponential decay of the beam intensity passing through the crystal. We shall derive the equations that describe the effect of absorption on the diffracted intensity in the kinematical regime and for reflection geometry. To do so, let us consider the elementary scattered wave coming from a volume $\mathrm{d}V = \mathrm{d}x\,\mathrm{d}y\,\mathrm{d}z$ at a depth z below the crystal surface (see Fig. 2.7). The beam path of this partial scattered wave through the crystal is then $\Delta = z(\csc\alpha + \csc\beta)$, where α and β are incidence angle and exit angle, respectively. Therefore, its intensity is attenuated by a factor of $\exp(-\mu\Delta)$. Consequently, the x-ray amplitude is attenuated by the factor

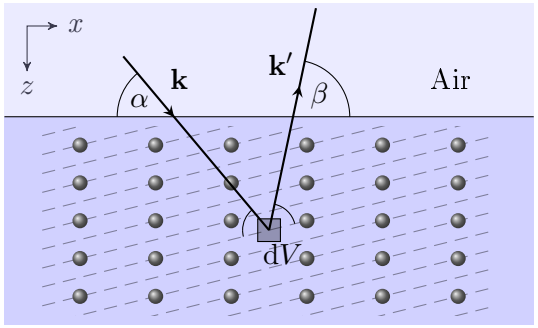

Fig. 2.7.: Drawing of the diffraction scheme in reflection ("Bragg") geometry. Elementary scattering in the volume $\mathrm{d}V$ is illustrated.

$\sqrt{\exp(-\mu\Delta)} = \exp(-\mu\Delta/2)$. Integration over the whole scattering volume gives the full attenuation of the peak amplitude of the Bragg reflection from a crystal slab of thickness d

$$\begin{aligned} A_{\mathrm{sc}}^{(1)}(\mu > 0) &= A_0 \varepsilon_\alpha'^{*} \varepsilon_\beta F^{\alpha\beta} \int_0^d \iint_S \mathrm{d}V \, \mathrm{e}^{-\mu\Delta/2} \\ &= A_0 \varepsilon_\alpha'^{*} \varepsilon_\beta F^{\alpha\beta} S \csc\alpha \int_0^d \mathrm{d}z \, \mathrm{e}^{-\mu z(\csc\alpha + \csc\beta)/2}. \end{aligned}$$

Here, S is the beam cross section and $\mathrm{d}z$ is chosen such that $\exp\{\mathrm{i}K_z \, \mathrm{d}z\} = 1$ to ensure that the structure factor is the same for each layer and can be moved outside the integral (otherwise, an extra phase factor would occur). This is valid since the wavelength of x-rays is by far smaller than the typical attenuation length and the exponential function would still be linear within $\mathrm{d}z$. One obtains the resulting absorption correction

$$A_{\mathrm{sc}}^{(1)}(\mu > 0) = A_0 \varepsilon_\alpha'^{*} \varepsilon_\beta F^{\alpha\beta} \frac{2S \csc\alpha}{\mu(\csc\alpha + \csc\beta)} \left(1 - \mathrm{e}^{-\mu d(\csc\alpha + \csc\beta)/2}\right).$$

Therefore, disregarding constant factors, the measured peak intensity will be modified due to absorption according to

$$\frac{I}{I_0} \propto \left|\frac{A_{\mathrm{sc}}^{(1)}}{A_0}\right|^2 \propto \left|\varepsilon_\alpha'^{*} \varepsilon_\beta F^{\alpha\beta}\right|^2 \left[\frac{1 - \exp(-\mu d(\csc\alpha + \csc\beta)/2)}{\mu(\csc\alpha + \csc\beta)}\right]^2. \tag{2.43}$$

This quadratic behavior can be seen in the right plot in Fig. 2.6. The result relies on a coherent sum of all waves scattered in the volume as well as on a nearly perfect crystal and high instrumental resolution. In practice, it is much more common to have a mosaic crystal which is composed out of many small single crystals that are slightly misaligned with respect to each other (*mosaic spread*). Furthermore, a certain beam divergence will lead to an averaging over many angles of incidence. As a result, there is no predictable phase relationship between the partial scattered waves and the calculation should be based on an incoherent superposition

of these. This is, in fact, what is most commonly observed. Therefore, the measured intensity including absorption will in this case be obtained via

$$\begin{aligned} I = \int \mathrm{d}I \propto \left|\varepsilon'^{*}_{\alpha}\varepsilon_{\beta}F^{\alpha\beta}\right|^2 \iint\limits_{0\,S}^{d} \mathrm{d}V\, \mathrm{e}^{-\mu\Delta} \\ \Rightarrow \frac{I}{I_0} \propto \left|\varepsilon'^{*}_{\alpha}\varepsilon_{\beta}F^{\alpha\beta}\right|^2 \int\limits_{0}^{d} \mathrm{d}z\, \mathrm{e}^{-\mu z(\csc\alpha+\csc\beta)} \\ = \left|\varepsilon'^{*}_{\alpha}\varepsilon_{\beta}F^{\alpha\beta}\right|^2 \underbrace{\left[\frac{1-\exp(-\mu d(\csc\alpha+\csc\beta))}{\mu(\csc\alpha+\csc\beta)}\right]}_{=:A}. \end{aligned} \tag{2.44}$$

In transmission (or "Laue") geometry, different results can be derived in a similar way, but in most cases within this work, Eq. (2.44) will be used to estimate or correct for the effects of absorption. In cases where no flat interface between crystal and environment is present, the attenuation of the beam can often only be approximated. Moreover, in the case of nearly perfect crystals, the interference of incident and scattered beam, which are comparable in intensity, can lead to standing x-ray waves in the crystal which stands in contrast to the exponential decay obtained before via the Lamber–Beer formula. In this case, the approximation of a homogeneous absorbing object fails to be applicable. Instead, it is crucial where the nodes of the standing wave field are. If they fall on the interatomic voids, for instance, an anomalous increase of transmission of x-ray through the crystal can be observed (called Borrmann-effect).

2.2.3. Influence of disorder

The picture of a strictly periodic (ordered) crystalline lattice is an approximation and never valid in reality. This is already due to the finite zero point energy in quantum mechanics: a particle is never at rest. When speaking of atomic positions in a crystal, one always refers to the average of those. Furthermore, real crystals contain defects where the regular arrangement of atoms is interrupted. These defects can be of various kind and dimensionality and can have a strong impact on the macroscopic properties of the crystal. In any case, the Eq. (2.37) still describes correctly the scattered intensity within the kinematical approximation. However, the decomposition into lattice and basis factors as in Eq. 2.39 is not correct anymore or rather needs to be modified. The effects of a random (Gaussian) displacement of atoms on the diffraction intensity are illustrated in Fig. 2.8. A decreased peak intensity can be observed which is stronger for higher reflection orders if the atoms are displaced from their ideal positions. On the other hand, an enhanced diffraction intensity can be observed between the peaks, often referred to as *thermal diffuse scattering*.

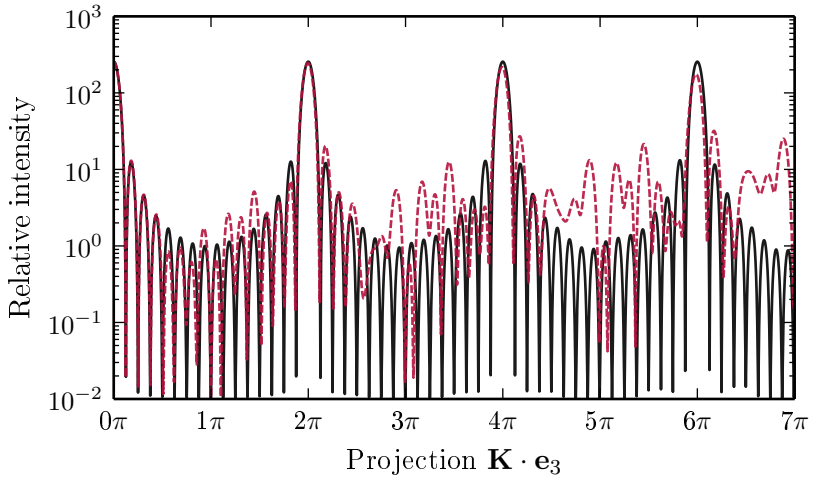

Fig. 2.8.: Influence of a mean square atomic displacement of all atoms for the monoatomic crystal slab of 16 layers. Shown is the resulting diffracted intensity in case of perfect order (black, solid line) in comparison to a case with normal random displacement with a mean square of $^1/_{30}$ of the lattice spacing (red, dashed line).

We will now aim to correct Eq. (2.39) so that it also describes the reflections from disordered crystals (but not the diffuse scattering). In order to do that, we assume that the crystal is large so that many lattice planes contribute to diffraction. This is true in most cases of x-ray crystallography. We can then view the crystal as a large set of unit cells which each have atoms at slightly different positions. The structure amplitude of the crystal basis is thus obtained by averaging over all of these unit cells:

$$F^{\alpha\beta} = \sum_j \langle f_j^{\alpha\beta}\, \mathrm{e}^{\mathrm{i}\mathbf{K}\mathbf{r}_j} \rangle \simeq \sum_j o_j f_j^{\alpha\beta}\, \langle \mathrm{e}^{\mathrm{i}\mathbf{K}\mathbf{r}_j} \rangle =: \sum_j o_j f_j^{\alpha\beta}\, T_j. \tag{2.45}$$

The averaging can, in most cases, be limited to the phase factor, since the environment of the atoms only slightly changes and therefore the atomic form factors remain almost unaffected. Then, the occupancy o_j describes the probability to find an atom occupying the site j of a unit cell. However, the changes in the form factors can be significant in certain cases of near-edge resonant diffraction when the reflection is suppressed or very weak for the ideal case.

Let $\mathbf{u}_j$ be the small displacement of a selected atom from its ideal position ($\mathbf{r}_j \to \mathbf{r}_j^0 + \mathbf{u}_j$). Assuming that the distribution of u_j in the crystal is Gaussian with mean zero, one can then parameterize the effect of averaging on the form factor as [AM11]

$$\langle \mathrm{e}^{\mathrm{i}\mathbf{K}\mathbf{r}_j} \rangle = \mathrm{e}^{\mathrm{i}\mathbf{K}\mathbf{r}_j^0}\, \langle \mathrm{e}^{\mathrm{i}\mathbf{K}\mathbf{u}_j} \rangle = \mathrm{e}^{\mathrm{i}\mathbf{K}\mathbf{r}_j^0}\, \mathrm{e}^{-\frac{1}{2}\langle (\mathbf{K}\mathbf{u}_j)^2 \rangle} = \mathrm{e}^{\mathrm{i}\mathbf{K}\mathbf{r}_j^0} \underbrace{\mathrm{e}^{-\frac{1}{2}K_l K_m \langle u_j^l u_j^m \rangle}}_{=T_j} \tag{2.46}$$

The real quantity T_j is the well known Debye-Waller factor. It reduces the scattering amplitude of the atom. The assumption of a Gaussian distribution is valid when the atomic

vibrations are harmonic. Then the oscillation energy of an atom j with eigenfrequency ω_j and mass m_j is

$$E_j^{\mathrm{ho}} = \frac{1}{2} m_j \omega_j^2 \langle u_j^2 \rangle$$

and the distribution of states in the canonical ensemble follows the Boltzmann distribution

$$P\left(E_j^{\mathrm{ho}}\right) \propto \mathrm{e}^{-\frac{E_j^{\mathrm{ho}}}{k_B T}} = \mathrm{e}^{-\frac{m_j \omega_j^2 \langle u_j^2 \rangle}{2 k_B T}}.$$

where T is the absolute temperature and k_B the Boltzmann constant. As shown in Eq. (2.46), the Debye-Waller factor can be calculated from the anisotropic mean square displacement which is commonly written as a tensor [Tru+96]

$$\langle u_j^l u_j^m \rangle =: U_j^{lm} \, |\mathbf{e}^l||\mathbf{e}^m| =: \beta_j^{lm}/2\pi^2 \tag{2.47}$$

and is a result of crystal structure determination. With Eq. (2.41) we get the alternative form

$$T_j = \mathrm{e}^{-h_l h_m \beta_j^{lm}}. \tag{2.48}$$

2.2.4. Symmetry in crystallography

We have introduced x-ray crystallography in a way that both the crystal and the diffraction is represented by a set of tensors. This is particularly beneficial, as we can calculate their behavior under change of basis. The description of crystals in terms of *direct* and *dual* space is very desirable, since the lattices are in general not cartesian. Crystals are usually classified according to symmetry operations under which they do not change [Won06; Aro+06]. These symmetries have to be valid also on a microscopic scale and are therefore imposed on the tensors described before. The crystal lattice is defined by the metric tensor g_{ij}. Crystallography describes which local symmetries are compatible with the translational symmetry of this lattice. They are tabulated in form of groups (*space groups*) for each crystal class in the International Tables for Crystallography [Hah06]. Each atom added to the unit cell of the lattice can reduce the symmetry resulting in another space group. The group elements are all (linear) symmetry operations found in the crystal. The *generators* are a subset, by combination of which all (other) members of the set can be produced. A subsequent application of these on the vector coordinates of an atom results in all other points of this site, thus "generating" the *crystallographic orbit*. To describe a crystal, only one specific atomic position per orbit is necessary (*asymmetric unit*) together with the set of generators and the metric g_{ij}. The amount of atoms per orbit is called *multiplicity*. Each generator can be represented by a matrix/vector pair $(\boldsymbol{W}, \mathbf{w})$ of rotation/translation part such that

$$\tilde{x}^i = W_j^i x^j + w^i, \tag{2.49}$$

where x^i and $\tilde{x}^i$ are the components of unit cell vectors of direct space before and after transformation, respectively. According to Eq. (2.38) $0 < x^i < 1$. Due to the crystal periodicity $0 < \tilde{x}^i < 1$ can be ensured (e. g. by $\tilde{x}^i \to \tilde{x}^i \bmod 1$). The translation part $\mathbf{w}$ changes only the position of the atoms whereas the rotation part $\boldsymbol{W}$ changes also their orientation. The latter also affects the tensors describing atomic properties like scattering or mean square displacement. Instead of transforming the tensor, the same can be achieved by **inversely** transforming their dual vectors. As an example, let us consider the case of polarization dependence of the scattering amplitude (see Eq. (2.14)) given in direct space (as contravariant vectors). Neglecting the wavevector dependence, we have after transformation

$$-\frac{mc^2}{e^2}\tilde{w}^{1+2}_{\text{atomic}} = \varepsilon'^{*\alpha}\varepsilon^{\beta}\tilde{f}_{\alpha\beta} = (W^{-1})^{\gamma}_{\alpha}\varepsilon'^{*\alpha}(W^{-1})^{\delta}_{\beta}\varepsilon^{\beta}f_{\gamma\delta}$$

Therefore, a symmetry operation as in Eq. (2.50) results in an inverse transformation of the covariant (dual) tensors on the new position according to

$$\tilde{f}_{\alpha\beta} = (W^{-1})^{\gamma}_{\alpha}(W^{-1})^{\delta}_{\beta}f_{\gamma\delta}.$$

Analogously the formula for the example of the twice contravariant tensor of thermal displacement β^{ij} is obtained. To understand how the components of a contravariant tensor will be transformed, let us consider a change of basis and the definition of the reciprocal lattice

$$\delta^j_i = \tilde{\mathbf{e}}_i\tilde{\mathbf{e}}^j \stackrel{!}{=} \mathbf{e}_i\mathbf{e}^j = \mathbf{e}_i(W^{-1})^i_k W^k_j\mathbf{e}^j. \tag{2.50}$$

It can be seen that the covariant components transform using the inverse transposed of the matrix representation:

$$\tilde{x}_i = (W^{-1})^k_i x_k.$$

Hence, following the same reasoning as before, we get for the components of the contravariant tensors the following transformation rule

$$\tilde{\beta}^{ij} = W^i_l W^j_m \beta^{lm}.$$

Although derived only for examples on tensors of rank 2, the transformation rules apply for all proper tensors with an arbitrary number of contravariant or covariant axes (as necessary for $I_{\alpha\beta\gamma}$ and $Q_{\alpha\beta\gamma\delta}$). To put the result in words: a new atom generated by $(\boldsymbol{W}, \mathbf{w})$ on position $\tilde{\mathbf{x}}$ will be described by different tensors $\tilde{\boldsymbol{f}}$ and $\tilde{\boldsymbol{\beta}}$ whose components are obtained as described. A more general introduction to the use of tensors in crystallography can be found in [Aut06].

2.3. Conclusion

It was seen in this chapter that atoms do not scatter isotropically. This can be due to anisotropic thermal motion and described by the Debye-Waller factor or due to anisotropy

in the local density of states which affects the scattering amplitude. In the former case, only anisotropy in the charge density is relevant. It can only be probed by comparing different Bragg reflections and is equal for all photon energies. In contrast, the anisotropy of the scattering amplitude depends on the density of unoccupied electronic states and is therefore strongly dependent on energy. It can typically only be observed for low energy excitations and therefore near an absorption edge. Moreover, in the decomposition of the scattering amplitude into a tensor series, each element (tensor rank) corresponds to a certain multipole transition. Each tensor component has a different influence on the polarization dependence which can be studied, for instance, by rotating the sample around the **K** vector or using polarizer or analyzer. For these reasons, the electron density can be studied not only spatially resolved but also as a function of energy and orbital specific by using resonant diffraction. These can be observed most clearly for reflections where the isotropic part of the structure amplitude $F_{\alpha\beta}$ is zero ("forbidden") due to the crystal symmetry which is why such reflections are also called *forbidden reflections*.

The approximation of isotropically scattering atoms, on the other hand, is acceptable when analyzing the fine structure oscillations of the extended part of the absorption edge and particularly useful when studying powder samples where it is impossible to disentangle the contributions from different crystallite orientations with respect to polarization or wavevector. This approximation is most common in the study of fine structure oscillations as in (extended) XAFS and DAFS. Their frequencies can be directly related to interatomic distances using the *extended XAFS* (EXAFS) equation [New14] (see Appx. A.1).

3. Methods

This chapter shall discuss the practical aspects of experiments which can be performed on the theoretical basis provided previously. It will be comprised of some very fundamental questions, such as how to obtain suitable x-ray radiation or how to acquire interpretable data. But they also include details on the data analysis which are specific for resonant diffraction experiments.

3.1. Generation of x-rays

Typical ways to produce x-ray radiation are either by the acceleration of charged particles or by their transition from an excited to a lower-energy state. In the most widely used sources based on vacuum tubes, both processes are contributing. An electron beam impinges on a metal target and the electrons are decelerated giving rise to the so-called *bremsstrahlung*. On the other hand, the electrons also can excite inner-shell electrons of the metal target. The subsequent relaxation of another electron into the core-hole is accompanied by the emission of x-ray photons with a characteristic wavelength. While the bremsstrahlung has a continuous spectrum, there exist only few of such characteristic emission lines for each atom. Except from a few "white-beam" experiments, it is favorable for the understanding of the observed phenomena to only use x-rays with a well defined wavelength. Therefore and since the intensity per energy interval of characteristic emission lines is about an order of magnitude stronger, bremsstrahlung of x-ray tubes is hardly used.

After their development in the late 19^{th} century, x-ray tubes were the only strong sources for laboratory experiments for more than 60 years. But this concept entailed a set of design based limitations and the x-ray yield for experiments could only be increased slowly with time. These limitations are comprised of:

- Undirected radiation of x-rays into the full solid angle allows only a small fraction of them to be used for measurements.

- Relying on characteristic emission lines, the wavelength of the x-rays cannot be scanned (it would result in very low intensities).

- The generation of x-ray via collisions of electrons on metal targets is not very efficient – most of the generators power is transformed into heat. This also represents the limitation for increasing the running performance. Despite cooling, the anode usually becomes too hot when operated beyond a few kW.

Using rotating anodes allows to distribute the heat load and therefore to increase the flux by roughly an order of magnitude. The latest development in this direction are liquid jet anodes, where the anode material is constantly cycled and refreshed, allowing an even higher operating power. However, some limitations still remain.

3.1.1. Synchrotron radiation sources

A completely different approach to the generation of x-rays is the deflection of highly relativistic charged particles using so-called *bending magnets*. It was first observed in a particle accelerator called *synchrotron* which is based on the synchronous increase of the deflecting magnetic field with the growing kinetic energy of the particle. While the radiation produced this way is therefore called *synchrotron radiation*, it is, especially nowadays, not only observed in synchrotrons.

Synchrotron radiation is not subject to the limitations listed above. Although the charged, relativistic particles also emit bremsstrahlung when being deflected by the magnetic field, the radiation is highly directed due to the time dilatation in special relativity. In the system moving with the particle, the spatial distribution of radiation corresponds to the one of an accelerated charged particle (Hertzian dipole) as it is known from classical electrodynamics [Jac99; Wil96]:

$$I(\Psi) = \frac{e^2}{16\pi^2\epsilon_0 m^2 c^3}\frac{1}{r^2}\,|\dot{p}|^2 \sin^2\Psi$$

where p is the momentum of the charged particle (e. g. electron) and Ψ is the angle between $\dot{p}$ and the direction of observation. The intensity distribution in the laboratory system is schematically shown in Fig. 3.1 in the form of isosurfaces for the relativistic ($\beta = 0.95$, $\gamma = E_{\mathrm{rel}}/mc^2 \approx 4.47$) and the non-relativistic ($\beta = 0.01$, $\gamma \approx 1.01$) case. One can see the deformation resulting from Lorentz transformation: the beam becomes directed into tangential direction. The momentum distribution undergoes a similar transformation, resulting in much higher values of photon wavevector (lower wavelength) in the direction of propagation of the charged particle. In modern synchrotron radiation sources, the value γ can be on the order of 10^4. The expansion of the photon momentum by the factor γ in direction of the particle propagation also leads to the typical small opening angle

$$\tan\theta_{\max} = \frac{1}{\gamma}$$

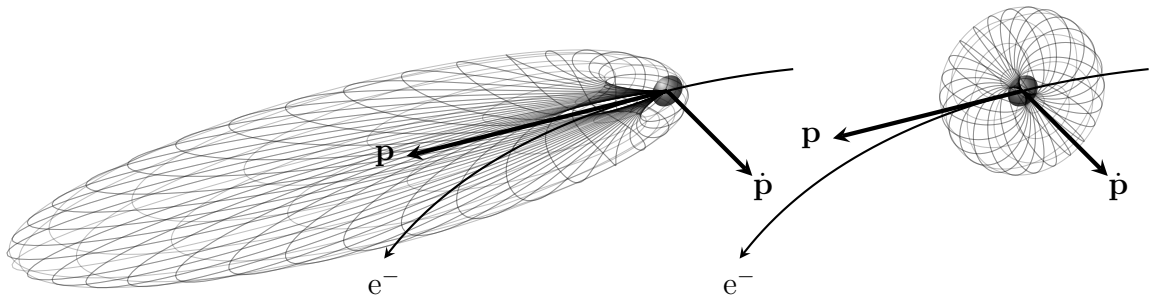

Fig. 3.1.: The spatial distribution of radiation intensity from a deflected charged particle traveling at relativistic speed ($\beta = v/c = 0.95$, left) and at non-relativistic speed ($\beta = 0.01$, right). The non-relativistic case shows the classical distribution of a Hertzian dipole. However, for the observer stationary in the laboratory system, the corresponding Lorentz transformation results in a deformation in the relativistic case.

of synchrotron radiation. The spectrum of such radiation is continuous and goes up to a critical energy of $\hbar\omega_c = 3\hbar c\gamma^3/2R$ [Sch49] beyond which it rapidly declines. Here, R is the local curvature radius of the deflection of the particles trajectory. Furthermore, the emitted radiation is highly polarized in the plane of the particle's orbit and pulsed, since the deflected charge is typically accumulated in short bunches.

Due to its advantageous properties, synchrotron radiation became a very popular tool in all branches of natural science. Therefore, particle accelerators have been developed and optimized to become dedicated sources. These are usually storage rings, where electrons or positrons are maintained at a fixed kinetic energy on an orbit with many deflection points where synchrotron radiation is produced. Such particle current can have a lifetime of several hours, depending on the vacuum conditions, resulting in a high radiation efficiency. To keep the current at a high level (resulting in a proportionally high radiation intensity) new particle bunches are regularly "injected".

3.1.2. Insertion devices

Although the radiation from bending magnets is already much more intense than that of x-ray tubes, there is in practice a rather sharp upper limit for the accessible flux since storage rings have a limited operation energy. This is defined by the radiation losses which are proportional to the fourth power of the particle energy [Wil96] and by the magnetic field which is needed to keep the particles on orbit. Furthermore, the bending magnet radiation is well collimated only in the direction of the magnetic field. In the other transverse direction, however, it is emitted as a fan and only a small part of this radiation can be used.

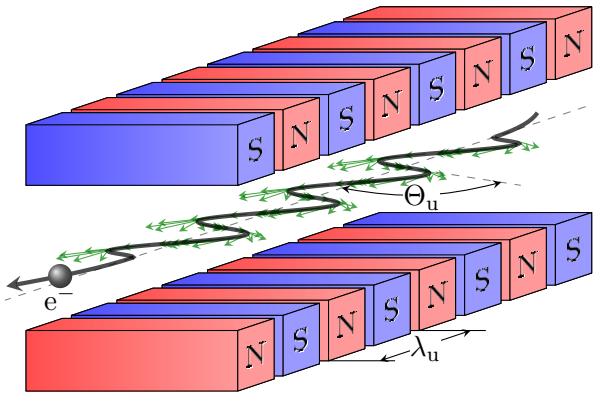

Fig. 3.2.: Schematic drawing of an undulator/wiggler – an alternating arrangement of permanent magnets in a straight section of the storage ring. Synchrotron radiation is produced where the electrons or protons are deflected corresponding of the positions of high field and largest displacement. The maximum angle under which radiation can be observed with respect to the optical axis is designated as Θ_u, the undulator period as λ_u.

A straightforward way to obtain a multiple of radiation flux is to stack several bending magnets, with alternating sign of the magnetic field, in a row (see Fig. 3.2). This way the total flux is enhanced proportional to the number of poles $2N_u$ where N_u is the number of magnetic periods which corresponds to an incoherent sum of the radiation produced at each pole. This is the concept of a *wiggler*. However, it may occur that the photons emitted at different positions interfere and therefore add up coherently. Under these circumstances, the device is rather referred to as an *undulators*. A well formulated, introductory derivation of the features of radiation from insertion devices can be found in the books [AM11; Wil96]. The key aspects shall be reflected briefly.

Undulators and wigglers can be described by three parameters: the number of periods N_u, the period length λ_u, and the undulator parameter K. The latter relates the maximum angle of the trajectory Θ_u (see Fig. 3.2) to the opening angle of the radiation cone in field direction (θ_{max}):

$$K = \frac{\Theta_u}{\theta_{max}} \approx \Theta_u \gamma.$$

Assuming a sinusoidal shape of the magnetic field with an amplitude B_0, one can derive

$$K = \frac{\lambda_u e B_0}{2\pi mc}.$$

The larger K, the less coherent is the superposition of the photons. Typically, one speaks of an undulator if $K \leq 1$.

The spectrum of an undulator is not continuous. In this case, the coherent interaction leads to a discontinuous spectrum of the radiation. The periodic emission of photons in each undulator period leads to the constructive interference of photons of a certain

energy (wavelength) and therefore a (fundamental) maximum in the spectrum. This wavelength can be calculated via the so-called *coherence condition*

$$\frac{hc}{\hbar\omega_1} := \lambda_1 := \frac{\lambda_\mathrm{u}}{2\gamma^2}\left(1 + \frac{K^2}{2} + \gamma^2\Theta_\mathrm{u}^2\right). \tag{3.1}$$

Even though the displacement of the electron due to the sinusoidal magnetic field is harmonic in the system moving with the particle, it is anharmonic in the laboratory-fixed system leading to the appearance of odd *higher harmonics* (maxima at multiples of the fundamental resonance energy, see Fig. 3.3). Furthermore, when observing the radiation off the optical axis, an additional phase-shifted component contributes to the apparent displacement hence allowing also the even harmonic. As can be seen in Eq. (3.1) and Fig. 3.3, the radiation emitted off-axis also exhibits asymmetric tails towards the lower energies in fundamental line as well as its harmonics which is due to relativistic Doppler effect. Usually, the energy of the fundamental line can be shifted by changing the distance of opposing poles ("undulator gap") resulting in a change of the magnetic field amplitude B_0.

The spectral and angular width of harmonics decreases with N_u. The interference effect on the undulator spectra grows with increased number of undulator periods. Moreover, the constructive interference is based on subsequent emission of radiation pulses at the points of maximum displacement in the trajectory of the charged particle (see Fig. 3.2). The length of the aggregated undulator pulse train is then proportional to the length of the undulator or the number of poles. Therefore, the spectral width of the pulse will be proportional to $1/N$ similar to the dependence on crystalline layers in x-ray diffraction. This way, one obtains for the n^th harmonic:

$$\frac{\Delta\hbar\omega}{\hbar\omega_n} \approx \frac{1}{nN_\mathrm{u}}.$$

From this result, the angular width can be approximated using the coherence condition Eq. (3.1) where the wavelength depends quadratically on the offset angle. This results in an angular width of

$$\Delta\Theta \approx \frac{1}{\gamma}\sqrt{\frac{1 + K^2/2}{nN_\mathrm{u}}},$$

which is independent of the azimuthal angle leading to similar beam sizes in horizontal and vertical direction.

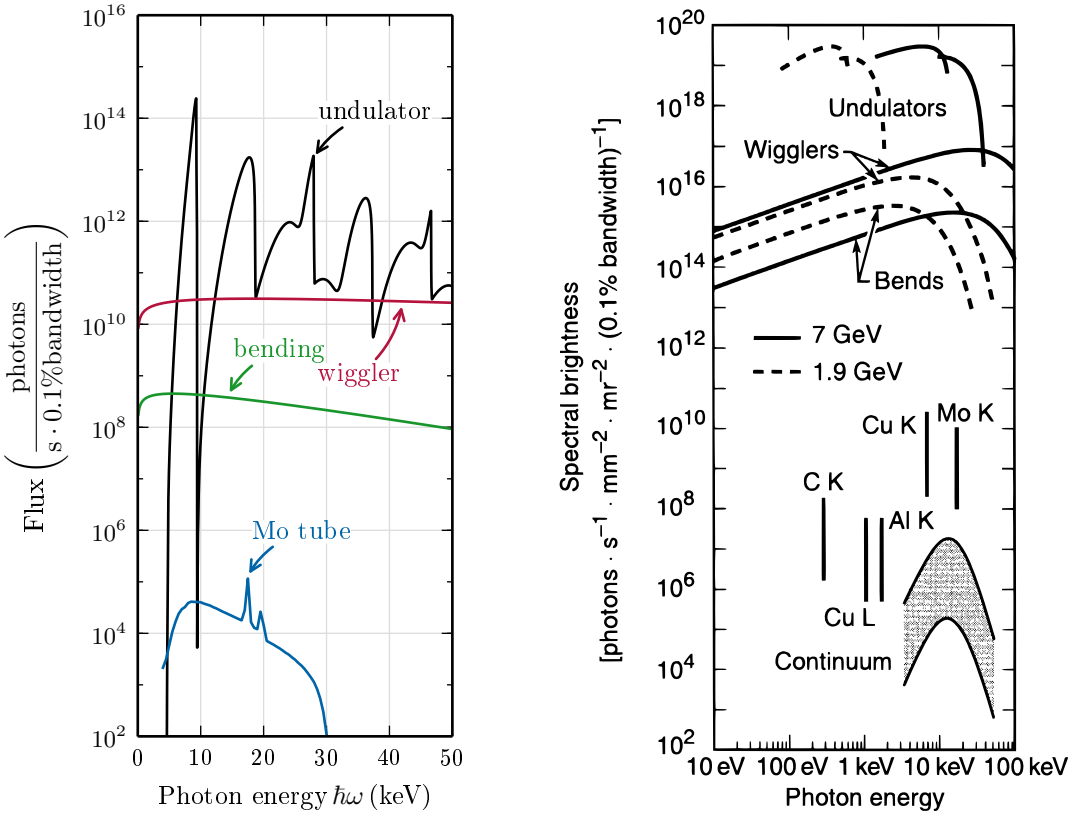

Fig. 3.3.: Left: typical spectra of the different x-ray sources calculated using the software package XOP [DS96]. The flux was calculated for a $1 \times 1\,\mathrm{mm}^2$ acceptance slit at $30\,\mathrm{m}$ distance. The spectrum for the tube is not drawn to scale and should be even a few orders of magnitude lower. Right: The range of what brightness can typically be achieved using the different sources for two different electron energies in the case of synchrotron radiation (taken from [Lin09]). The undulator gap is usually optimized to yield the maximum flux for each selected energy, resulting in a continuous spectrum on the right.

3.2. Measurement and data analysis

3.2.1. The resonant x-ray diffraction setup

An advantage of x-ray diffraction measurements is a high flexibility which is based on the rather easy generation of x-rays and their ability to penetrate through matter. This allows complex setups and sample environments also for laboratory sources. On the other hand, doing resonant x-ray experiments already requires the use of synchrotron sources to be able to tune the x-ray wavelength. The least requirements for resonant x-ray diffraction are therefore a tunable x-ray source, apparatus for beam shaping and a diffractometer which is used to mount the sample in arbitrary orientation and position as well as to detect the diffracted radiation. Fig. 3.4 shows a typical single-crystal x-ray diffraction endstation of a synchrotron with description of the different components:

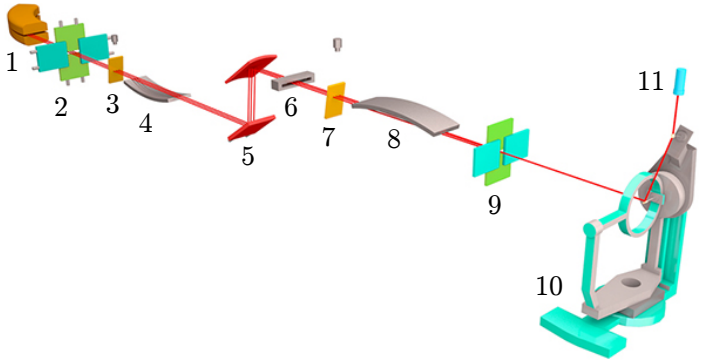

Fig. 3.4.: Drawing of a typical synchrotron setup for x-ray diffraction: (1) bending magnet or undulator source; (2+9) collimating slits; 3+7) beam position monitors; (4+8) focussing mirrors; (5) double crystal monochromator; (6) ionization chamber; (10) six circle diffractometer; (11) detector. Image taken from the webpage of the Kurchatov Synchrotron Radiation Source (KSRS) at http://www.kcsni.nrcki.ru/dyn_images/img12151.jpg .

The heart of such setup is the diffractometer (10) having at least four circles – one defining the scattering angle $2\theta_B$ within a fixed (usually vertical) scattering plane and three for the rotation of the sample (here around Eulerian angles). Some diffractometers have six circles also allowing the rotation of the scattering plane. Apart from that, diffractometers allow translation of the sample and often can accommodate heavy sample environments. Additional equipment frequently used in RXD is a polarization analyzer which is based on 90° diffraction by a crystal mounted before the detector such that the field component parallel to the scattered beam is suppressed (see Eq. (2.6)). A fluorescence detector is useful for online monitoring of the absorption in the sample.

The double crystal monochromator (5) is an essential device for RXD since it allows scanning of the photon energy. Two crystals are necessary to keep the position of the monochromatized beam fixed which also involves a translation of one of the crystals. Most commonly, silicon single crystals are used for monochromators due to their high quality, availability and also a negative thermal expansion at low temperatures. The latter is used under cryogenic conditions to avoid crystal lattice deformations due to a high radiation heat load. Different orientations of the single crystals are used (e. g. 111, 311, 511) to access different energy ranges and change the energy bandwidth. They can also help to avoid or shift "monochromator glitches" [BLW92] which are caused by an excitation of multiple reflections at the same time. These glitches occur at certain energies depending on which main reflection is used. Typical values for energy bandwidth are $\Delta E/E \approx 10^{-4}$ or lower for reflections of higher order than 111.

An important issue about monochromators is that the Bragg condition is always fulfilled for a set of discrete energies (wavelengths), called harmonics, which are related to the

fundamental wavelength λ_f via $\lambda_n = {}^{\lambda_f}/_n$. Harmonics distort the measured diffraction intensities since they are always part of the spectrum of the primary beam. In resonant diffraction, they cause a nearly constant offset which can be much larger than the interesting signal. One way to weaken harmonics is their higher sensitivity to a slight detuning of the two monochromator crystals. They can even be suppressed by the combining different monochromator crystals using the fact that the structure factor of certain subsets of the harmonics can be zero. However, the most common way to suppress the harmonics is the usage of mirrors.

(Focussing) mirrors (4,8): The most important purpose of mirrors is the suppression of higher harmonics. They only reflect for very small angles of incidence (total external reflection). Above a certain value α_c, the reflectivity of mirrors dramatically drops. As α_c decreases with higher photon energy, the higher harmonics are hardly reflected for targeted setting of the mirror [Lin09]. Furthermore, bending of the mirror allows focussing of the beam and, this way, increasing of the flux density.

Other equipment: A large set of further equipment is commonly used at a single crystal diffraction beamline. It is not intended to give a detailed list at this point but to mention some. Ionization chambers or other kinds of intensity monitors are used to characterize the beam intensity. Usually, much of the beam path is evacuated to keep air absorption as low as possible and to avoid diffuse scattering background. Beam attenuators are necessary to be able to control the intensity on the sample but also on the detector. Some scattering processes are many orders of magnitude weaker than others but usually the detectors can only process properly a few million photons per second. Typical attenuators are composed of a set of metallic foils of different thickness and can be inserted into the beam path on demand.

In a few cases, phase retarders can be used to change the polarization state of the incoming photons – either to rotate linear polarization or to produce circular polarization which allows to study chirality of the sample (e. g. natural chirality or magnetic moments). This is achieved through different responses of the different polarization states during transmission through a crystal under simultaneous excitation of a Bragg reflection.

Most of the experiments performed in this work relied on this kind of setup found at different synchrotron radiation sources.

3.2.2. The absorption correction

It was shown in Section 2.2.2 that the energy dependence of the diffraction intensity is affected by absorption which is pronounced and carries fine structure of the average sample. To allow an interpretation of the measured spectra, they usually need to be absorption-corrected based on the knowledge of the linear absorption coefficient μ (Section 2.1.6). To perform this correction, the absorption coefficient of the sample can be obtained in different ways:

Through measurement of fluorescence: A certain part of the absorption is due to photoexcitation which, again partially, results in emission of photons with characteristic (lower) energies. These energies are known for all elements and can be identified as well as isolated during the measurement. The advantage of using fluorescence is that it can be recorded in parallel to the measurement of RXD data and that it definitely corresponds to the same sample volume that is probed by diffraction which is especially important if the sample is inhomogeneous.

Considering a specific emission line at the photon energy E_f, the fluorescence intensity I_f from a sample of thickness d can be calculated for an angle of incidence α and an angle of observation β with respect to the sample surface via [BB05]

$$I_\mathrm{f}(E) \propto \frac{\mu_a(E)}{\zeta(E,E_\mathrm{f})}\left\{1-\mathrm{e}^{-\zeta(E,E_\mathrm{f})d}\right\} \qquad \text{where} \qquad \zeta(E,E_\mathrm{f}) = \frac{\mu(E)}{\sin\alpha}+\frac{\mu(E_\mathrm{f})}{\sin\beta}. \tag{3.2}$$

Here μ_a is the share of absorption that is due to a specific core excitation (edge) selected by the emission line ($\mu = \mu_a + \mu_\mathrm{nonresonant}$). In the so-called "thin sample limit" where d is small, such that

$$\zeta(E,E_\mathrm{f})d \ll 1,$$

the taylor expansion of the exponential function can be terminated after the second element ($\mathrm{e}^{-x} \approx 1-x$). Therefore, the fluorescence intensity is approximately proportional to the resonant part of absorption μ_a. Another favorable case where proportionality occurs is the "thick dilute limit". In this case, the term in braces in Eq. (3.2) equals to 1 and the amount of resonant atoms is small such that μ does not show any energy dependence while scanning the photon energy through the edge. Once μ_a is obtained it needs to be scaled and added on top of $\mu_\mathrm{nonresonant}$ in order to obtain absolute values for μ which can be done with help of the knowledge of the nonresonant progression of μ.

If the linearity of $I_\mathrm{f}(\mu_a)$ is not given, the measured fluorescence needs to be corrected for self-absorption. This means Eq. (3.2) has to be solved for μ. This is not possible analytically but, since $I_\mathrm{f}(\mu_a)$ is monotonous, there always exists a numerical solution.

Solving this equation for known parameters (thickness, angles, etc.) and a conversion to total absorption coefficient μ supported by table data for its smooth progression has been implemented in the software package "rexs" [Ric16b]. It further allows an optimization of parameters if they are not well known.

From transmission measurements: Eq. (2.29) shows that the absorption coefficient is readily obtained from measurements of the transmitted intensity I_t when the sample is homogeneous:

$$\frac{I_\mathrm{t}}{I_0} = \mathrm{e}^{-\mu d}.$$

In practice, the thickness or the primary beam intensity is often not known very well and a scaling as mentioned in the previous point can be necessary. The advantage of transmission is a more simple dependence of measured data on absorption coefficient but this measurement usually probes a different volume of the sample than the diffracted beam.

From other reflections: It may happen that the resonant atom does not contribute to the structure amplitude for certain reflections. In this case, μ can be obtained from the corresponding equation for absorption correction (e. g. Eq. (2.44)). For Bragg reflection from thick samples, another possibility is to divide the spectra of different reflections obtaining a quantity which is not affected by absorption. Remarkably, this quantity can then be analyzed in a similar manner as presented in Eq. (3.9) by measuring several reflections and solving a linear systems for the obtained phases.

In the case of powder diffraction, a homogeneous mix of the interesting powder with a reference can give another possibility for absorption corrections if the reference powder provides Bragg reflections in a similar angular range and does not contain any resonant atoms. However, the absorption measured using the reference does not contain the beam path through the crystallite of the interesting structure. Therefore, slightly different spectra are obtained and only a coarse correction is feasible as shown in Section 4.1.

3.3. Modeling and algorithms

It is important to discuss practical aspects of the theory provided in Section 2 and its implementation. The central quantity in this work are resonant parts of the atomic scattering amplitudes (or form factors) $f'^{\alpha\beta}$ and $f''^{\alpha\beta}$. Based on these, all kinds of elastic interaction of matter and x-rays (diffraction, refraction, reflectivity, etc.) can be calculated. As denoted by the indices α, β and as seen in Eq. (2.21), the scattering amplitudes have tensorial character

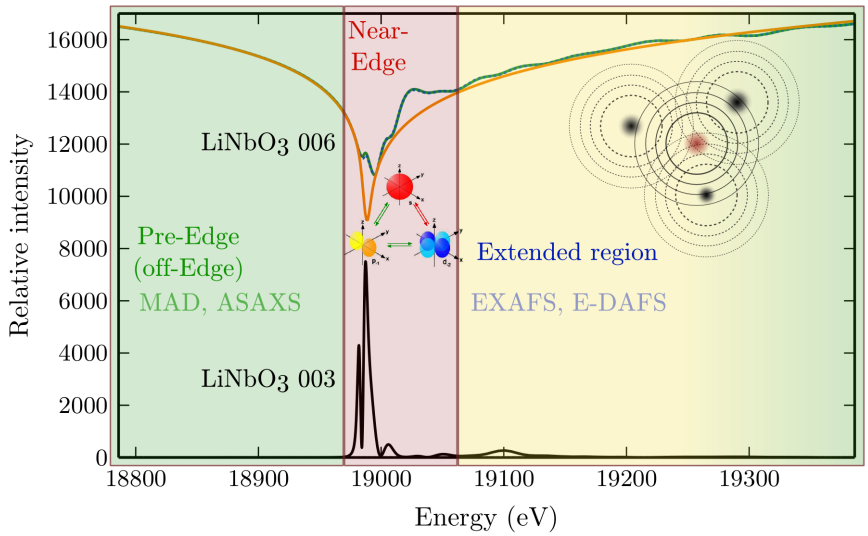

Fig. 3.5.: Illustration of the different regimes of RXD using the example of lithium niobate (LNO). Calculated resonant Bragg intensities are shown for two reflections of LNO, 003 and 006, near the niobium *K*-edge. The 003 (black line) reflection does only appear when taking into account polarization as well as wavevector dependence reflecting the anisotropic environment of the niobium atom. The anisotropy in only observed where polarization and wavevector dependence is strong which corresponds the near-edge region. The 006 reflection is shown for different stages of approximation. The orange line shows the smooth energy dependence that is a result of neglecting the chemical environment of the resonant atom (niobium). Taking into account the local structure, fine structure oscillations are observed (solid green curve). In the extended region, these can be explained by interference of spherical waves emitted in form of the excited photoelectron. Therefore, no anisotropy is observed in the extended region. This approximation is not valid in the near-edge region: taking into account wavevector and polarization dependence again leads to the blue dashed curve that essentially lies on top of the green curve shows a slight deviation at the edge. Remarkably, the scattering characteristics are already well described when neglecting the chemical environment, especially away from the edge. Therefore, the smooth variation is already basis for many resonant x-ray techniques as explained in the introduction in Section 1.1.

describing the dependencies on x-ray polarization and wavevectors. These dependencies are characterized by the density of unoccupied electron states at the absorbing atom. The density of states can be calculated *ab-initio* from atomic structure and based on a quantum mechanical solution of either Schrödinger or Dirac equation. There are, however, several stages of simplification of theoretical treatment in RXD which still allow its application and production of results. As before (Section 2.3), the level of theoretical treatment depends on the kind of measurement and also on the interesting energy region.

Figure 3.5 illustrates the different typical approximations for the example of lithium niobate $LiNbO_3$ and shows that, depending on the kind of experiment, they can yield sufficient agreement or not. In Equations (2.20,2.21) present an expansion which is treating the non-linear wavevector dependence by a series of increasing powers of (linear) tensors.

A very common approximation is the so-called dipole-dipole approximation where the taylor series is terminated after the first element ($e^{\mathbf{ikr}} \approx 1$) and therefore the wavevector dependence is neglected. This is usually a good approximation. However, in cases where diffraction up to second rank scattering tensors is forbidden by symmetry, the wavevector dependence can still lift the symmetry and cause a substantial intensity when the energy is very close to the absorption edge.

As soon as the reflections are allowed (strong) and the local symmetry around the absorbing atom is high, anisotropic scattering can be neglected completely. As a result, the scattering amplitudes can be described by scalar values and the indices (α, β) are dropped (see Eq. (2.17)). The fingerprint of the local atomic structure is then only seen in the energy (or wavelength) dependence of the scattering amplitude: starting shortly below the edge energy, oscillations appear and slowly decay within $\approx 1000\,\mathrm{eV}$ above the edge. These still carry information about the local density of unoccupied states. But from energies several $10\,\mathrm{eV}$ above the edge, the excited photoelectron carries sufficient energy to describe the observed fine structure oscillation in terms of photoelectron diffraction by the surrounding atoms as in EXAFS [RA00; AD75]. Moreover, a good modeling of the EXAFS oscillations can often be achieved by considering only single scattering events – especially at higher kinetic energies of the electron.

Last but not least, there are several fields of x-ray crystallography that solely exploit the change of scattering amplitude caused by the mere presence of an absorption edge without considering any fine structure [Hel00; HT81; Att90]. This usually does not consider the chemical environment but corresponds to the case of an isolated atom for which the scattering amplitudes are listed in tables [Cha95; Sas89; CHK97; HGD93] based on semi-empirical calculations [BC92; CL70]. Remarkably, this already is a good approximation in the x-ray regime – when their energy is below or far beyond ($> 500\,\mathrm{eV}$) the edge. A similar tabulation exists for the scattering vector ($\mathbf{K}$) dependence of the nonresonant scattering amplitude f_0 for common ions [Bro+06; SC98; MC01].

3.3.1. Calculation of scalar form factors and DAFS curves for the isolated atom

In this work, the different databases have been tested and mostly the Sasaki database ([Sas89]) was used since it has a good sampling in the near edge regions. Furthermore, a FORTRAN implementation of the Cromer-Liberman algorithm [CL70] has been used to calculate the scattering amplitudes of the isolated atoms for arbitrary energies (see [New98; Cro+98]). The software routine has been wrapped into python and is part of the software package “rexs”

written within this work [Ric16b]. It also contains routines for interpolation of the different tabulated data of dispersion correction as well as the nonresonant term f_0.

3.3.2. Bound atoms and fine structure

When a good knowledge of the scattering characteristics of a resonant atom is required, the fine structure needs to be considered as soon as the photon energy is close or larger than the resonance. This depends on the local arrangement of atoms around the absorber and can therefore not be obtained from databases. The following section will discuss theoretical and empirical ways to derive the fine-structure of dispersion which either allows a modeling of the measured diffraction spectra or can be interpreted in the course of (virtual) photoelectron diffraction.

Phenomenological and numerical (ab-initio) calculation of form factor tensors

In the recent years, there was a strong progress in the development of software to calculate the fine structure from "first principles". This is based on given atomic coordinates either inside a cluster around the absorbing atom or on a periodic lattice. It often includes the computation of local density of electronic states (LDOS) for the given structure solving non-relativistic (Schrödinger) or relativistic (Dirac) quantum mechanical wave equations (full potential). This is then followed by the evaluation of matrix elements for the excitation of core electrons according to Fermi's golden rule and Eq. (2.4) [Jol01; BJ09]. Other approaches are the calculation of electron scattering amplitudes based on muffin-tin approximation which involves a spherical averaging of the potential [Reh+10; BDN03]. The latter results in a loss of sensitivity to polarization or wavevector and is mostly used for the description of the extended energy region (EXAFS, $> 30\,\mathrm{eV}$ above the edge). However, these approximate calculations are much faster than full potential calculations.

Another kind of calculations that can be helpful is of phenomenological character meaning that they do not envision a quantitative modeling of absorption or diffraction spectra. Instead, scattering characteristics are discussed as a function of (unknown) tensor components of the atomic scattering amplitude. This course of action is still informative and important since it allows to estimate the occurence and strength of certain contributions. A symmetry analysis can be done and access to different scattering processes can be pointed out which allows the design of strategies for experiments. For instance, space group symmetry will allow certain reflections to occur only under consideration of wavevector dependence. These reflections can

contain contributions due to point defects depending on the symmetry with respect to time inversion. In Section 4.3.2 an example is presented.

In order to perform such phenomenological characterization of the diffraction process, the scattering amplitude is developed into a series of cartesian tensors as shown in Eq. (2.21). Each of the tensors exhibits symmetries that are either intrinsic (inherent in the scattering process and not depending on the crystal structure) or defined by the local symmetry of the Wyckoff site that is occupied by the resonant atom. The former can be due to approximations (e. g. neglect of magnetic scattering) but are also due to a redundancy in the description via cartesian tensors. Another possible and equivalent description uses spherical coordinates (tensors) which have less components and therefore provide an irreducible presentation [Pao14; Lov+05; Mat12]. It has the appeal that it allows a direct relation of each term with certain multipoles of charge or magnetic moment [DJN05]. In this work, the phenomenological approach is limited to charge scattering up to linear wavevector contribution (quadrupolar order) and only cartesian tensors have been used. Therefore, the following symmetries should be mentioned (see Eq. (2.21)):

- $D^{\alpha\beta} = D^{\beta\alpha}$ if magnetic scattering is neglected

- $I^{\alpha\beta\gamma} = I^{\alpha\gamma\beta}$ due to a commutativity in the perturbation operator (see e. g. [Blu94; Kok+10]) and Section 2.1.4

Apart from that, $D^{\alpha\beta}$ and $I^{\alpha\beta\gamma}$ are real in case that magnetic scattering can be neglected. Consequently, the dipole-quadrupole interference term in Eq. (2.21) adds a purely imaginary component to the scattering amplitude. Within this work, a software package has been developed [Ric16a] which is capable of phenomenological symmetry analysis by means of symbolic calculations based on *sympy* [Joy+12]: all atomic attributes such as tensor components can be left unknown and are described by specific symbols carrying information about the properties of the physical quantity (e. g. real, complex, positive,...). The following steps describe the typical workflow/features of the software:

- definition of the structure: **space** group, **asymmetric unit**, **lattice parameters**

- assigning tensor properties for each atom and applying inherent symmetries from above in cartesian space

- invoking the space group **generators** for several purposes:

  - application on each atomic position of the asymmetric unit to fill the unit cell with the orbit (all equivalent atoms, see Section 2.2.4)

  - transformation of tensors (represented in direct crystal lattice basis) describing atomic properties using the rotation part of the generator only

  - determination of tensor symmetry: this is done by collecting a set of equations when generated positions occur several times

- calculation of the structure amplitude tensor

- transformation of the structure amplitude into the cartesian laboratory system (following [KPE91; KP92])

- contraction of the tensors for certain Bragg reflections and polarization channels

- substitution of symbols with values taken from databases or from numerical simulations done with other codes (e. g. FDMNES [Jol01; Jol03])

To give an impression of the practical usage of the software, Fig. A.1 in Appx. A shows a piece of Python script that goes through the steps of a similar workflow for the specific example of a gallium nitride (GaN) crystal. Obtaining the actual expressions of structure amplitudes for scattering by simple algebraic formulae allows a deeper understanding of the different contributions for a specific structure. There are several other functions implemented for practical calculation of RXD that are not listed here in detail. Among them are: importing fine structure data from XAFS measurements, calculating powder diffraction patterns, Renninger scans, absorption, etc.

Extraction from absorption measurements – application of Kramers-Kronig relations

Diffraction (DAFS) and absorption (XAFS) carry the same information about the fine structure in cases where only one unique kind of resonant atoms exists in the structure, i. e. where all resonant atoms have the same chemical environment. Still, the energy dependence of diffraction carries more information about the crystal structure (see e. g. Section 4.2.2) and an interpretation is facilitated by proper modeling based on a known fine structure. That is why the imaginary part of the fine structure f'' is often extracted from absorption measurements through the optical theorem (see Eq. (2.13)). As described in Section 2.1.5, the real part f' is not independent from the imaginary part and can be calculated based on the

knowledge of the latter using the Kramers-Kronig relations Eq. (2.27). In that section, it was already mentioned that the KK transform entails certain practical problems like the integration over the complete energy axis and the calculation of the Cauchy principal value. Possible solutions have also been discussed. The procedure, that has been used in this work, will be explained more detailed in the following.

The x-ray regime offers the unique advantage that the asymptotic behavior of the scattering amplitude is known when moving the photon energy away from resonances: it corresponds to the case of an isolated atom (neglecting chemical environment). Since the KK relations are linear integrals, any KK pair (real and imaginary part) can be added or subtracted on the corresponding side of the Eqs. (2.27,2.28) without affecting their validity. Therefore, the scattering amplitude or form factors are typically decomposed into the known, "smooth" part f_s of the isolated atom and the complex fine structure part $\tilde{\chi}$ that depends on the local structure

$$f'(E) + \mathrm{i}f''(E) =: f'_\mathrm{s}(E) + \mathrm{i}f''_\mathrm{s}(E) + \tilde{\chi}(E). \tag{3.3}$$

This way, the fine structure function $\tilde{\chi}(E) = \chi'(E) + \mathrm{i}\chi''(E)$, $(E = \hbar\omega)$ is **band-limited**, only non-zero near the absorption edge and takes account of the chemical environment. It can interpreted in terms of spherical wave photoelectron diffraction from the surrounding structure in the extended region beyond the edge (see Appx. A.1).

Having a band-limited kernel (fine structure function) allows to compute convolution according to Eqs. (2.27,2.28). The problem of calculating the Cauchy principal value was overcome by using a regular grid of energies in which the integration is performed. In cases where the measurement was not performed on a regular grid, the data needs to be rebinned or interpolated. By an absorption measurement, the imaginary part of the fine structure function is then sampled for the energies

$$E_i = E_0 + i \cdot \Delta E, \quad i = 0, \ldots, N. \tag{3.4}$$

To avoid divergence of the integrand in Eq. (2.27), the energy of evaluation E' (or frequency ω') must not coincide with one of the given regular grid. Therefore, a shifted regular grid with the same stepping ΔE was chosen for the evaluation energies:

$$E'_i = E_0 + i \cdot \Delta E - \Delta E/2, \quad i = 0, \ldots, N+1. \tag{3.5}$$

This way, a symmetric sampling of the pole is realized which is crucial for the correct output. Then, the integration can be performed numerically using, e. g., the trapezoidal rule. It works well if the spectra are sampled with a fine stepping. The result can be improved easily, by using another commensurate regular grid. For instance, taking an m-fold finer energy stepping ΔE as illustrated in Fig. 3.6 will lead to a multiple of the number of points $(N{+}1 \to m(N{-}1){+}2)$ for the evaluation of the integral. Subsequently, the result can be interpolated again to obtain

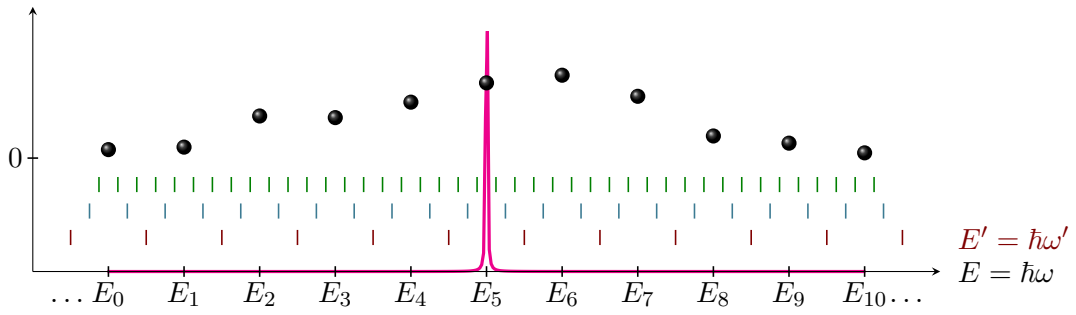

Fig. 3.6.: Illustration of convenient regular grids (colored ticks) for evaluation of the integrand in KK relations Eq. (2.27) providing a symmetric sampling of the pole (shown for $E = E_5$) for integration. The sampling rate can be arbitrarily increased. Black dots show exemplary measured data points for instance of χ_i'' measured for energies E_i.

the values on the original grid E_i. This way of KK transform has been implemented in this work [Ric16b] with the additional opportunity to define known anchor points of the target spectrum. However, it turned out that this option can result in strong overshoot oscillations and was not used in most of the cases.

The method of iterative Kramers Kronig transform

In the previous part, the extraction of the fine structure function based on absorption measurements was described. This, however, is not possible when there is more than one unique resonant atom in the sample, since absorption averages over all atoms of the same chemical species. In this case, DAFS can be used to isolate the fine structure of all resonant atoms. In DAFS, the measured signal is not the average of all resonant atoms but corresponds to the modulus of a weighted sum of their scattering amplitudes. The weighting can be varied by choice of different reflection according to the structure factor. It will be described here, how to obtain the fine structure function of the atoms from DAFS measurements.

It was mentioned before that the atomic scattering amplitudes can be decomposed into a sum of a smooth, known part and the fine structure. The same thing certainly applies for the structure amplitude F, as it is a weighted sum of scattering amplitudes (see Eq. (2.45)):

$$F = F_\mathrm{s} + \Delta F. \tag{3.6}$$

This situation is sketched in Fig. 3.7. While F_s is known, ΔF undergoes the characteristic fine structure oscillations. The measured intensity corresponds to the distance from the complex origin and therefore describes a circle in the complex plane when the phase is unknown.

To retrieve the phase and ΔF, an iterative algorithm has been developed and presented in literature [Pro+99; Pic+93]: while per each point of energy only one value is measured, there

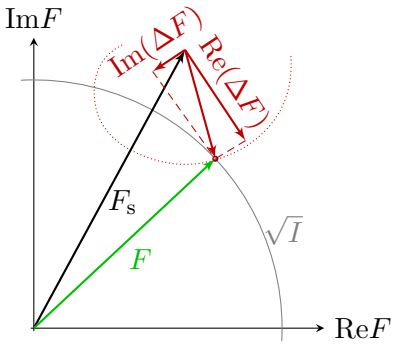

Fig. 3.7.: The resonant structure amplitude drawn in the complex plane illustrating the decomposition into a smooth, known part (F_s, black) and a fine structure part (ΔF, red) which add up to F. A schematic fine structure oscillation in ΔF is sketched with the dotted line. The measurement yields the modulus of the total structure factor $|F| \propto \sqrt{I}$.

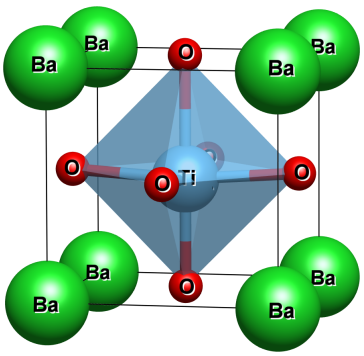

Fig. 3.8.: Projection of the unit cell of ferroelectric barium titanate onto the a-c plane. The non-centrosymmetric structure with was used as a model to test the different methods for phase retrieval.

are two unknowns which are the real and imaginary part of ΔF. However, we learned that both parts are not independent. Real and imaginary part for each atom are linked by KK relations, but if several atoms are resonant, the sum of fine structure functions ΔF does only fulfill the KK relations if imaginary and real parts are not mixed. This is the case when the phase factors (see calculation of the structure amplitude in Eq. (2.45)) are real for a certain reflection which is generally true for centrosymmetric crystal structures. Then, the fine structure of ΔF can be obtained by

(a) solution of $\mathrm{Re}(\Delta F)$ for each energy to meet the measured intensity ($\sqrt{I} = |F|$),

(b) KK transform of the real part $\mathrm{Re}(\Delta F)$ to obtain the imaginary part,

(c) re-iteration of (a) and (b) until convergence.

It should be noted that step (a) can have 0, 1 or 2 solutions which can potentially cause problems in the algorithm (see Fig. 3.7). Therefore, two slightly different approaches have been tested for step (a) in this work which were

(a') scaling ΔF in radial direction to meet $\sqrt{I}$: $\Delta F = \left(\sqrt{I/I_\mathrm{s}} - 1\right) \cdot F_\mathrm{s}$, where $I_\mathrm{s} = |F_\mathrm{s}|^2$

(a") randomized variation of ΔF proportional to the square root of local discrepancy between measured and calculated intensity.

The latter variant (a") converges very slowly and requires a large amount of iterations. But

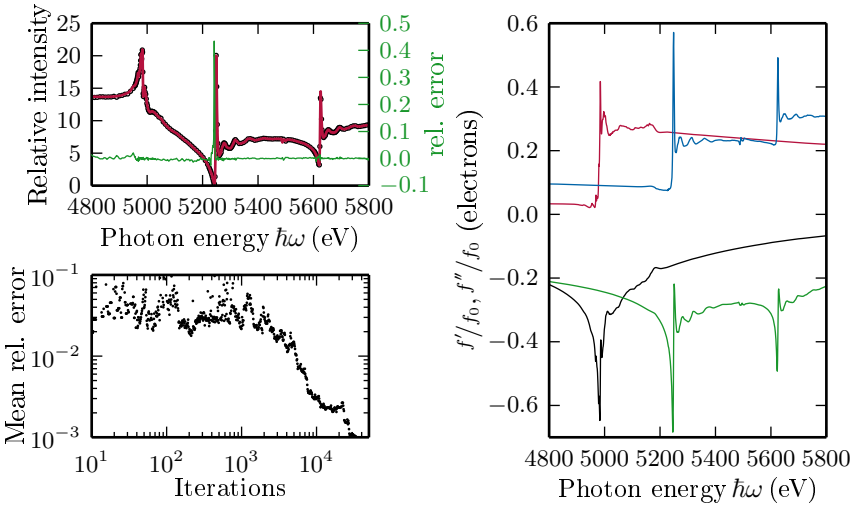

Fig. 3.9.: Results of the retrieval of fine structure via randomized variation of the initial guess (zeros) of the imaginary part of the fine structure function $\chi''(E)$ and subsequent KK-transform to obtain the real part $\chi'(E)$. The energy range was split into two parts where fine structure was ascribed to either titanium or barium (at $\approx 5190\,\mathrm{eV}$). Top left: comparison of measurement and iterative fit. A high relative deviation at the minimum is visible. Bottom left: the development of the mean relative deviation with number of iterations. Right: the resulting resonant scattering amplitudes f', f'' normalized to the nonresonant (Thomson scattering).

since the typical computation time per RXD curves are rather short, this poses only a small problem. Fig. 3.9 shows an application of this procedure on the RXD spectra of the 001 reflection of ferroelectric barium titanate $BaTiO_3$ (BTO) layers. Only one atom has been assumed to show a fine structure for a certain energy circumventing the problem of a non-centrosymmetric structure, although the edges of titanium and barium are close to each other. In particular, the energy region was split at $\approx 5190\,\mathrm{eV}$ and each part ascribed to the corresponding atoms. An accidental destructive interference is observed in the barium L_3-preedge: scattering amplitudes from different kinds of atoms cancel each other out causing a pronounced minimum. This is a case where step (a) is very likely to fail. In contrast, following (a') and (a"), a certainly more robust algorithm is obtained. Nevertheless, the correct description of the minimum also fails in these cases (see also Fig. 3.10) due to high sensitivity to small absolute deviations. If there is only one absorbing atom defined, as in the present case, ΔF can be directly converted into the atomic fine structure function $\tilde{\chi}$ by dividing by the corresponding crystallographic weight (the phase factor).

New approaches – the logarithmic dispersion relations

Another, only recently presented, approach to solve the phase problem in DAFS and, this way, to extract the fine structure of atoms is by the use of *logarithmic dispersion relations*

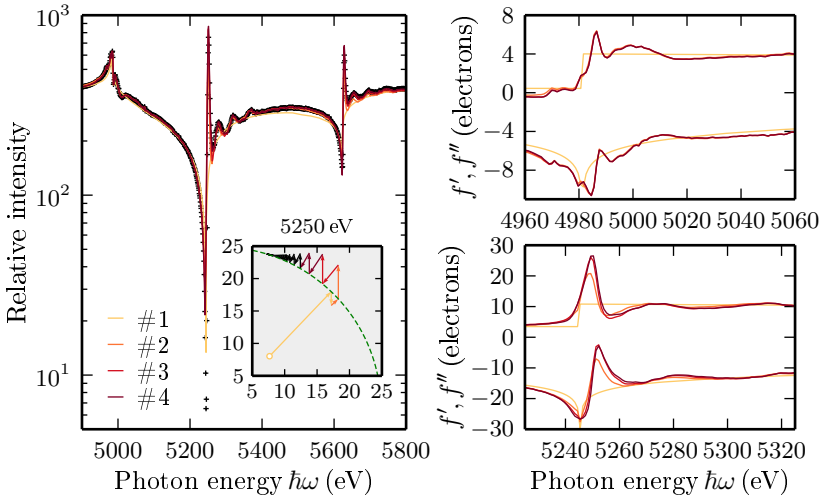

Fig. 3.10.: Visualization of the iterative algorithm to retrieve fine structure of the atomic scattering factors for barium and titanium in $BaTiO_3$. Shown are the measured (plus signs) and simulated intensity (solid lines) for the first iterations (left). On the right, the results for the obtained fine structure of the Ti-K edge (top) and the Ba-L_3 edge (bottom) are shown for the same iterations. The inset in the left plot shows the evolution of the simulated structure amplitude for a selected energy (5250 eV, close to the "white line") in the complex plane starting from tabulated (smooth) values (open circle) until convergence. The energy range was again split into two parts to separate fine structure of titanium and barium.

(LDR) [Kaw+14]. It is based on the fact that the logarithm of the structure amplitude can be written as

$$\ln F = \ln\left(|F|\mathrm{e}^{\mathrm{i}\varphi}\right) = \ln|F| + \mathrm{i}\varphi, \tag{3.7}$$

where φ is the unknown phase of the structure factor and $|F|$ is suspect to measurements. Both the structure amplitude and its logarithm fulfill the Cauchy-Riemann equations in the same regions [Roe65; Tan15]. Therefore the KK relations are valid also for the logarithmic expression. This means that the phase can be calculated from the intensity according to

$$\varphi(E') = -\frac{2E'}{\pi}\mathcal{P}\int_0^\infty \frac{\ln|F(E)|}{E^2 - E'^2}\mathrm{d}E, \tag{3.8}$$

as long as the structure amplitude does not occur to be zero anywhere in the complete spectral range. To avoid this problem and to take account for the limited spectral range that is accessible by a measurement, the knowledge of the smooth asymptotic behavior of scattering was used in this work. In particular, let I_s be the known, smooth part of the diffracted intensity which is calculated based on table data. If we introduce the quantity $I/I_\mathrm{s} = (|F|/|F_\mathrm{s}|)^2$, it will be one everywhere but in a small energy range. Moreover, $\ln\sqrt{I/I_\mathrm{s}}$ will be band-limited similar to the fine structure function $\tilde{\chi}$ which was introduced before. It can also be assumed that the ratio I/I_s is not zero far from the edge avoiding singularities. We can then rewrite Eq. (3.8) using $\ln\sqrt{I} = \ln\sqrt{I/I_\mathrm{s}} + \ln\sqrt{I_\mathrm{s}}$ as

$$\varphi(E') = \underbrace{-\frac{2E'}{\pi}\mathcal{P}\int_0^\infty \frac{\ln\sqrt{I/I_\mathrm{s}}}{E^2 - E'^2}\mathrm{d}E}_{\Delta\varphi(E')} \underbrace{-\frac{2E'}{\pi}\mathcal{P}\int_0^\infty \frac{\ln I_\mathrm{s}}{E^2 - E'^2}\mathrm{d}E}_{\varphi_\mathrm{s}(E')}. \tag{3.9}$$

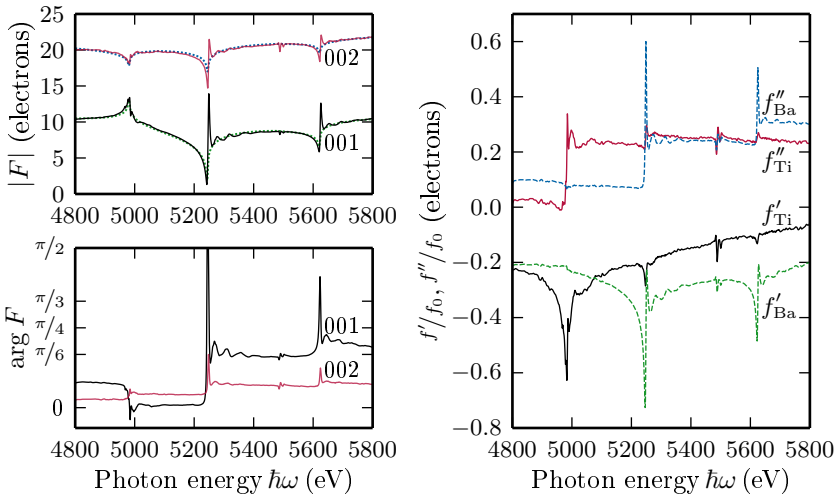

Fig. 3.11.: The result of using the LDR. The top left shows the measured vs. the smooth intensity for reflections 001 and 002 of BTO. The logarithm of the ratios is then used in LDR to obtain the phase for each reflection (bottom left). This way, the complex fine structure amplitude of the structure factor ΔF is obtained and distributed onto the different atomic scattering amplitudes by solving Eq. (3.11).

Here, φ_s (the second integral on the right) is the smooth phase which is known for each structure and whereas $\Delta\varphi$ contains only the phase shift due to fine structure oscillations. If now a good structural model was found, the calculated I_s will asymptotically describe the measured intensity as going away from the resonance. In this case, the integrand of the first term is band-limited and can be integrated on the measured energy grid using the same algorithms as for the KK transform shown above. This way, the complex structure amplitude can be derived and its fine structure part is obtained via

$$\Delta F = F - F_\mathrm{s} = \sqrt{I} \cdot \mathrm{e}^{\mathrm{i}(\varphi_\mathrm{s}+\Delta\varphi)} - F_\mathrm{s}.$$

The extracted phase of 001 and 002 reflection for the $BaTiO_3$ example can be seen in Fig. 3.11 (bottom left) together with the measured and calculated smooth intensity (top left).

If there are several resonant atoms in the structure and, hence, contribute to ΔF, several (at least as many) reflections need to be recorded to disentangle atomic fine structure functions for each atom [Cro+97; Hod+95]. For a certain atom j contributing to the structure factor, its contribution on the structure amplitude (recalling the dependencies on energy and scattering vector $\mathbf{K}$) is calculated by

$$\Delta F(\mathbf{K},E) = \frac{\partial F(\mathbf{K},E)}{\partial f_j(E)}\Delta f_j(E) \overset{\text{e.g.}}{=} \frac{\partial F}{\partial f_j}\tilde{\chi}_j(E) =: \mathcal{W}(\mathbf{K},E)_j\tilde{\chi}_j(E). \tag{3.10}$$

The quantity $\partial F/\partial f_j$ is called the crystallographic weight of atom j for a certain reflection. It depends on the structural model which is necessary to interpret DAFS spectra. Performing the sum over j and including the measured data of a set of reflections $\mathbf{K}_i$, we obtain the following set of linear equations

$$\begin{pmatrix} \Delta F(\mathbf{K}_1, E) \\ \vdots \\ \Delta F(\mathbf{K}_i, E) \\ \vdots \end{pmatrix} = \begin{pmatrix} \frac{\partial F(\mathbf{K}_1,E)}{\partial f_1(E)} & \cdots & \frac{\partial F(\mathbf{K}_1,E)}{\partial f_j(E)} & \cdots \\ \vdots & \ddots & & \cdots \\ \frac{\partial F(\mathbf{K}_i,E)}{\partial f_1(E)} & & \frac{\partial F(\mathbf{K}_i,E)}{\partial f_j(E)} & \cdots \\ \vdots & \vdots & \vdots & \ddots \end{pmatrix} \cdot \begin{pmatrix} \tilde{\chi}_1(E) \\ \vdots \\ \tilde{\chi}_j(E) \\ \vdots \end{pmatrix}, \tag{3.11}$$

for each energy value E. If the matrix $\mathcal{W}(\mathbf{K}_i, E)_j$ is quadratic, the fine structure functions $\tilde{\chi}_j$ for each resonant atom can be obtained by inversion of the matrix. If there is data of more reflections, linear regression can be used reducing the error on the result. Figure 3.11 shows the spectra of titanium and barium for BTO obtained by this method. Two reflections, 001 and 002, have been used to disentangle the fine structure of both atoms for the whole energy range. This approach automatically describes the measured intensity correctly. The resulting energy dependencies of the atomic scattering amplitudes in Fig. 3.11 show the expected behavior at the corresponding edges (in comparison to Figs. 3.9 and 3.10). But, looking more closely, also a remaining mixing of the spectra can be seen: small traces of the barium edge are visible in the titanium spectrum and vice versa. This can be due to uncertainties in the structural model. In particular, Debye-Waller factors are not known precisely and cannot be determined unambiguously from two reflections.

It should be noted that this LDR approach can only be employed when the spectra are corrected for absorption or do not exhibit any absorption effects like in the present case of thin films. Also, it is worth mentioning that extracting fine structure from these reflections can give information on the absolute polarization of the ferroelectric film. Above, we assumed the measurement of 001 and 002 reflection which corresponds to the titanium atom as well as the polarization pointing away from the surface. The calculations can be repeated based on the opposing reflections ($00\bar{1}$ and $00\bar{2}$). However, this yields much stronger mixing of the two fine structures (barium and titanium) spectrum indicating an inconsistent model.

4. Results and Discussion

The purpose of this chapter will not only be to present results of crystal structure analyses using RXD, but also to illuminate some of the different strategies to attain these results. In particular, the differences which occur for materials in the different kinds of crystalline state will be highlighted. Again, in doing so, this work does not aim to give a comprehensive guide but to point out some of the possibilities which may be interesting for the material scientist.

4.1. Polycrystalline materials

Resonant x-ray diffraction measurements on polycrystalline samples certainly belong to the most difficult group of those performed in this work. This concerns, in particular, the interpretation of the data. Resonant effects in x-ray diffraction are additive and therefore most notable on the relative scale when the actual reflection is weak (at least in the nonresonant case, see e. g. Fig. 4.1 on the right). On the other hand, x-ray powder diffraction offers a rather low signal to noise ratio. Furthermore, in powder diffraction peak, overlap often occurs and the measured diffraction spectra are usually dominated by absorption effects, as will be shown later. For these reasons a certain expertise on powder diffraction as well as an powder diffraction optimized beamline are required for successful extraction and interpretation of resonant diffraction data from polycrystals and there are limitations on the opportunities for the measurement for example of weak (or forbidden) reflections or of Friedel pairs.

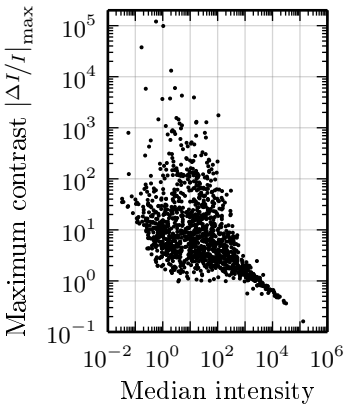

Fig. 4.1.: Resonant contrast calculated for all reflections of RbH_2PO_4 with $|\mathbf{K}| < 15.71\,\text{Å}^{-1}$ plotted vs. the median intensity in an energy range close to the Rb-*K* edge.

Nevertheless, resonant diffraction has been used to get a deeper insight into the structure of polycrystalline materials since long. One of the first papers that were published on DAFS dealt with the investigation of powder [Pic+93] and demonstrates the extraction of XAFS like information from those measurements. In terms of signal intensity, DAFS hardly can compete with XAFS, but the selection of certain

spatial frequencies, as it is done via diffraction, allows to discriminate atoms of the same species that exist in different crystallographic phases or occupy different crystallographic sites. Little later, a book chapter was devoted to the topic [CW93], being focused more on contrast enhancement of atoms with similar (or equal) number of protons. A review on the different aspects of resonant powder diffraction appeared only recently [Pal+12]. It emphasizes the two strategies of the method in which also the two previously cited papers differ: (*i*) analysis of full diffraction patterns including many reflections for a small set of resonant energies and (*ii*) analysis of full energy scans across an absorption edge of one or more atoms for a small set of reflections. In this work, I performed all experiments in the frame of the latter strategy. The following applications will be focused on pointing out the problems of powder RXD and possible solutions to them as well as include results of structure refinement based on DAFS.

4.1.1. Application of DAFS for powders for the example of a mixed-valence compound $EuPd_3B_x$

In this introductory example, the study is focussed on a valence shift of the rare earth metal europium in the compound series $EuPd_3B_x$. Valence shifts are often observed in rare earth metals and are determined by various external es well as internal (structural) parameters. The insertion of the light element boron into $EuPd_3$, which crystallizes in the Auricupride (AuCu3) structure type, is one example of such internal parameter and has recently been studied in detail by Gumeniuk et al. experimentally as well as theoretically [Gum+10]. In this work, an increasing lattice parameter of the cubic phase could be observed up to values of $x \leq 0.53$. Together with the assumption of a single phase, polycrystalline sample, which was supported by powder diffraction measurements, it implies that this value is the maximum occupancy of boron which is situated in the center of the cube defined by europium atoms. Therefore, the new structure type corresponds to $CaTiO_3$ with boron formally occupying the titanium position.

One of the main experimental results presented in the mentioned article is a valence shift of europium from Eu^{3+} towards Eu^{2+} which sets in at a boron content of $x > 0.22$. It was visible in an edge shift in XAFS which is a very convenient tool to assess the absolute valence state of heavy ions. A second interesting finding in this work is the formation of a $2 \times 2 \times 2$ superstructure at slightly higher boron contents ($x > 0.35$) which is shown in Fig. 4.2.

The questions stimulated by these results, are

(i) Why a valence shift is seen only for boron content above 0.22

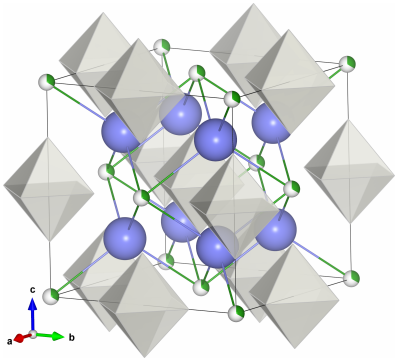

Fig. 4.2.: Cubic unit cell of $EuPd_3B_x$ for $x > 0.35$ where a $2 \times 2 \times 2$ superstructure forms. Empty Pd octahedra are shown in grey and Eu atoms in blue. The partially occupied boron positions are indicated with partially filled green spheres. They are also surrounded by Pd octahedra (not shown) which are larger than the empty ones. See [Gum+10] for details.

(ii) If a valence shift is strictly correlated with a super structure

(iii) Whether europium exists in different (divalent and trivalent state) in the sample

(iv) If the powder is phase pure for $x \leq 0.53$ (as indicated by *x-ray diffraction* (XRD) in [Gum+10])

The latter two points are closely connected and could be addressed using DAFS as well as point (ii): If it would be possible to measure DAFS at the europium edge for one of the superlattice reflections and to extract the fine structure, any differences in comparison with (averaging) XAFS would affirm (ii) and (iii) and negate the last point. However, the clear shift in diffraction peaks with boron content x as published in that work nicely follows Vegard's law [VD28] and therefore doesn't leave much space for the assumption of multiple phases. What remains for a study with DAFS is to test for the presence of europium in an amorphous matrix and checking point (iii) which corresponds to a cross-check of the provided structure model. Since the europium sublattice does not exhibit the superstructure, there should be no DAFS signal seen in the superlattice reflections.

To preempt the result of the DAFS investigation on $EuPd_3B_x$, only a rather small statement could be made that is about the verification of the mixed-valent europium as part of the crystal structure. Hence, there is no indication that contributions from amorphous regions to XAFS need to be taken into account, as expected. The reasons for not having come closer to answers of the points (i...iv) above were of practical nature and will be discussed here. The presentation of the data at this point is nevertheless motivated due to their high data quality and the good agreement with theory.

The main issues that need to be considered for DAFS measurements on powders include the following:

Orientational distribution and size distribution of crystallites: Similar to conventional powder diffraction measurements, the intensity of each measured reflection depends on the amount (volume) of crystallites (grains) that satisfy the Bragg condition (2.42) and scatter in the direction of the detector. Therefore the relative intensities can be distorted if the crystallites exhibit a preferred orientation ("texture"). Furthermore, if only a few crystallites participate in diffraction, an additional variance of the measured intensity can be expected similar to shot noise. It is important to note that for DAFS the influence of preferred orientation, is actually only a minor problem because, usually, only relative changes of one Bragg reflection are analyzed at a time. If the crystallites become large, on the other hand, particular care needs to be taken to ensure an averaging over a large number of grains. In principle, the number of scattering grains also follows the Poisson distribution and it is highly unlikely, that the number of contributing grains is maintained during an energy scan, where the angles have to be adjusted according to Bragg's law and the beam path changes. Therefore, there is no sence in recording (many) more photon counts than the number of contributing crystallites which is a problem, since DAFS, similar to xafs, is based on the analysis of small relative changes of relatively strong reflections with energy. The easiest way to obtain a good sampling of scattering grains is certainly the rotation of the sample through different axes providing most orientations and to the capture of a large (full) part of the Debye-Scherrer rings (see Fig. 4.3). Also it turned out in this work that it is preferable to perform the same kind of rotation for each energy step or to synchronize the rotation with the measurement.

Sample homogeneity: Due to the changing pathway of the x-ray beam during energy scans, small sample inhomogeneities can easily fake the small oscillations which are subject of data interpretation in DAFS. This can be especially problematic when measuring in transmission geometry and when the resonances of interest lie in the rather soft x-ray region. Then, the sample thickness must be very small and might be hard to control. Also less material in the beam again means a worse grain sampling.

Absorption and self-absorption: As it was introduced in Section 2.2.2, the measured intensity suffers loss due to absorption which demands a thorough correction, since the absorption shows a similar, non-trivial fine structure as the DAFS spectra. Usually the powder (or also singlecrystalline) sample needs to be considered as homogeneous with a known shape to allow for the integration of partial scattering from all volume elements (voxels). In this work, several ways to perform an absorption correction, i.e. to

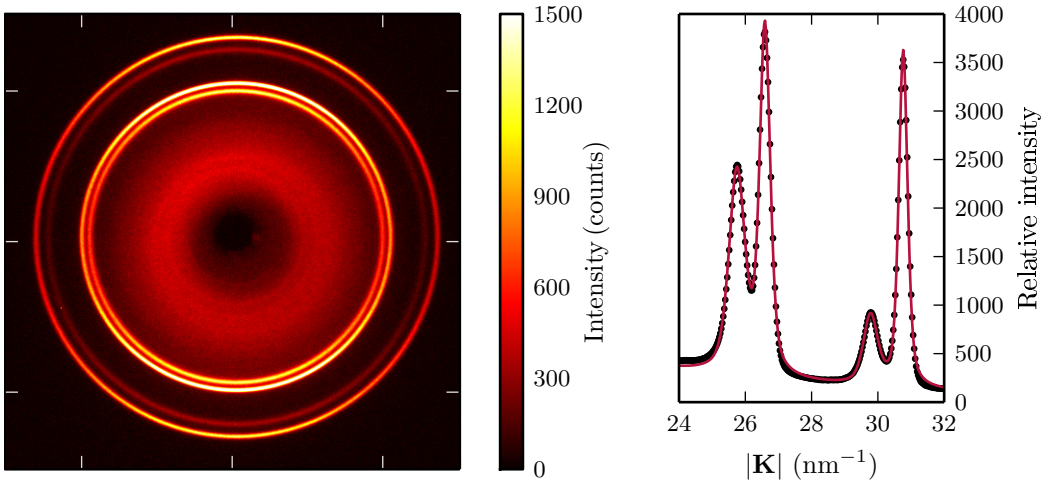

Fig. 4.3.: Diffraction pattern from a mixture of $EuPd_3B_{0.44}$ and LiF at a Eu-resonant energy of 6950 eV where LiF was admixed to serve as a reference for absorption correction. Left: raw intensity on a 2d-position sensitive detector (PSD). A pair of weak rings can be seen in the inner halo and are cause by the third harmonic of the monochromator. Right: result of calibration and azimuthal integration performed using pyFAI [Ash+15] (black dots) and peak fitting using pseudo-Voigt profiles (red lines) for the section of the four main rings (from low to high $|\mathbf{K}|$: $EuPd_3B_{0.44}$ 111, LiF 111, $EuPd_3B_{0.44}$ 002 and LiF 002 reflection).

obtain the absorption spectrum, have been tested (see Section 3.2.2): via measurement of transmission, measurement of fluorescence, admixture of a reference compound. Another way is to simulate absorption as part of the data evaluation or to measure spectra from several reflections to gain data redundancy and, this way, to tell apart absorption from diffraction fine structure.

Geometry, Background: Especially during powder measurements, the geometry of the experiment is crucial in order to obtain interpretable data. The Lorentz factor which is well known from powder x-ray diffraction [Rey86; AM11] and takes account of **K**-space integration and solid angle covered by the detector, results in a strong decline of diffraction intensity with higher scattering angles. It is common to perform powder XRD at higher x-ray energies to avoid this problem. However, this degree of freedom does obviously not exist in resonant diffraction and it might be necessary to perform the measurements at rather low energies. This also entails the problem of an increased diffuse background scattering which is why an evacuated beam path is obligatory to measure weak reflections.

In this example, we followed the concept of mixing a reference compound into the powder sample in order to obtain the absorption spectrum. To obtain the full Debye-Scherrer rings shown in Fig. 4.3, the measurements were performed in transmission geometry. They were carried out at the beamline "PHASE" of the Kurchatov Center for Synchrotron Radiation in Moscow using a customized transmission setup. The samples were a homogeneous mixture of

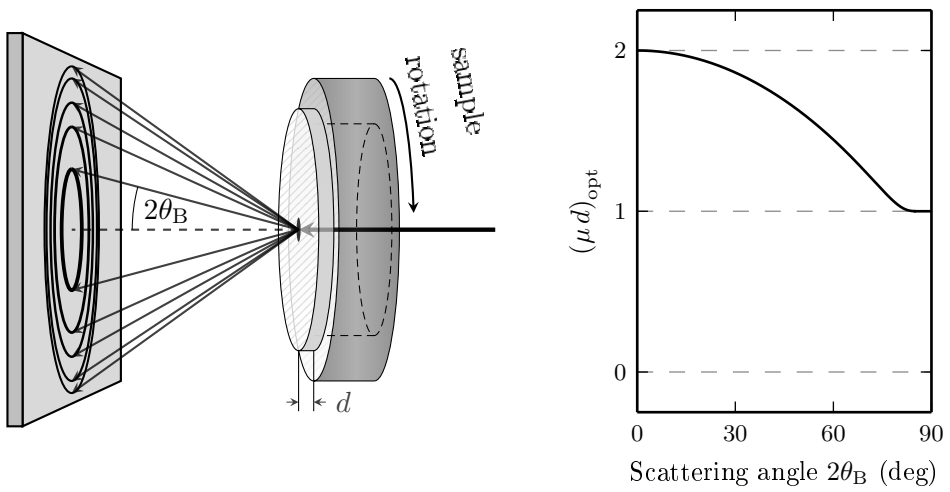

Fig. 4.4.: Left: Scattering geometry of (resonant) powder diffraction experiments in transmission mode. The sample is powder pressed into a pill and placed on a rotary positioner to maximize grain sampling statistics. Right: the product of absorption coefficient and thickness μd to maximize the diffraction intensity in the geometry given on the left.

$EuPd_3B_x$ and LiF pressed into a tablet. LiF was selected for several reasons: a small unit cell (few reflections), low absorption, easy to handle, small grain size (5 µm). The tablet has been mounted on a rotary positioner with large aperture with the rotation axis perpendicular to the tablet face and parallel to the beam (see Fig. 4.4). The equation for absorption similar to Eq. (2.44) can be obtained by integration as it was described in Section 2.2.2 but it turns out to be more complicated in the case of asymmetric transmission geometry [LLH06]. However, in our special case, we can fix the angle of incidence to be $\alpha = 0$. Therefore, the exit angle equals the scattering angle $\beta = 2\theta_B$ The Absorption factor becomes

$$A(E, d, \theta_B) = \frac{1}{\mu(E)(1 - \cos 2\theta_B)} \left[\exp(-\mu(E)d) - \exp\left(-\frac{\mu(E)d}{\cos 2\theta_B}\right)\right]. \tag{4.1}$$

To find the ideal thickness d of the sample slab, one needs to consider that the scattered intensity will also be proportional to the illuminated volume and therefore to the thickness: $I \propto d \cdot A(E, d, \theta_B)$. Hence, the ideal thickness is obtained by computing

$$\frac{\partial}{\partial d}\left[d \cdot A(E, d, \theta_B)\right] \stackrel{!}{=} 0,$$

resulting in

$$\exp\left(\mu d(\sec 2\theta_B - 1)\right)(1 - \mu d) + \mu d \sec 2\theta_B - 1 = 0.$$

This equation can easily be solved numerically and the non-trivial solutions of μd where the intensity is maximized is shown on the right hand side in Fig. 4.4. One can see that the ideal sample thickness varies between the one- and twofold of the attenuation length depending on the scattering angle. In the present case, the targeted absorption edge was Eu-$L3$ with an energy of 6977 eV which results in rather strong absorption and small optimal sample thickness of about 5.6 µm. The admixture of the light reference LiF also relaxed this situation: a mixing

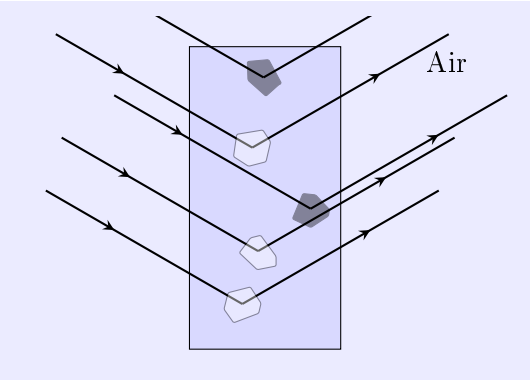

Fig. 4.5.: Illustration of the effect of (additional) self-absorption within the crystallites. A reference material (e. g. white crystallites) inside the same powder sample and transmission data will exhibit the same kind of absorption according to the pathway through the sample. The crystallites under study (here black), which are illuminated with resonan x-rays, involve an additional, intrinsic absorption path.

ratio LiF:$EuPd_3B_x$ of approximately 9:1 was chosen aiming to have an equal |structure factor| to unit cell volume ratio in accordance to an equal peak intensity as in Eq. (2.39). This also leads to a reduced absorption and $2/\mu \approx 51\,\mu\text{m}$.

Both powders were small grained and an optically homogeneous mixture was obtained during sample preparation. Since the scattering angles of the reflections from reference and $EuPd_3B_x$ are close, the x-ray beams diffracted by the two substances should traverse very similar paths and, hence, suffer approximately the same absorption. However, the corrected DAFS spectra obtained by normalization onto the reference reflections could not be reproduced using absorption spectra and Kramers-Kronig relations (see Fig. 4.6). The difference is such that it can not be explained by a different chemical environment of those atoms probed by DAFS on the one hand, and those probed by XAFS on the other hand. In this case, DAFS would only contain information of atoms that have a periodicity according to the lattice spacing of the reflection and therefore slight differences in the oscillations can be observed compared to XAFS but the general progression should be the same.

It turned out that, for an adequate description of the measured data, it is necessary to take into account self-absorption coming on top of the bare absorption by the sample as a whole. The situation is visualized in Fig. 4.5: while the beam path through the absorbing sample (blue) is the same for reference and crystallites of interest, the attenuation during diffraction by a mosaic block of the crystallite can be much different. In particular, LiF is hardly absorbing and, besides, does not show any features near the europium edge. X-rays diffracted by $EuPd_3B_x$, on the other hand, undergo an additional self-absorption which is exclusively due to the diffracting crystallite and can, in general, show a different spectral shape than that of the average sample.

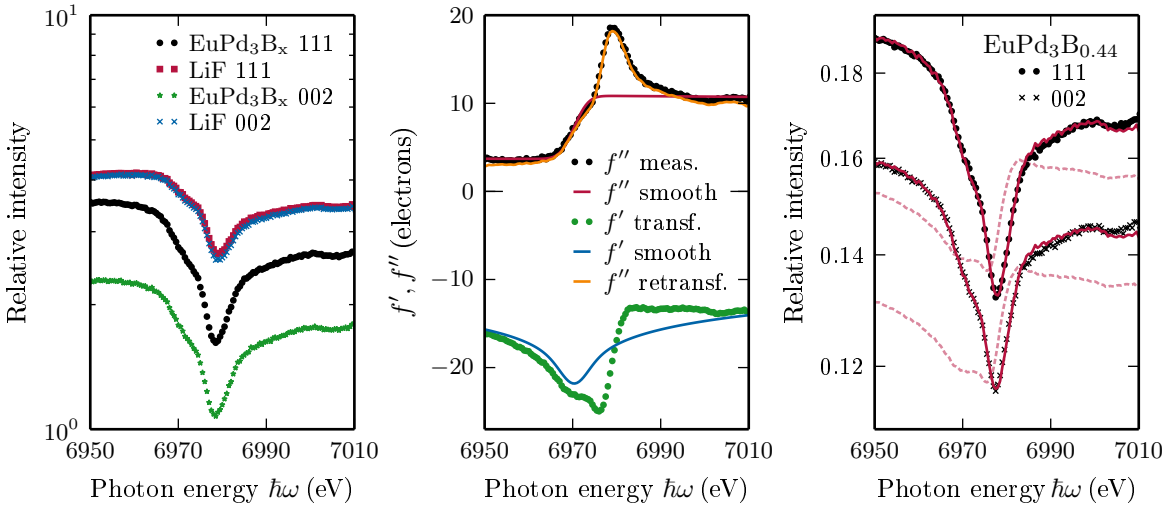

Fig. 4.6.: Left: peak intensity as obtained from fitting the radial diffraction profiles for the four maxima in Fig. 4.3. Middle: the illustration of KK transform of the imaginary part f'' of the europium scattering amplitude, obtained from the reference (LiF) peaks, into the real part f'. Smooth lines are the general "background" progressions as they are calculated for isolated atoms in vacuum and tabulated (see Section 3.3.1). These are subtracted during the KK transform. Right: absorption corrected peak intensity (black dots) as well as the calculations based on the results of KK transform and fitting the effective self-absorption depth. The best fit result without taking into account self-absorption is seen as dashed lines.

Even though it is not possible to tell in what kind of geometry the self-absorption process takes place for each crystal, it was possible to describe the measurements correctly by multiplying an additional absorption factor corresponding to Bragg geometry (Eq. (2.44)) and an effective thickness of the diffracting mosaic block of 0.8 µm (see Fig. 4.6). The additional self-absorption correction is also necessary when the absorption is extracted from transmission measurements, as will be seen in the next example. One can conclude that the agreement of the corrected intensity and the diffraction fine structure calculated from the absorption spectra is excellent. Similar results have been obtained for samples with $x \in 0.15, 0.17$. This essentially means that the used structural model is consistent with the data and no extra information can be gained from DAFS, except that europium mostly exists in this crystal structure, which was expected. However we gained experience about proper absorption correction using a reference powder. The advantage is that the reference beam, in contrast to transmission measurements, probes a similar region of the material and that the obtained absorption is not distorted as in the case of, e. g., fluorescence. To gain more information on the questions mentioned before, a similar study on the superlattice reflections would be necessary but these could not be accessed in the present, non-optimized setup since they were too weak to be distinguished from the background. Furthermore, if the structural model is correct, there would still no information to be obtained on the europium edges since the europium sublattice does not exhibit any superstructure. Since the boron-filled palladium octahedra show a different volume than the unfilled octahedra (grey in Fig. 4.2), only measurements on an palladium edge would allow

to exclusively study the super structure and to discuss question (iv) which motivates further measurements.

In summary, it was shown here that the measurements of Bragg intensity as a function of energy are well understood and can be modeled to high detail. The challenges in powder DAFS have been outlined together with possible solutions. The application of the method has been described in detail. This can serve as a guide to such kind of measurements. It was shown that additional self-absorption needs to be considered if the absorption correction is performed by normalization to Bragg reflections of a reference substance. In the case of $EuPd_3B_x$, a reduction of background from air scattering will allow to perform measurements on superlattice reflections. This is due to the absence of Bragg-Brentano or other focussing which exists in laboratory diffractometers. Future measurements at the Pd-K edge would allow both the reduction of air scattering and selected probe of the superstructure.

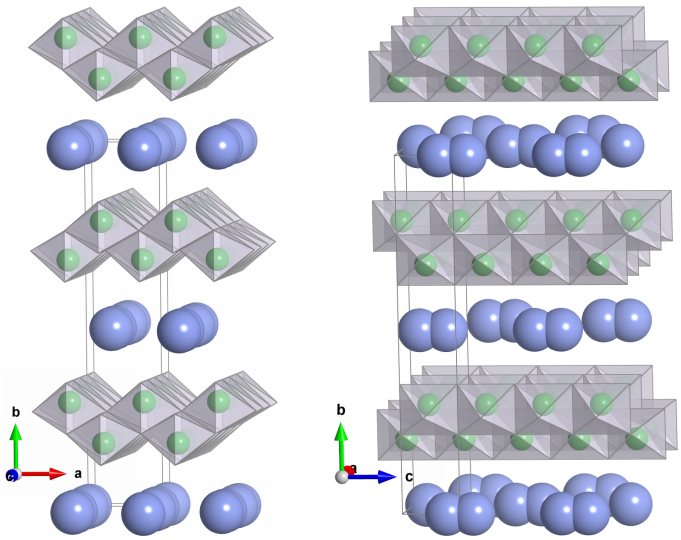

Fig. 4.7.: The structure of LHT in a-b projection (left) and b-c projection (right). The unit cell is drawn with thin lines. A large layer-spacing ($\approx 9.2\,\text{Å}$) in c-direction between sheets of connected TiO_6 octahedra can be seen which is half-filled with hydrazinium ions ($N_2H_5^+$, only N_2^- ions drawn as blue spheres).

4.1.2. Titanium environments and heavy ion intercalation in layered hydrazinium titanate

The second example of a polycrystalline substance which was studied in this work is Layered Hydrazinium Titanate (LHT). It is was discovered in 2011 and showed a high adsorption performance for a large part of the periodic table and is therefore interesting for application, e. g., as a filter for heavy metal ions from their solution [Bri+11]. The adsorption abilities of LHT origin from the redox properties of the hydrazinium molecule but also from the layered structure of LHT ($(N_2H_5)_{1/2}Ti_{1.87}O_4$) offering large surface area and structural voids at the same time (see Fig. 4.7). The hydrazinium molecules (blue, only nitrogen) are sandwiched between double layers of distorted, edge-sharing [TiO_6] octahedra having a large spacing of $\approx 9.2\,\text{Å}$ resulting in pseudochannels along the c axis that are half-occupied by the hydrazinium molecules. The crystal structure shown in Fig. 4.7 was obtained via Rietveld refinement [Rie69] of x-ray powder diffraction data. It does only contain one type of titanium environment – the distorted octahedron. However, several experimental data in [Bri+11] indicate the existence of a short Ti=O titanyl bond in the powder sample which is not contained in the crystal structure. Indications for titanyl bonds were found by x-ray spectroscopy as well as by *fourier transform infrared spectroscopy* (FTIR). In particular, these are a characteristic peak in the pre-edge region of *x-ray absorption near edge spectroscopy* (XANES) at 4970.5 eV and a maximum in the Fourier-transformed EXAFS-function $\tilde{\chi}(R)$ (EXAFS) at a short distance of 1.66 Å. The titanyl bond was explained with 5-fold (square-pyramidal) coordination of titanium (Ti^V) by oxygen and attributed to defects resulting from the truncation of the

titanate sheets in LHT which consequently would not share the periodicity of the lattice and therefore explain the result of Rietveld refinement.

An observation of the mentioned features in DAFS spectra would determine a Ti^{V} coordination geometry as intrinsic element of the crystal structure and therefore contradict with the current structure model. Using DAFS, it is possible to gain the same information as from XANES and EXAFS selectively for those atoms that show the periodicity probed by the reflection. Therefore, if the titanyl bond does not occur in the crystal structure, as was concluded before, the DAFS spectra should not contain the corresponding maxima which were seen in XANES and EXAFS.

For this reason, DAFS measurements were performed on different reflections of LHT in a polycrystalline as well as a nanocrystalline form. The latter is expected to exhibit a higher degree of defects due to truncation and therefore larger interface volume. However, due to small crystal size its diffraction peaks are very weak.

Nanocrystalline LHT – amorphous vs. ordered volumes

DAFS measurements on nanocrystalline LHT ("LHT-nano") were performed in the XANES region of the Ti-K edge to compare the near edge spectra of periodic structure against the average sample. The measurements have been performed at the beamline BW1 at the DORIS synchrotron at DESY (Deutsches Elektronen-Synchrotron), Hamburg [Fra+95], using the same transmission geometry as shown in Fig. 4.4. Only one reflection could be observed during the experiment which vanished in fluorescence background as soon the x-ray energy was set to a value above the absorption threshold. For this reason, it was necessary to reduce the background and therefore no pixel detector could be used. A soller slit [SS65] was placed between sample and detector to reduce its acceptance angle and isolate the radiation that comes from the sample. Furthermore, a silicon drift diode (SDD) energy-dispersive detector was used to separate the fluorescence photons from elastically scattered photons. Fig. 4.8 shows a typical energy distribution of photons which have been scattered from the LHT-nano sample at an incident photon energy of 5400 eV. The intense peaks on the right correspond to titanium K_α (4505 eV, 4511 eV), K_β (4932 eV) emission lines as well as the elastically scattered photons (5400 eV, containing Compton scattering). The maximum in the middle stems from argon gas in the atmosphere and was not considered. The spectra were fitted using asymmetric profile functions as described in [Egg04; Egg+06] (red line). During the actual (resonant) measurements, the incident photon energy is close to the edge and therefore the corresponding maximum in the detector response (Fig. 4.8) strongly overlaps with the one of the K_β emission line. This problem is inherent to RXD and can be solved by preliminary

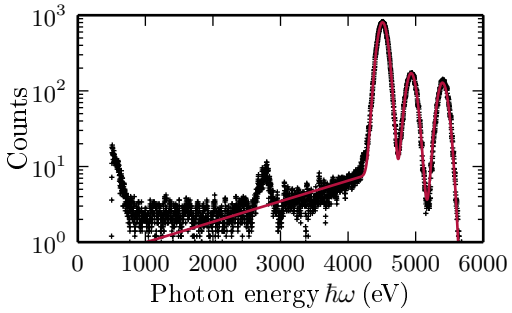

Fig. 4.8.: Typical spectrum measured during RXD with an energy dispersive detector: here corresponding to LHT illuminated with 5400 eV photons. The data feature three intense peaks (f.l.t.r: Ti K_α, Ti K_β, elastic scattering). The peak near 3000 eV is fluorescence from argon in the air. The increase on the low-energy limit is due to electronic noise in the detector.

characterization of the intensity ratio of K_α to K_β line which should stay fixed during the measurement as they origin from the same excitation (of the K-1s shell). In the present case, the ratio was $I_{K_\beta}/I_{K_\alpha} = 21.8\%$ and this fraction of K_α fluorescence was subsequently subtracted from the integral over the range containing K_β and elastic photons resulting in the elastic part only. This way, it was possible to monitor the 020 diffraction peak of LHT-nano along across the Ti-K absorption edge (see Fig. 4.9 left) by fitting a sum of Gaussian peak and Lorentzian shaped background attributed to small angle (diffuse) scattering from the sample. At the same time, absorption spectra have been obtained via titanium fluorescence as well as by using an additional silicon diode detector recording the transmission at zero scattering angle. The resulting spectra are shown in the middle plot of Fig. 4.9. As expected, absorption spectra extracted from transmission and fluorescence coincide. The energy dependence of the Bragg intensity is slightly different exposing the contribution of DAFS. Interestingly, the diffuse background follows nearly the same energy dependence. Its intensity is proportional to the sum of scattering power of all atoms and is therefore also related to the titanium fine structure. The absorption was again calculated from Eq. (2.44) after extraction of μ. The absorption-corrected spectrum is shown on the right in Fig. 4.9. Furthermore, using the linear absorption coefficient μ and Kramers-Kronig relations, the DAFS spectra, assuming that all titanium atoms are part of the crystal structure, was calculated and drawn into the same plot for comparison. It should be noted that, given the setup at BW1 which was not optimized for this measurement, two days were consumed for data acquisition in order to achieve a data quality as seen in these plots. A discussion of differences in spectra obtained via XAFS and DAFS (seen on the right of Fig. 4.9) is limited by the effect of photon counting statistics on the corrected data. Still, within the error margins, no discrepancy between XAFS and DAFS spectra can be seen. This means that no indication was found that the crystalline part of LHT-nano shows a different titanium XANES than the sample average. Hence, a Ti^V coordination or at least the short (Ti=O) titanyl bond seem to belong to the crystal structure of LHT. A stronger signal or longer exposure would further allow to study the extended

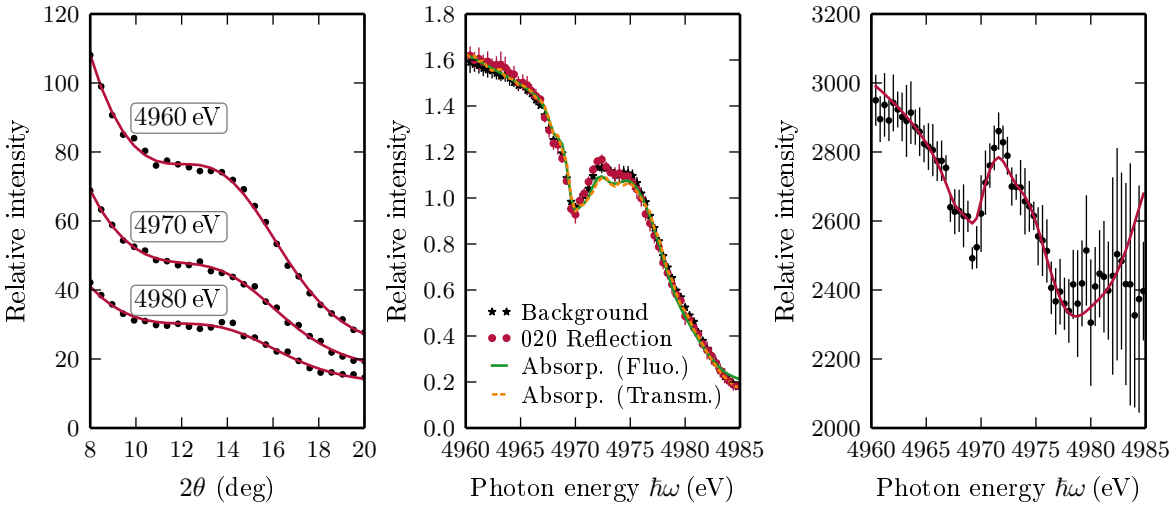

Fig. 4.9.: Diffraction patterns of the 002 reflection from LHT-nano for selected energies (left); peak height from fitting diffraction patterns as function of energy next to absortpion data in the titanium pre-edge region (middle); absorption corrected DAFS spectrum of the 002 reflection (right, black dots) against the progression calculated from absorption data (red line).

DAFS region and to extract bond-distances as it was done in the following for the case of LHT-bulk.

Polycrystalline LHT

A similar conclusion can be drawn by comparison of the XANES spectra of LHT-nano and an LHT sample with moderate grain size ($1 \ldots 10\,\mu m$) further referred to as LHT-bulk. Since the periodic regions of LHT-bulk are much larger than those of LHT-nano ($< 100\,nm$), a much smaller fraction of surface volume can be expected. Therefore, in XANES spectra, the titanyl peak which is attributed to compensation dangling Ti-O bonds at the surface of the truncated nanocrystals should be weaker in the case of LHT-bulk. A comparison of XANES spectra of both samples is shown in Fig. 4.10 (left) and reveals that this is not the case: XANES spectra for bulk and nano samples practically coincide. Furthermore, the purely crystallographic spectrum has been obtained via DAFS measurements on the 130 reflections on bulk LHT. The larger crystallite size and therefore higher reflection intensities allowed measurements in a wider spectral range (see Fig. 4.10 middle) and the extraction of dispersion fine structure from this reflection. The near edge region is also shown on the left in Fig. 4.10 (black dots) and agrees well with the sample-averaged XANES spectra. On the right in Fig. 4.10, Fourier transforms of the extended XAFS oscillations ($\tilde{\chi}(k_{el}) \xrightarrow{FT} \tilde{\chi}(R)$) are shown: k_{el} is the wavevector (momentum) of the photoelectron and can be calculated given the ionization threshold (edge energy) E_0 via $\hbar\omega - E_0 = {}^{(\hbar k_{el})^2}/_{2m}$ and $\tilde{\chi}$ is the difference between the spectrum showing fine structure oscillations and the smooth progression calculated for

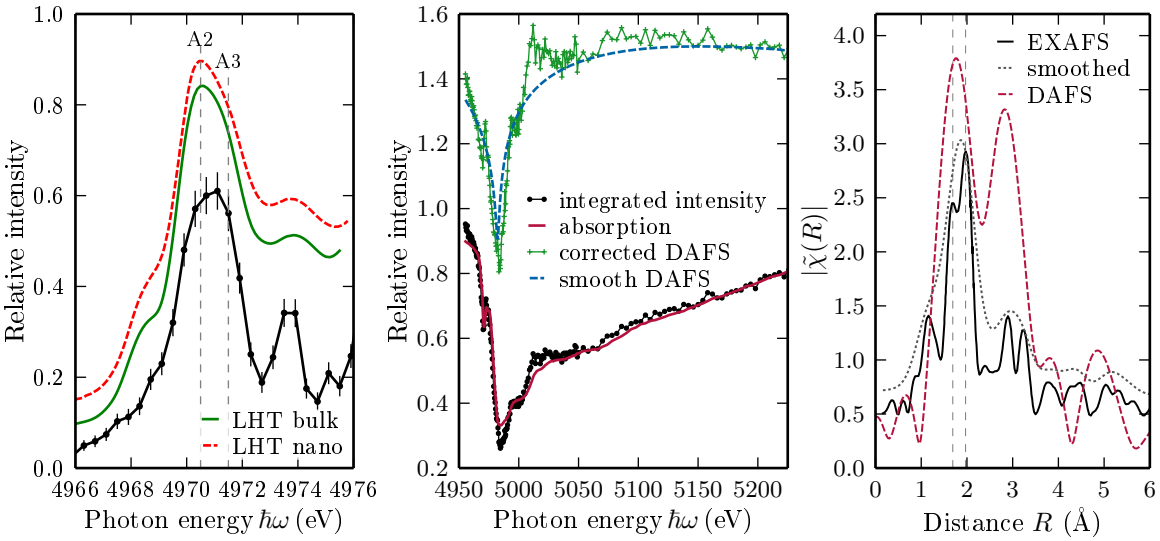

Fig. 4.10.: Left: XANES spectra of LHT-nano and LHT-bulk compared the one reconstructed from DAFS (black dots) on the 130 reflection of LHT-bulk. Middle: Energy dependent integrated intensity of the 130 reflection along with extracted absorption and the absorption corrected spectrum. Right: Fourier transform of the fine structure function $\tilde{\chi}(k)$ into R-space obtained from DAFS (dashed line) and from XANES on LHT-nano (back solid line).

an isolated atom. The extraction of the fine structure function $\tilde{\chi}(k)$ from DAFS spectra is explained in Section 3.3.2. Its Fourier transform ($\tilde{\chi}(R)$) is related to the density of interatomic distances involving the absorbing atom (herein titanium). The EXAFS spectrum of LHT-nano features a double-peak which has been attributed to the different Ti-O coordination geometries [Bri+11]. One can clearly see the short titanyl bond at 1.66 Å and the bond length corresponding to octahedral coordination at 1.95 Å marked with dashes lines in Fig. 4.10. The spectrum obtained via DAFS shows much lower resolution in R-space which is a result in a low counting statistics. Therefore, only one maximum could be resolved at the position formerly taken by the double peak. However, looking at the center of mass of the less well resolved maximum obtained by DAFS ($R = 1.75$ Å), it becomes clear that it cannot be explained by a set of bonds with a minimum length of 1.95 Å which is the case in the crystal structure model of LHT. For comparison, the EXAFS spectrum of LHT-nano has been smoothed with a Gaussian kernel to imitate a measurement with lower resolution. It can be seen that both peaks of the spectrum stemming from DAFS are reproduced by the smoothed spectrum from EXAFS. In conclusion, one can state that the titanyl bond (Ti=O) with a length of approximately 1.66 Å is structural and that there is no indication that the purely crystalline fraction of titanium atoms in LHT feature strongly differing x-ray absorption spectra than the bulk average. A possible reason is that the positively charged hydrazinium ion needs negatively charged titanate sheets for charge compensation. It was stated in [Bri+11] that this it most probably accomplished by titanium vacancies in agreement with the results of Rietveld refinement. Therefore, defects in the titanate sheets should correlated with the

crystal structure and their compensation might involve titanyl bonds, even though this would be more likely to occur for the case of oxygen deficiency.

Intercalation of selenium into LHT

It was mentioned before that LHT has strong potential for being used as an adsorbent for a large variety of ions. The effect of adsorption on the structure of LHT is not yet known. Since there are fairly large voids in the half-filled pseudo-channels in the LHT structure, it should allow accommodation of additional atoms. On the other hand, the due to reductive properties hydrazinium reacts with foreign ions which results in its replacement/consumption. Therefore, one part the investigation of LHT was focused on the process of heavy ion intercalation and its impact on the crystal structure. Several samples with different adsorbates have been synthesized by S. N. Britvin and provided for RXD measurements. The most interesting results have been obtained for the intercalation of selenium after mixing with diluted selenous acid (H_2SeO_3). The incorporation of selenium from the acid into LHT will take place via two different ways which are due to the different (chemical and structural) processes mentioned above. A certain part of the selenite ion will be reduced by the hydrazinium ion:

$$H_2SeO_3 + N_2H_5{}^+ \longrightarrow Se^0 + N_2 + 2H_2O + H_3O^+. \tag{4.2}$$

Furthermore, part of the deprotonated selenite atom can be adsorbed into the interlayer gaps of LHT. This would result in two different oxidation states of selenium present in the structure.

In order to analyze the structure of LHT after intercalation, DAFS measurements can give specific answers. While EXAFS already yields typical bond lengths, it is not clear if the results would be related to the crystal structure or to selenium in other environment (e. g. remaining reactant). It is important to emphasize, that DAFS can give two separate answers in such cases:

(i) whether the foreign ion has been accommodated into the structure and, if so, at which crystallographic position it settled,

(ii) how does the local structure (neighborhood) of the incorporated ion look like.

The first item can be answered base on the general progression of the atomic scattering amplitude of the resonant atom (see Fig. 2.3). With increasing photon energy, the real part undergoes first a gradual decrease and an increase above the edge. The imaginary part, on the other hand, exhibits a positive step. Both will contribute to the energy dependence of

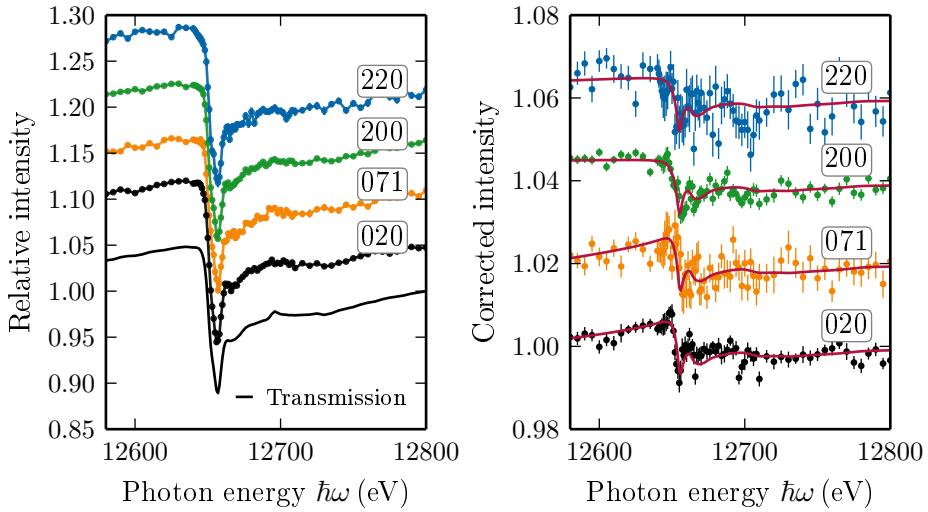

Fig. 4.11.: Left: Measurements of the integrated intensity of 020, 071, 200 and 220 reflections from LHT-9 bulk as well as the intensity of the transmitted beam (000 reflection, solid line). It can be seen that the signal is absorption dominated. Right: the absporption corrected spectra for each reflection. The trace of a remaining energy dependent signal can be seen which is either explained by self-absorption or an intercalation correlated with the LHT-9 crystal structure. The solid red lines indicate a fit based on variation of the atomic position of selenium as well as its occupancy and the effective crystalline domain thickness. The dispersion corrections $f'_{\mathrm{Se}}, f''_{\mathrm{Se}}$ have again been obtained from the measured absorption and subsequent KK transform.

the reflection intensity with a contribution (sign and proportion) defined by the resonant atoms position. This contribution will also depend on the chosen reflection. However, only an average position of the foreign ion can be discussed this way and local distortions will not be visible. The latter can, in contrast, be studied based on the in the fine structure oscillations in the energy dependence (item (ii)). In order to do so, one needs to extract the fine structure function $\tilde{\chi}$ from DAFS oscillations which requires significantly lower noise in the data.

To obtain the position of selenium, DAFS has been measured on several reflections in symmetric transmission geometry using the same sample mount as before: after preparation of the sample substance, the powder was pressed into a pill and mounted on the rotary positioner with large aperture. The data was acquired at beamline E2 (RÖMO) of DORIS using a PSD and an additional photo-diode for simultaneous monitoring of the transmission through the sample. The energy dependence of transmission as well as integrated reflection intensity can be seen in Fig. 4.11 (left). In symmetric geometry, the absorption factor A equals the absorption suffered by the transmitted beam (000 reflection) [LLH06] multiplied with an energy independent factor. Therefore, the absorption is corrected for by normalization of the measured intensities on the transmitted one. The resulting spectra are shown in Fig. 4.11 on the right. Since μ is also related to transmission via Eq. (2.29), it was extracted and used via KK transform to obtain the fine structure of the dispersion corrections for selenium ($f'_{\mathrm{Se}}, f''_{\mathrm{Se}}$). This way, a coarse modeling of the corrected spectra could be performed by variation of the

positional coordinates of selenium within the unit cell and under the assumption that the fine structure of sample average and intercalated selenium do not differ much. This assumption is not completely justified, but sufficient here, since we do not aim for the analysis of the fine structure. Hence, the investigation of the structure of selenium-adsorbed LHT has to be restricted to point (i) mentioned above. The fitted theoretical spectra, containing the dependencies of DAFS, absorption and additional self-absorption (as introduced in Fig. 4.5), are shown as solid lines in Fig. 4.11 (right). Already by looking at the corrected data, an important observation can be made: a part of the spectral dependence can certainly be due to absorption, however, an increase of intensity in the pre-edge region can, without doubt, be attributed to a contribution from DAFS.

The interesting parameters for the fit were the coordinates (x, y, z) of the selenium position and its occupancy. Several solutions (minima) have been found during optimization, some representing crystal symmetry, others due to ambiguity in the measurement. This has been visualized in Fig. 4.12. There, the deviation of the χ^2 distribution in terms of σ is calculated according to [Avn76] and drawn for cuts of the parameter space exposig pairwise correlations of the parameters. Symmetrically non-equivalent local minima have been numbered and marked. At first glance, it is already obvious that there are some regions around $y = 0.25$ and $y = 0.75$ which can be excluded by this measurement. Interestingly these regions correspond well to the positions of titanate sheets showing that the method gives reasonable results. On the other hand, the resulting confidence regions are strongly shaped by the (limited) choice of reflection.

Higher order reflections result in a higher sensitivity to the atomic positions but also in an ambiguity since the phase factor for a Miller index of n repeats n times within the unit cell (see Eq. (2.39)). This can be seen, e. g., in the bottom left of Fig. 4.12. Since there was only one reflection with a z component ($l = 1$), the resolution along z is very low and the corresponding error margins are high, whereas in y-direction the resolution is high since one of the measured reflections had an Miller index of $k = 7$. Hence, there should be a 7-fold ambiguity in the y position of the solution but this is lifted by taking into account the 220 reflection – there is no common multiple of 1/2 and 1/7. However, for the x-direction, an ambiguity remained due to the choice of reflections for the measurement: only 220 has an h-component resulting in a two-fold ambiguity and, therefore, each solution (x, y, z) produces a "twin"-solution at $(x + 1/2, y, z)$ which is actually not true.

The other interesting parameter – the occupancy of the selenium site – was highly correlated with the crystallite thickness which is shown in the bottom left of Fig. 4.12. Therefore, the confidence interval of the occupancy is not well defined. Nevertheless, a minimum value of $o = 0.001$ can be given resulting in an average value of 0.016 selenium atoms per unit since

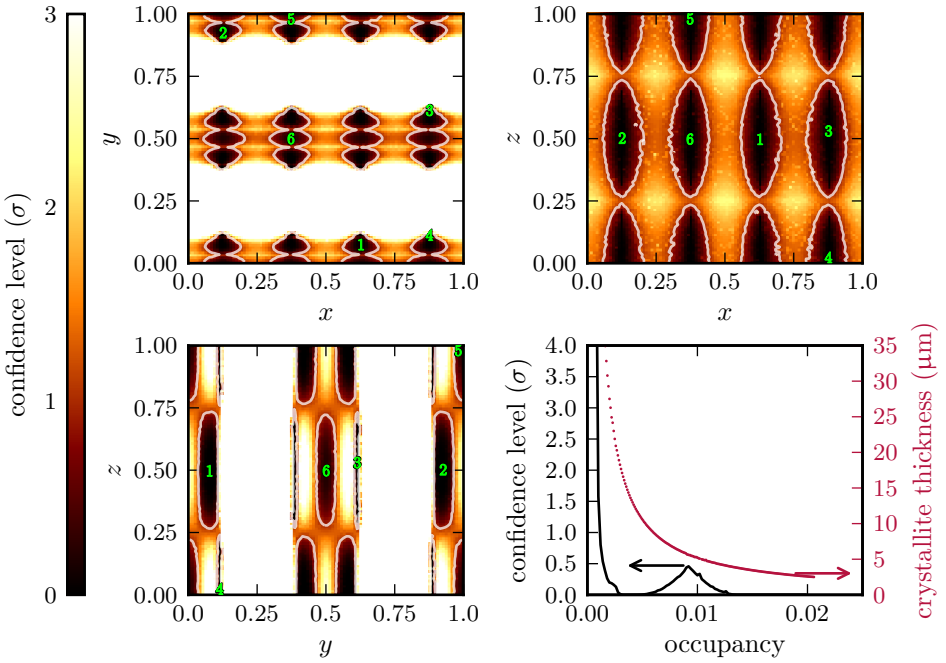

Fig. 4.12.: Confidence intervals for the interesting parameters that were varied during the fit shown in Fig. 4.11 (right). Pair-wise correlation is shown for the spatial coordinates of the selenium atom. The color corresponds to the best value of χ^2 in terms of deviation from the minimum in σ (approximating χ^2 as normal distributed) which was obtained for certain fixed parameters.

the general positions in LHT have a multiplicity of 16. Further, there is a reciprocal relation between the crystallite thickness and the occupancy in the fit-results. As the crystallite size of LHT bulk was estimated to be between $1 \ldots 10\,\mu m$, the corresponding occupancy would range from $0.05 \ldots 0.005$ meaning an abundance of $0.8 \ldots 0.08$ selenium atoms per unit cell. Certainly, the large uncertainty in these values as well as the ambiguity of atomic positions can be reduced by the measurement of additional reflections but we can already discuss the different types of solutions that are marked in Fig. 4.12. Table 4.1 lists these solutions together with the nearest special position and a set of nearest having a maximum distance of 2.5 Å.

We shall discuss all types of solutions briefly. It is important to note that there is a considerable error margin for each solution especially in the z-direction (seen in Fig. 4.12). Each pair of odd and even numbered solution (e. g. [1,2], [3,4]) form a twin solution due to the two-fold ambiguity in x-positions. Hence, only one of each is valid. For example, solution Se1 has been discarded in favor of Se2 since the interatomic distances appear more reasonable for the latter. The same way, solution Se3 has been discarded for its proximity to the titanate sheet. It should be stressed that a missing analysis of the fine structure functions results in a lack of knowledge about the local order. In particular, a solution that is very close to other crystallographic positions may still be valid since locally the crystallographic structure is perturbed and could differ from the average. Still, one of the twin solutions is artificial and therefore the less consistent ones have been neglected. Moreover, the solutions Se5 and Se6

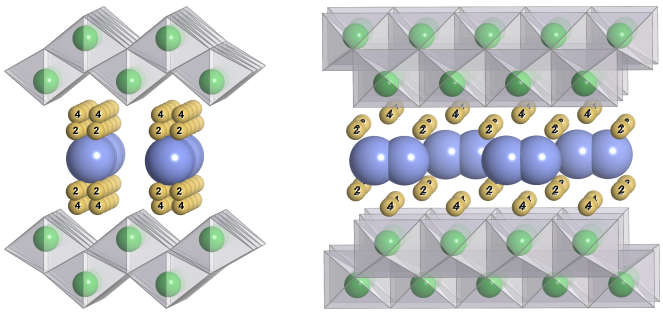

Fig. 4.13.: Display of the most probable positions (2,4) of the selenium atom between the titanate sheets as resulting from the fit. Left: Projection on a-b plane. Right: Projection on b-c plane.

have both been neglected after having a look at the low occupancies which would, through the correlation of parameters, only be possible under assumption of a large crystallite thickness of LHT powder higher than 20 µm (also for nearby solutions).

The selenium positions of the remaining solutions inside the LHT structure are shown in Fig. 4.13 along with their crystallographic equivalents. Remarkably, the solutions fall into plausible regions: solution Se4 corresponds to a free position of the interlayer gaps with a large distance to all neighbors whereas solution Se2 is close to the hydrazinium ion. Based on more detailed DAFS measurements, it would now be possible to characterize the local order of the perturbed structure around these selenium positions.

In conclusion, a structural refinement has been attained for a recently found substance, LHT, that shows high adsorption performance of heavy elements and is therefore interesting for environmental sustainability. Using resonant diffraction, a characterization beyond that of conventional methods was possible. In particular, x-ray spectroscopy has been performed exclusively on crystallographic atoms by means of DAFS. Spectral features that before were ascribed to surface regions or disordered regions have been found also in the purely crystalline part of the sample. For instance, pre-edge peaks that are, according to literature, related to 5-fold coordinated titanium environments are reproduced in energy dependent Bragg diffraction. Also the EXAFS information obtained in diffraction mode gives hints for short titanyl (Ti=O) bonds that are constituents of the 5-fold coordination geometry. Furthermore, the deposition of a foreign element inside the LHT structure has been investigated, as the process itself and the preferred position are not known yet. This was done by evaluating of the energy profiles of Bragg intensity near the edge of the intercalated atom, selenium. As a result, the possible positions of selenium have been determined based on a measurement of few reflections. The found positions show that selenium is strictly confined between the titanate sheets and is located near the original position of the hydrazinium ion.

Tab. 4.1.: positions of the selenium atom in LHT. All fall on the general $16o$ Wyckoff position. The nearest neighbors for each solution up to a distance of $2.5\,\text{Å}$ are presented. The coordinates written in light font indicate special (high-symmetry) Wyckoff positions which are very close to the actual solution.

Label (site)	x/a	y/a	z/c	Nearest Neighbors	Distance	χ^2 Increase	Occupancy	Valid
Se1	0.6253	0.0750	0.4977	O	1.2577	0	0.35%	✗
8n	0.6253	0.0750	0.5000	N	2.1383			
				N	2.1434			
Se2	0.1253	0.9250	0.5021	N	1.6671	0	0.35%	✓
8n	0.1253	0.9250	0.5000	N	1.6730			
				O	1.8373			
Se3	0.8757	0.6131	0.5304	O	1.5461	$0.0016\,\sigma$	1.4%	✗
8n	0.8757	0.6131	0.5000	Ti	1.5904			
				O	1.7118			
				O	2.4481			
Se4	0.8757	0.1130	0.0240	O	2.0456	$0.0016\,\sigma$	1.4%	✓
8n	0.8757	0.1130	0.0000	O	2.0622			
				Ti	2.0822			
				O	2.1630			
				N	2.2251			
				N	2.2687			
Se5	0.3724	0.0000	0.9994	N	1.5689	$0.1861\,\sigma$	0.22%	✗
4e	0.3724	0.0000	0.0000	N	1.5705			
				N	2.4762			
				N	2.4772			
Se6	0.3719	0.5000	0.4980	N	0.8348	$0.1861\,\sigma$	0.22%	✗
4e	0.3719	0.5000	0.5000	N	0.8444			
				N	2.3378			
				N	2.3492			

4.2. Singlecrystalline thin films – atomic and domain structure

In this chapter, the presented results will be both of methodological as well as applied kind. From now on, the samples under investigation will be single- (or 'mono-') crystalline. Therefore, the systems are more well defined and there are less unknowns. It also allows the study of anisotropic scattering in terms of polarization or wavevector dependencies. At first, results on atomic structure and domain propagation of singlecrystalline thin films will be presented. Thin films may provide the situation where absorption can be neglected: while the absorption-correction was one of the main challenges for the analysis of RXD data, it can be omitted in the case of Bragg diffraction in the thin film limit (see Eq. (2.44)). The study of thin films is in particular interesting since interface effects (strain, fields, surface defects) can change the structure of these films and generate new properties in them [Zha+15; Tan+13; Lic+14]. Moreover, functional materials are often used in the form of thin films to allow miniaturization (e. g. for ferroelectric random access memories (FRAMs)), combination of properties of different materials (e. g. giant magnetoresistance) or to reduce material costs when only surface properties are important. Here, thin films of two well known oxide dielectrics were studied, $BaTiO_3$ and $SrTiO_3$, which are closely related in their structure as well as their properties since barium and strontium are neighbors in the same chemical group.

4.2.1. Ferroelectric barium titanate films

Single-domain polarization state

For many years, ferroelectric materials have been in focus of scientific and technological investigations for their unique optoelectronic, photorefractive, piezoelectric and nonlinear optical properties which are based on their spontaneous electric polarization and the possibility of polarization reversal by an external electric field. BTO and other polar perovskites are well known model-ferroelectrics and remain subject of research and development due to their unique combination of ferroelectric, pyroelectric and optical properties. These features lead to versatile applications in electronic devices such as non-volatile memory cells (FRAMs) [SP89] or tunable capacitors, as well as in sensors, optical beam modulators [Tan+04], higher harmonic generators, etc.

Many envisioned applications rely on the ferroelectric properties of thin, single crystalline barium titanate films [Fei82]. While the behavior of bulk BTO is well known, an understanding of the physical properties of nano-scale effects is yet missing and stays in focus of research [SP89; Pol+12; JG03]. As was shown recently, ultra thin films allow tuning potential barriers

by external bias [Zen+13; TG13] and therefore the tunnel current in layered heterostructures or show photovoltaic effects [Zen+14]. Especially, at film thicknesses less than the typical diameter of the ferroelectric domain nucleus the nucleation-limited mechanism [TCF10] is reported to be replaced by homogeneous switching [Gay+11]. This effect can be of a critical importance both for understanding of the physics of ultra thin layers, but also for design and operation of devices.

In this part, the polarization state and dynamics of ultra thin BTO films was investigated using resonant diffraction. The thin singlecrystalline BTO layers were heteroepitaxially grown on platinum-coated magnesium oxide (MgO) substrates by *pulsed laser deposition* (PLD). The sensitivity of the RXD signal to the polarization state of a polar material was mentioned in the introduction and is well known and regularly used in materials science [Gor+16; Fab+15]. It is based on the breaking of Friedel's rule [Fri13] which occurs when taking into account complex-valued scattering amplitudes as done in RXD. This means that resonant diffraction can complement the existing methods for imaging of ferroelectric domains. Amongst these are, most prominently, scanning probe techniques such as *piezoresponse force microscopy* (PFM), *atomic force microscopy* (AFM) and *scanning electron microscopy* (SEM) as well as optical methods: optical microscopy or confocal Raman microscopy [YZ14]. The advantage of scanning probes is a very high spatial resolution down to a few nanometer whereas the optical methods are diffraction limited to about 250 nm. On the other hand, optical methods allow resolving the sample in depth and therefore provide 3D information. Next to resonant diffraction, it has been shown that coherent diffraction can be used to gain a high-resolution image of domain patterns by means of Bragg projection ptychography [Hru+13] yielding also high contrast and entailing all benefits of using an x-ray probe. The potential advantage of resonant diffraction is to gain time-resolved images of domains when it is combined with full-field x-ray diffraction microscopy [Hil+14]: A domain imaging with spatial resolution down to 100 nm together with a temporal resolution of (a single cycle) below 1 s would be unprecedented and belongs to the future outlook suggested in this thesis.

The polar unit cell of the tetragonal phase of BTO was shown before in Fig. 3.8. Fig. 4.14 shows the expected contrast in the 001 reflection calculated for different polarization states of BTO in an energy region near the titanium K and barium L edges. While the fine structure oscillations for all cases should be unchanged, the energy dependencies are shifted for different polarization states which is based on the fact that another reflection is measured (see Fig. 4.14 on the right). These changes are based solely on changing crystallographic weights and therefore on only sensitive on the average structure.

To conclude about the average (within the beam footprint) polarization state, an intensity measurement at a set of energies is necessary to overcome the normalization problem of

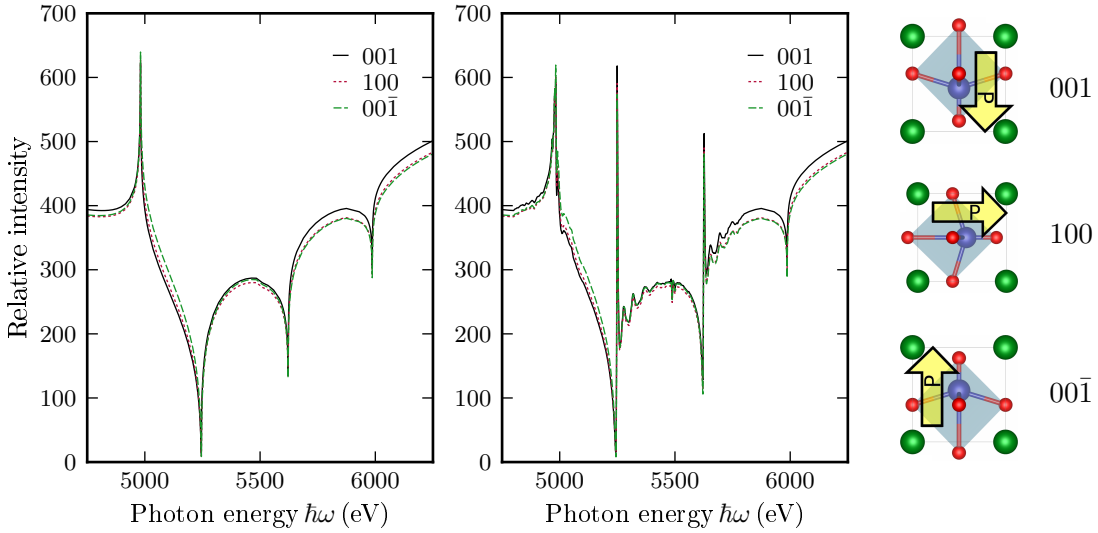

Fig. 4.14.: Calculations of expected RXD curves for different polarization states of the thin BTO layers for the 001 reflection and in the region of titanium K and barium L edges. The observed differences are in the range of 10 % and due to changing crystallographic weights and already visible in the calculation of the smooth parts (left). Taking into account fine structure oscillations (obtained by means of logarithmic dispersion relations, see Section 3.3.2) does not change the situation significantly (middle). The unit cells (right) illustrate the structures associated with these polarization states (up, in-plane, down) together with the resulting polarization.

unknown absolute values. For a small set, the result would usually be influenced by the energy dependent device function – a spectral drift due to different energy dependencies in the setup such as source spectrum, absorption in air and windows, detector efficiency, etc. Therefore, it is desirable to perform the diffraction measurements not necessarily in an energy range where the contrast is very large but rather where it shows a strong energy dependence. As seen in Fig. 4.14 such regions are precisely the absorption edges where the contrast may change its sign. In this case, the interesting signal changes faster than the device function. This can be optimized by a clever choice of Bragg reflections, if accessible, as is shown in the next section (4.2.2).

However, a remaining problem is that the calculated energy dependencies and consequently also the interpretation is based on structural models – the knowledge of the positions and atomic vibrations of all atoms as well as the occupancy of each crystallographic site. Especially for thin films, this knowledge is usually not given. A conventional crystal structure determination is not possible in the low-dimensional, restricted geometry system. The different technologies and parameters of epitaxial layer growth produce very different qualities in terms of crystallinity: defects such as vacancies, antisites or stacking faults render the simple structure model used in the calculation in Fig. 4.14 invalid. It is possible to include these defects in the model by considering a coherent mix of crystal structures and, hence, considering

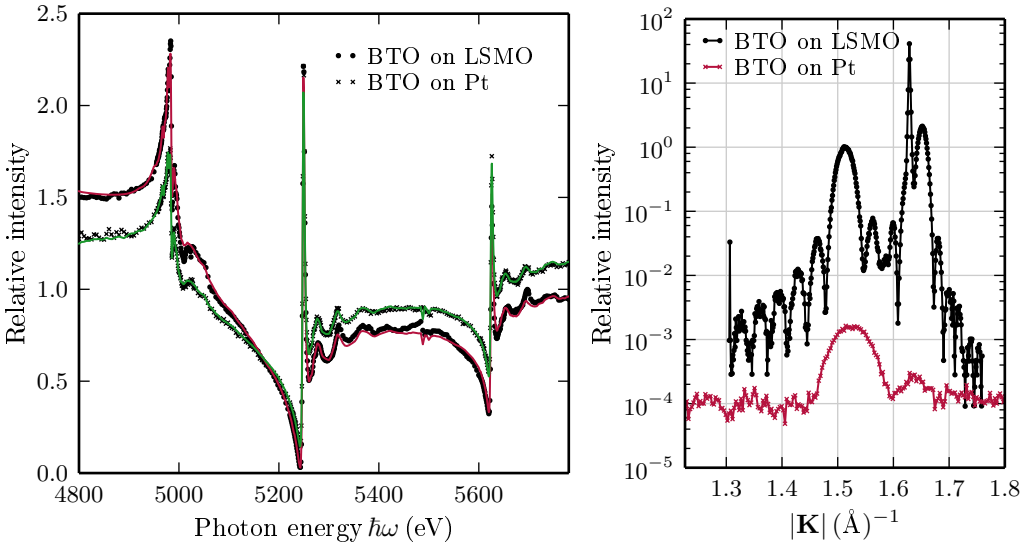

Fig. 4.15.: Energy dependence (left) and angular dependence (right) of the 001 reflection of BTO layers grown on different buffer layers. The energy dependence is solely sensitive to internal structural parameters as atomic positions, their uncertainty and occupancy while the diffraction pattern on the right mainly carries information about the lattice constant, layer thickness, roughness and orientation of the lattice. The result of fitting the energy dependence on the left is based on the extracted fine structure from other films (see Section 3.3.2) and shown as solid lines. From both curves a lower film quality for those grown on Pt interlayers can be concluded.

occupancy values lower than one and adding atoms to the unit cell which expands the set of unknown parameters.

The effect of film quality on the energy dependence of the 001 reflection of BTO can be seen in Fig. 4.15. The films were grown on different buffer layers (platinum and lanthanum strontium manganite (LSMO)) but also in different environments. The diffraction patterns on the right in Fig. 4.15 reveal that the thicknesses are different and very low for both films: $\approx 8\,\mathrm{nm}$ for the film grown on platinum and $\approx 18\,\mathrm{nm}$ for that on LSMO. It can also be seen that the film quality is different: besides the expected higher reflectivity of the BTO 001 reflection (at $\approx 1.5\,\mathrm{Å}^{-1}$) of the thicker film on LSMO (see Section 2.2), its thickness oscillations – maxima as well as minima – are much stronger pronounced. Fitting the energy dependence seen on the left in Fig. 4.15 results in very low (stable) values for the occupancies of the resonant atoms: $\approx 15\%$ for BTO on LSMO and $\approx 1\%$ for BTO on Pt. These values are obtained by limiting the occupancy to a maximum 1 while the film thicknesses have no effect on the energy dependence. Therefore, one should conclude that the structure model (single crystalline BTO) is not a good one here and that there is a large part of disorder in these films. For instance, stacking faults can result in a increase scattering power for oxygen or a very large statistical displacement of the cations having a similar effect as reduced occupancy. Without further investigation, e. g. of other reflections or other energy regions, no detailed explanation for the low values can be given. Important at this point is just to conclude that already the smooth energy

dependence of certain Bragg reflections can strongly vary when internal structural parameters change. Here, these variations are larger than those expected for an inversion of polarization (see Fig. 4.14): it seems that one cannot readily read the polarization state from the energy dependence. Nevertheless, when looking at the structure factor in Eq. (2.45), it becomes clear that parameters like thermal mean square displacement or reduced occupancy have a different effect (scaling of the atomic scattering amplitude) than a mean displacement (rotation of the atomic scattering amplitude in the complex plane). Therefore, it was possible to determine the polarization state for both samples as the fitting procedure steadily converged toward one of the boundaries when taking into account a (coherent) mix of two polarization states. As a result, the state of downwards pointing polarization (away from the surface, see Fig. 4.14) was concluded for both samples which is in accordance with local PFM measurements [Zen+14]. A polarization perpendicular to the surface is induced by biaxial compressive strain due to the lattice mismatch of BTO and platinum [Cho04; Zen+12].

Kinetics of domain growth in ultra thin BTO films

It was mentioned that the mechanism of polarization reversal is not well known for ultra thin epitaxial films. For bulk crystals and even thin layers, the polarization kinetics are dominated by the process of domain nucleation and subsequent domain wall motion [IT71]. In the case where the layer thickness is in the range of the size of typical domain nuclei, new models have been proposed to describe the switching [Viz+03; Hig+10] and have shown to yield a good description of measurements.

In this work, the kinetics of domain growth in ultra thin films was investigated using resonant x-ray diffraction. This method was used before to study the polarization state and switching of ferroelectric films [Ree+04; Wan+09]. The switching behavior of ultra thin, being matter of current research, was the original aim of this work. Ultra thin layers often do not allow to apply voltage through extensive electrodes which is due to defects such as conductive filaments which result in a drop of resistance. In this situation, application of a voltage will locally result in a high current density through this filament and cause local phase transitions due to heat. It was found, however, that small areas of the BTO films do not exhibit these defects. Patterns of circular electrodes with different diameters ($10, 5, 2, 1\,\mu m$) have been applied to the film and contacted through a conductive PFM tip (see Fig. 4.16). Some of the $5\,\mu m$ showed a resistance and could be used for switching the ferroelectric layer. The experiments have been carried out at the beamline ID01 at the European Synchrotron Radiation Facility (ESRF) where an *in-situ* AFM was available in combination with a sub- µm sized x-ray beam. In principle, the small beam and the AFM tip can both fit on the electrode of $5\,\mu m$ which, however, in our case did not turn out to be feasible. After landing the AFM tip on the electrode, we monitored

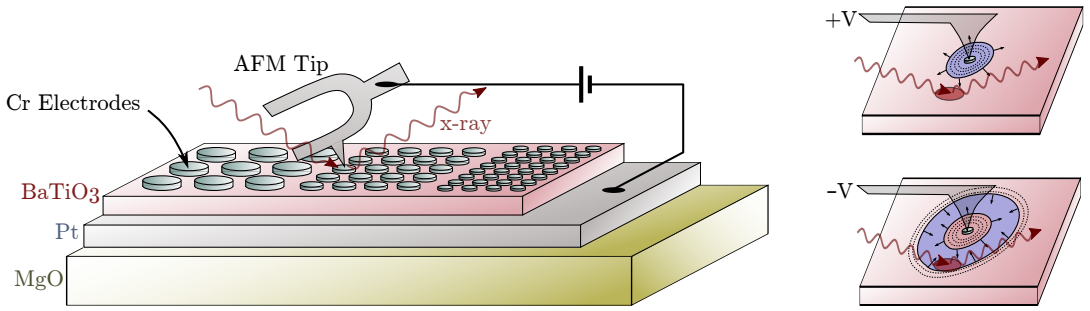

Fig. 4.16.: Sketch of the sample with patterned electrodes and the *in-situ* AFM (left) which was used at beamline ID01 for imaging of the electrodes as well as for voltage application. On the right the formation of different domain shapes as a result of alternating voltage is shown.

the Bragg intensity of the 001 reflection at an energy of 5000 eV where a relatively large contrast of $\approx 8\%$ for polarization reversal was expected. In parallel, a square wave-shaped, periodic, alternating voltage was applied between AFM tip and platinum buffer layer with different voltages in the range of $1 \ldots 4$ V which corresponds to a field of $33 \ldots 133$ MV/m for the present film thickness (30 nm). For thick bulk samples, much lower fields are needed for polarization switching and a reciprocal dependence of switching field to layer thickness has been found [Mer56; MS60]. Therefore, the activation voltages are comparable for thin layers and thick bulk crystals. The timescales we expected for a response of the polarization to the external bias of a few volts were in the microsecond to millisecond regime [Gru+05; Gay+13]. However, what was observed is a slow, reversible change of intensity in the course of several seconds. This intensity was accumulated over a large number of electric field cycles and the average is shown for different voltages in Fig. 4.17. Furthermore, it can be seen that there is a strong asymmetry in the speed of convergence of intensity with respect to the sign of the voltage. This difference also changes between the measurements for different absolute voltages. Both observations led to the conclusion that the actual process which was observed here is the lateral growth of polar domains. Firstly, it would explain the long time scales on which the inversion of polarization takes plase. Secondly, the asymmetric behavior can be understood since one polarization state is more stable depending on the initial (monodomain) state of the layer (see Fig. 4.16, right). A ring domain, for example, can dissipate into a circular monodomain after voltage withdrawal or domains can disappear due to backswitching to the original (global) state [Iev+14]. The initial state can be different since a constant voltage was applied for rather long time between the measurements. Therefore, for each case, there is a 'fast' and a 'slow' direction of switching. The overlap $\mathscr{O}$ of a circularly growing domain and a elliptic beam footprint with normally distributed intensity has been modeled numerically and, later, approximated with the function

$$\mathscr{O} = 1 - \left(\frac{t - t_0}{\tau} + 1 \right) \cdot \mathrm{e}^{-\frac{(t-t_0)}{\tau}}, \tag{4.3}$$

where $t > t_0$ is the time t_0 is the time of voltage reversal and τ is the characteristic switching time. The intensity is then obtained via $I(t) = I(0) + [I(\infty) - I(0)] \cdot \mathscr{O}(t)$ The switching times

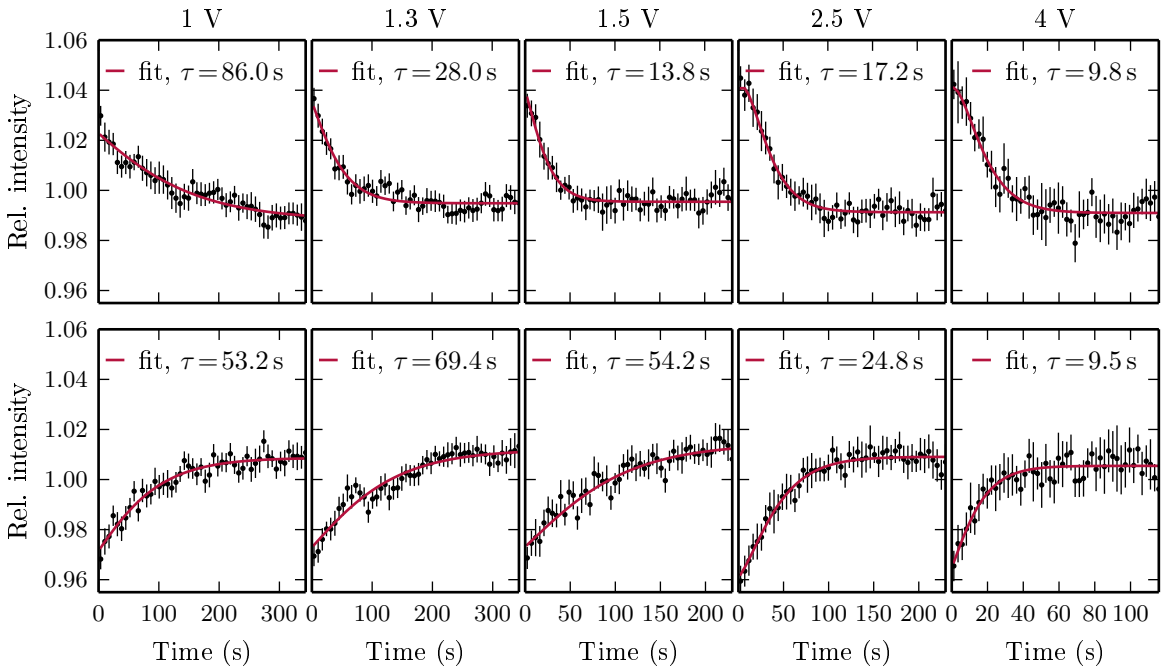

Fig. 4.17.: Results of averaging the intensities measured during a large number of alternating, square wave-shaped electric field cycles averaged for intervals of constant voltages. Top: positive voltage on the tip. Bottom: negative voltage on the tip. The amplitudes are given in the top of each column. The red solid lines indicate the obtained fit using Eq. (4.3).

are shown as a function of absolute applied voltage and classified as slow and fast component in Fig. 4.18. Since the beam size was $\approx 1.8\,\mu\text{m}$, a rough estimate for the speed of domain wall motion can be given as $v_{\text{dwm}} \approx {}^{1.8\,\mu\text{m}}/_{4\tau}$ (the overlap Eq. (4.3) grows beyond 90% after 4τ).

In conclusion, the absolute polarization state of ferroelectric (polar) films has been characterized exploiting the violation of Friedel's law in resonant x-ray diffraction and based on resonant measurements of solely one reflection. In contrast to the one presented here, most similar studies rely on the switching of polarization to obtain the Friedel contrast [Gor+16; Ree+04]. The dynamics of switching can be monitored at a fixed energy near the resonance. This has been used here to study the nucleation and growth of domains in ultra thin ferroelectrics. An asymmetry in the domain wall motion with respect to voltage reversal has been observed. Furthermore, the preferred direction of voltage changed between the measurements indicating a stabilization of a formed domain due to pinning effects which limit the domain wall propagation [KG07]. This results in the formation of additional domains as shown in Fig. 4.16 (right). Although the dependence of switching lifetime τ on voltage allows further interpretation that can yield thermodynamic parameters, the further analysis was beyond the scope of this work and needs further efforts that should be presented in future reports.

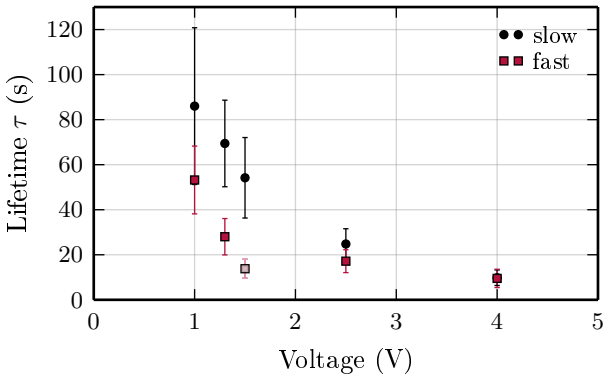

Fig. 4.18.: Characteristic decay times as obtained by fitting the averaged time series shown in Fig. 4.17 sorted for fast and slow direction of switching.

4.2.2. The structure of a new, polar phase of strontium titanate ($SrTiO_3$)

The second perovskite that was studied in this work, is strontium titanate $SrTiO_3$ (STO). Chemically it is very similar to the previous example, BTO. At high temperatures ($> 120\,°C$) BTO even exhibits the same crystal structure as STO at room temperature: an ideal perovskite ($CaTiO_3$-type) with cubic, centrosymmetric unit cell corresponding to space group $Pm\bar{3}m$ (see Fig. 4.19). Nevertheless, it is a popular material for heterostructure interlayers [RS08] or as a substrate and can acquire a variety of interesting physical properties based on breaking of the symmetry. Among these are: superconductivity [SHC64] and ferromagnetism near interfaces [Cen+09] or due to doping [Moe+12] as well as ferroelectricity due to strain [Hae+04] or isotope exchange [Ito+99].

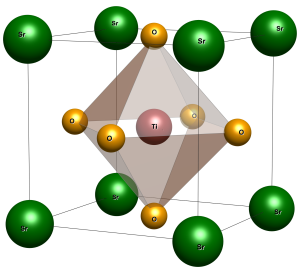

Fig. 4.19.: The unit cell of bulk $SrTiO_3$: cubic, centrosymmetric, ideal perovskite ($Pm\bar{3}m$).

In addition to that, single crystals of STO show a long term response to a static external electric field leading to a tetragonal distortion. This can be seen by broadening of Bragg peaks after application of an electric field on the order of 1 MV/m for several hours [Mey+04]. A breaking of centrosymmetry in the surface region could be concluded based on the appearance of additional Raman modes [FW68; Han+13].

This phase transition is quite unusual because it is triggered by a redistribution of oxygen vacancies in the crystal which is visible as an increased leakage current (see right in Fig. 4.20). The oxygen vacancy migration leads to local distortions of the unit cells and, eventually, to the formation of a polar, strained layer at the anode side which is stabilized by the external field. Therefore the new phase is referred to as *migration induced, field-stabilized, polar* (MFP) phase. It demonstrated several additional physical properties, such as pyroelectricity [Han+15] and piezoelectricity [Kha+15]. These observations led to the prediction of space group $P4mm$ for the new structure. However, no direct information about a polar atomic structure could be obtained because conventional x-ray diffraction methods could not be applied in the restricted geometry system. Since the MFP layer only exists on top of a cubic, singlecrystalline STO substrate, they are connected by a continuously strained transition region and the corresponding Bragg peaks from different volumes are strongly convoluted (see Fig. 4.20).

In this work, a new tool of x-ray structure analysis was developed which can be used to characterize slight changes in atomic positions and, hence, to determine the crystal structure even in such cases. It is based on the evaluation of energy dependencies of Bragg reflections

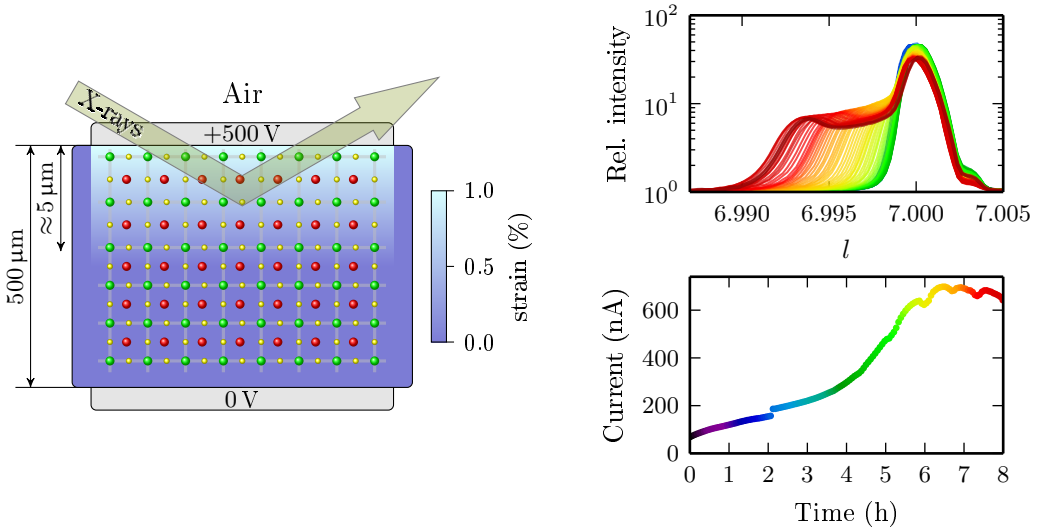

Fig. 4.20.: Schematic view of the formation process in a strontium titanate single crystal. The crystal is sandwiched between two electrodes (left). During application of an external electric field of $\approx 1\,\mathrm{MV/m}$ for several hours, the leakage current starts to grow exposing the migration of oxygen vacancies (right). After several hours (here: 5 h), the reflections in field direction (shown here: $hkl = 007$) experience a broadening towards lower momentum transfer (i. e. lower scattering angles). A thin layer of increased lattice constant appearing near the anode can be concluded.

near a resonance (absorption edge). In contrast to the previous section, the Bragg reflections are selected in a way that an accidental destructive interference can occur. It is common to observe 'systematic extinction' for certain reflections which is due to space group symmetry and the destructive interference of scattered waves coming from the same elements. However, here we make use of the situation where competing scattering contributions from different elements cancel each other out to a large extent. This can be controlled by tuning the scattering amplitudes through the variation of photon energy and, therefore, can only be observed in a small energy range. In particular, if two (or more) atoms contribute to the structure amplitude with opposite sign, the real part of the scattering amplitude of the heavier atom (stronger scatterer) can be reduced by approaching an absorption edge of this particular atom (see, e. g., Fig. 2.3). Thus, when scanning the photon energy through the edge, the structure amplitude runs through a loop in the complex plane which passes the origin (shown in Fig. 4.21) and leads to a pronounced minimum in intensity.

Whether and to which extent this can be achieved strongly depends on all structural parameters that influence the structure amplitude (2.45). Small changes in atomic positions, thermal vibrations or occupancies will shift the structure amplitude and also the conditions for a destructive interference. This is shown as an example for STO and the variation of either atomic position or mean square displacement (as in the Debye-Waller factor (2.46)) of titanium in Fig. 4.21. Regarding the distribution of atoms in the crystal lattice, the position always refers to the mean of all positions whereas the Debye-Waller factor takes account of the

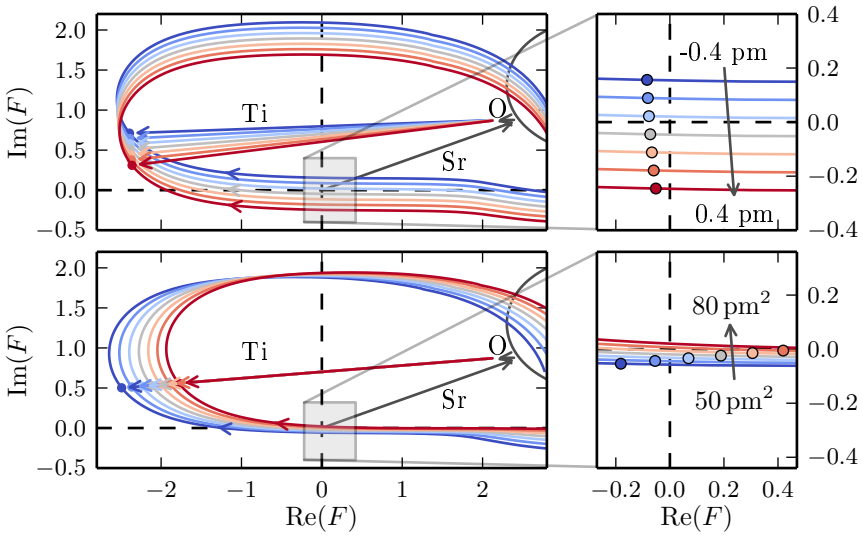

Fig. 4.21.: Complex plane and curves that are described by the structure amplitude for the example of STO: strontium undergoes a fine structure (black curve) and competes with the contributions of titanium and oxygen (small). The sum of contributions corresponds to the colorful (blue to red) lines. Top: changes in titanium position lead to rotation of its scattering amplitude. Bottom: variation of the mean square displacement results in scaling of the titanium contribution. Right: zoom into the origin of the complex plane, showing that the curves pass near zero resulting in an intensity minimum. Circles mark a position of fixed energy and values indicate the limits of variation.

mean square deviation or variance of this distribution. This means that each crystallographic site is usually parameterized by first and second moment of the statistical distribution of the corresponding atom. If necessary, higher moments can be taken into account [Kuh13].

It can be seen that a variation of these parameters has a different effect on the loop which is described by the structure factor: directed displacement rotates the scattering amplitude of the atom while an increasing mean square deviation results in scaling. This can be seen in Eq. (2.45) and is more clear when developing the phase factor near a position where destructive interference occurs. Let $\mathbf{u}$ be a small displacement of atom j ($\mathbf{r}_j = \mathbf{r}_j^0 + \mathbf{u}$) leading to the expansion

$$\begin{aligned} F &= \underbrace{F|_{\mathbf{u}=0}}_{\to 0} + \left.\frac{\partial F}{\partial u^k}\right|_{\mathbf{u}=0} \langle u^k \rangle + \frac{1}{2} \left.\frac{\partial^2 F}{\partial u^k \partial u^l}\right|_{\mathbf{u}=0} \langle u^k u^l \rangle + \cdots \\ &\approx o_j f_j \mathrm{e}^{-M_j} \mathrm{e}^{\mathrm{i}\mathbf{K}\mathbf{r}_j^0} \left(\mathrm{i} K_k \langle u^k \rangle - \frac{1}{2} K_k K_l \langle u^k u^l \rangle \right), \end{aligned}$$

where $\langle u^k u^l \rangle$ denotes a mean square displacement from the average which is added on top of the one contained in M_j. As a result, a change of the mean and the variance of a atomic position shift the complex structure amplitude in orthogonal directions because the former contribution is scaled with the imaginary unit. This will also affect the measured intensity (= distance from the origin) in different ways. On the right in Fig. 4.21, points mark a fixed energy position in the curve near the minimum intensity. For a directed displacement of the

considered atom, the position of the minimum will hardly change in terms of energy, but the relative intensity will change dramatically. On the other hand, increasing the mean square deviation will mostly influence the location of the minimum. Therefore, these parameters can be disentangled by one measurement of energy dependence of such Bragg reflection in the region of the minimum. It is worth noting that the described, strong qualitative changes of the energy dependence for slight variations in these parameters are very easily accessed experimentally and, this way, one has a very sensitive probe to small structural modifications. However, the interpretation of the observed changes strongly depends on the knowledge of all other structural parameters. In practice, a crystal structure never changes in just one internal parameter (such as displacement) – it is reasonable to expect a relaxation of the surrounding lattice. As there are several unknowns, an unambiguous refinement of the one, interesting parameter may turn out to be impossible or require measurements of additional reflections.

Characterization of the initial state of $SrTiO_3$

Using the described experimental access to atomic displacements, this part of the work aims to solve the structure for the strained MFP phase formed in STO. For a set of Bragg reflections where exactly one of the Miller indices (hkl) is odd, the structure amplitude of ideal STO (neglecting thermal motion) takes the form

$$F \approx f_{\mathrm{Sr}} - f_{\mathrm{O}} - f_{\mathrm{Ti}}.$$

These reflections show considerable intensity, since strontium is the heaviest atom of this structure and scatters stronger then the sum of the other two. Approaching energies near the strontium absorption edge, however, results in a decrease of its scattering amplitude which can lead to destructive interference. As mentioned before, a prediction of the spectral shape of the reflection intensity in such situation is strongly influenced by the Debye-Waller factors which are the only parameters that are not known precisely for STO single crystals.

To give an example, the energy dependence of the 007 reflection of STO is shown as a function of temperature on the left in Fig. 4.22. It exposes the high sensitivity to thermal motion: the minimum becomes more pronounced and shifts towards higher energies as the temperature decreases. The measurements have been carried out in quasisymmetric geometry (i.e. $\alpha = \beta$) at the beam lines BM20 [Mat+99] and BM28 [Bro+01] of the ESRF. The cooling was done using a continuous-flow liquid nitrogen cryostat at BM20 down to a temperature just above the cubic to tetragonal phase transition at 105 K [Tom92]. The single crystal samples with electrodes have been prepared in the Institute of Experimental Physics of the University Freiberg.

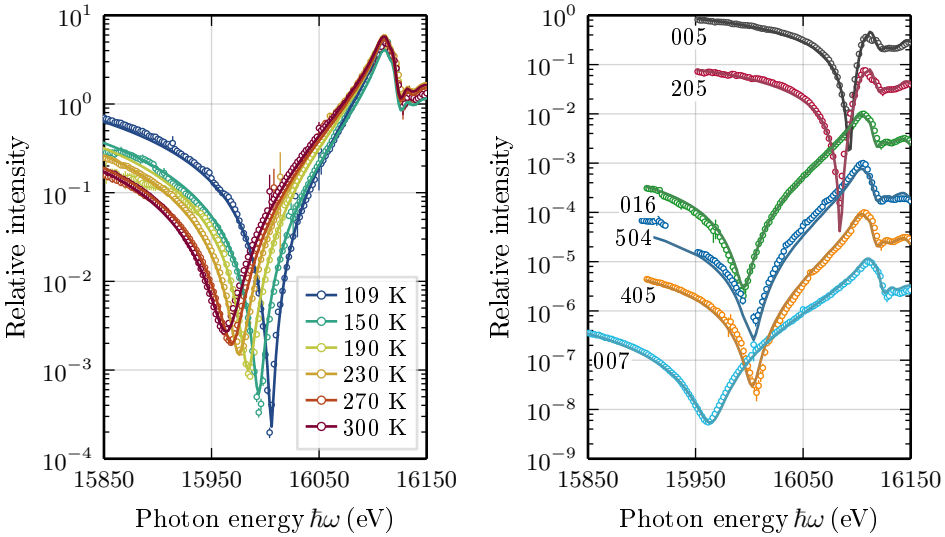

Fig. 4.22.: Left: energy dependence of the 007 reflection of bulk STO in the vicinity of the Sr-*K* edge and for different temperatures. Right: additional reflections measured in the same energy region at room temperature in quasisymmetric geometry. Open circles show measured data, solid lines show the best fit through variation of the Debye-Waller factors.

Calculations based on different references from literature [YHK02; Abr+95] for the cubic phase of STO already give different results for the location of the minimum and only one of the datasets shows a fair agreement with the measured data for room temperature (see Fig. A.2 of Appx. A). Therefore, but also to test the present method, a characterization of the initial state of the STO bulk single crystals was performed. For a proper modeling of the data measured in the near and post edge region, the fine structure oscillations need to be taken into account. These have been acquired from EXAFS measurements on polycrystalline STO (see Section 3.3.2 for details). Furthermore, absorption needs to be taken into account for Bragg geometry according to Eq. (2.44).

Assuming a temperature dependence of the atomic displacement parameters (ADPs) (see Eq. (2.47)) according to the Debye model [Kri96]

$$\langle u^2\rangle(T) = \frac{9\hbar^2 T^2}{m k_B \Theta^3} \int_0^{\Theta/T} \frac{x}{\mathrm{e}^x - 1}\,\mathrm{d}x, \tag{4.4}$$

a refinement of the Debye temperatures Θ_j for each atom j in the unit cell is possible based on the temperature dependent data of the 007 reflection. However, oxygen does not occupy a site of cubic symmetry in STO and, hence, is an anisotropic scatterer. A symmetry analysis (see Section 2.2.4) shows that there are two unique components in the tensor of ADPs corresponding to thermal vibrations parallel and perpendicular to the Ti–O bond, respectively. For this reason, a decomposition of the Debye temperature (into $\Theta_\mathrm{O}^{\parallel}$ and $\Theta_\mathrm{O}^{\perp}$, see e. g. [Pot+84; KGD02a]) and additional data was necessary to perform an unambiguous refinement.

Tab. 4.2.: Refined atomic displacement parameters (ADP) for cubic $SrTiO_3$ as a result of fitting the temperature dependent experimental RXD spectra to the Debye model. The given errors correspond to 1σ uncertainties.

	Debye temperature	ADP at 298 K
Atom	Θ (K)	U (Å^2)
Sr	198^{+31}_{-43}	$0.0127^{+0.0080}_{-0.0031}$
Ti	292^{+56}_{-73}	$0.0109^{+0.0084}_{-0.0032}$
$O_{\parallel}$	713^{+364}_{-270}	$0.0061^{+0.0085}_{-0.0030}$
$O_{\perp}$	499^{+92}_{-121}	$0.0117^{+0.0082}_{-0.0031}$

Measurements on further reflections at room temperature and in the same energy region are shown on the right in Fig. 4.22. The calculated curves as a result from fitting all components of the Debye temperature and a linear device function to the data are shown as solid lines in both plots of Fig. 4.22. All measured reflections are members of the mentioned set where exactly one Miller index is odd. However, not all reflections of this set are necessarily suitable or exhibit a large contrast with respect to variation of the unknown parameters. Moreover, whether the reflection shows a strong response or not, again depends on the structural parameters. That is why an iterative procedure would be necessary to find the ideal set of such reflections, consisting of

(a) identification of the reflection showing, in average, the strongest response under variation of all unknown parameters within the reasonable boundaries,

(b) measurement and fit of this reflection which may lead to an infinite number of solutions that are part of a lower-dimensional submanifold of the parameter space (this was the case here after only taking into account data from the 007 reflection),

(c) re-entry at (a) for all combinations of parameters from this subset or finish if only one solution is found.

If only one solution has been found, it still makes sense to acquire more data, as it would allow to reduce the error in the fit result. Since such iterative procedure is not ideal for experiments at beamlines (at large scale facilities), a set of interesting reflections larger than necessary was identified beforehand and all spectra were taken into account. The results of the fit are shown in Table 4.2. The obtained results are close to the literature values [JP99; Abr+95] and show the same trends: (i) titanium, despite being the lighter atom, exhibits smaller

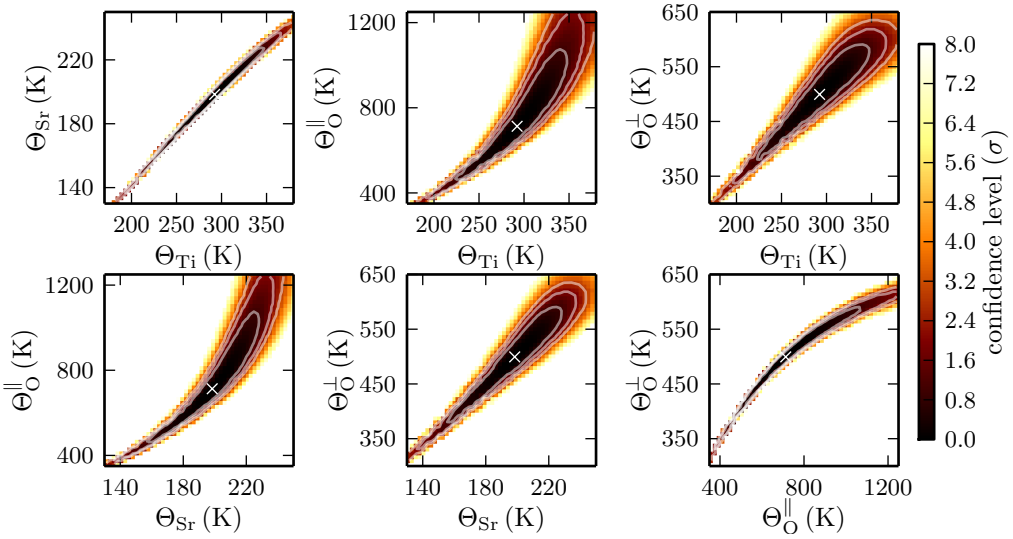

Fig. 4.23.: Maps of the sum of squares χ^2 for fixed values of pairs of the interesting parameters (the Debye temperatures) and the simultaneous optimization of all other parameters. A strong correlation is revealed, indicating that the relative values of the Debye temperatures are known more precisely. White crosses mark the minimum position of the cost function and contour lines show the confidence regions corresponding to 1σ, 2σ and 3σ.

thermal vibrations than strontium which is explained by the strong bond inside the $[TiO_6]$ octahedra; (ii) the oxygen vibrations along the Ti–O bond are smaller than perpendicular to it. Apart from that, the results still show a quite large error which is unexpected considering the high sensitivity of the used approach. An explanation for this is the remaining correlation of parameters which is shown as a mapping of the response of the sum of squares χ^2 towards pairwise variations of the interesting parameters in Fig. 4.23. The other parameters (e. g. linear device function) have been optimized to gain the lowest value of χ^2 for each point in the maps according to [Avn76]. They expose a very strong correlation of the ADPs corresponding to a proportional variation causing the large errors. The relative errors, on the other hand, should be small: assuming the knowledge of one of these parameters, a very precise value for the others can be given. Thus, the ratios of the parameters are known very precisely from this fit. The strong correlation is based on the fact that both vibration components of ($U_O^{\parallel}$ and $U_O^{\perp}$) are contributing to every reflection and the mixing only slightly differs between the reflections. Certainly, measuring spectra of additional reflections or at different temperatures would help to decrease the correlation further. On the other hand, the obtained results proved to be sufficient to study the atomic displacements that occur upon application of the electric field with high detail.

Polar atomic displacements in the MFP phase

It has been mentioned before that the strained MFP surface layer shows polar properties which is why a displacement of the titanium atom away from the center of the [TiO_6] octahedron is expected. A secondary peak which develops towards lower scattering angles (see Fig. 4.20) has been ascribed to a $\approx 1\,\mu m$ thick region of constant strain at the anode side of the STO single crystals. The strain can reach values of up to 1% depending on the voltage, thickness and environmental conditions. Furthermore, there is a transition region with a strain gradient connecting the MFP layer with the bulk crystal that has a thickness of a few microns. Therefore, there is a variety of manifestations of the MFP phase, all likely to exhibit different atomic displacements.

If the MFP layer is homogeneous in the in-plane directions XAFS is an applicable tool to investigate the local atomic structure: for x-rays under grazing incidence, the penetration depth is small and only the MFP layer can be probed. In particular, XANES at the titanium K edge has been used before to study the electronic structure of related, ferroelectric perovskites (e. g. $BaTiO_3$, $PbTiO_3$). It has been shown that the intensity of the mixed dipole-quadrupole transition from Ti $1s$ to Ti $3d$ e_g states depends quadratically on the off-center displacement of the Ti ion [Ved+98; Woi+07]. Figure A.3 in Appx. A shows XANES measurements of the Ti-K pre-edge performed under gracing incidence and during forming of the MFP phase. The observed changes are tiny: the characteristic peak A slightly grows and some additional density occurs between the peaks B and $C1$. The peak B, corresponding to the e_g states, should increase upon displacement of the central atom but, instead, a slight decrease is visible here. Due to the minor effects that were observed, a rigorous modeling of the XANES patterns was not pursued. On the other hand, this fact suggests that an adequate modeling of resonant diffraction curves from the MFP phase is possible based on the fine structure obtained before on polycrystalline STO.

A crystallographic determination of all atomic positions was intended based on the developed method of targeted suppression of reflections using resonant dispersion. One advantage of this method is that it allows to select volumes of constant strain through the Bragg condition and does not average of all atoms that are in the x-ray beam path, like XANES. Furthermore, XANES is dependent on lattice parameters, while the resonant suppression is solely sensitive to the structure factor which, in turn, does only depend on relative atomic positions of the unit cell. In other words, the angular and the energy dependence of Bragg reflections allows a study of lattice and basis in a distinct manner. The former was characterized before [Han+13; Kha+15] and resulted in a Poisson's ratio of approximately $\nu = -\frac{\Delta a}{\Delta c} = 0.2$ for the tetragonal model.

From the crystallographic point of view, atomic displacement results in reduction of symmetry in a kind that depends on its direction. A displacement of atoms perpendicular to the field direction would result (i) in an orthorhombic structure leading to crystal twinning and consequently to peak splitting or (ii) in a two-fold superlattice in a-b direction [Gla75] resulting in appearance of superlattice reflections. To exclude both cases, reciprocal space maps have been recorded using a position sensitive detector showing no additional reflections. Furthermore, it is reasonable to assume that the ADPs will not (at least not significantly) change during formation of the MFP phase. This way, only the atomic positions in field-direction (along z) are unknown. There are three oxygen atoms which were linked by symmetry in the initial, cubic state. After application of an electric field, these split up into two oxygen atoms having the Ti–O bond perpendicular to the field direction and one where it is parallel to the field. This leaves four atoms with unknown z position reducing to three as the origin of the unit cells can be chosen arbitrarily and is defined as the position of strontium here.

As mentioned before, differently strained regions in the layer are expected to result in different atomic displacements. As a prototype for this study, we selected a value of strain of $^{\Delta c}/_{c} = 0.15\%$ which corresponded to the position of the distinct maximum after the forming process (see Fig. 4.20) under the present conditions. This has been done by recording l-scans for each included reflection hkl choosing an offset according to $^{\Delta l}/_{l} = -0.15\%$. At these positions, fixed **K** energy scans have been performed for a similar energy range as before and a similar set of reflections (see Fig. 4.24 (left)). During the measurements, the x-ray beam had to be

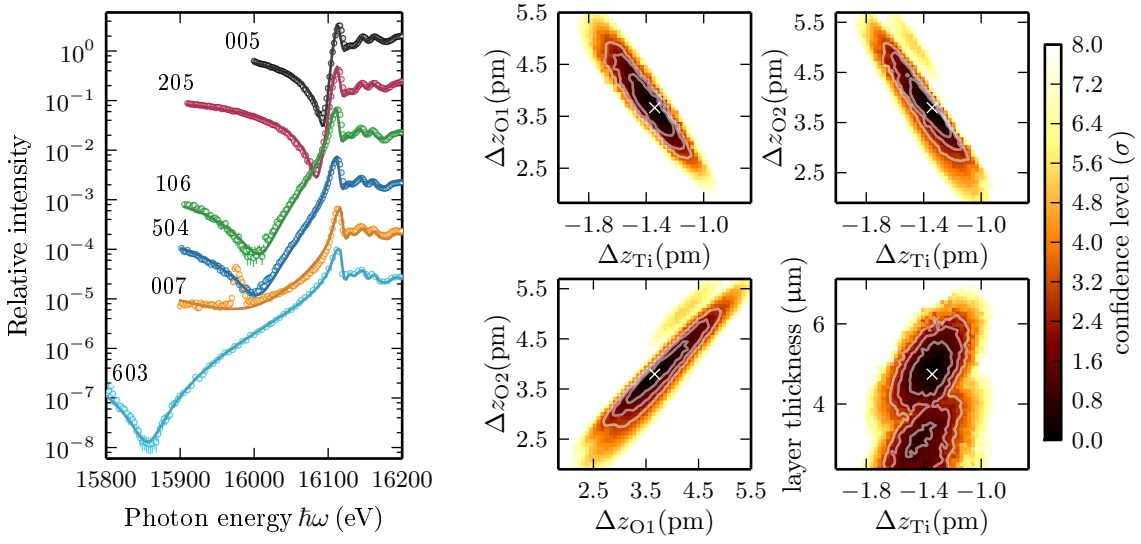

Fig. 4.24.: Left: Energy dependence of different reflections from the MFP phase near the Sr-K edge: measurement (open circles) and fit (solid lines) after optimization of the atomic positions in field direction (z). Right: maps of pairwise correlations of the interesting parameters showing the stability of the fit. The false color reflects the lowest sum of squares obtained for each position through optimization of all other parameters. Values are given in multiples of the standard deviation σ. Contours mark 1σ, 2σ and 3σ.

attenuated to keep the photocurrent low ($< 1\,\mu A$) maintaining the electric field and, thus,

facilitating the forming process. Figure 4.24 shows that some of the reflections, especially the 007, have a very different energy dependence than for the initial state (Fig. 4.22) giving a hint of atomic displacement already. The maximum in the pre-edge region of the 007 reflection is an artifact and can be attributed to multiple beam diffraction (Renninger effect [Ren37]). This can be filtered out in most cases by recording several spectra for small rotations around the **K** vector and subsequently processing their median or picking one which was not affected. For the analysis of these measurements, it is now necessary to take into account the finite thickness of the diffracting MFP layer, since the penetration depth of the x-rays was in the range of $5 \ldots 43\,\mu\mathrm{m}$ depending on reflection and energy. This can readily be done based on Eq. (2.44) and setting $\alpha = \beta$ for the present geometry.

The best fit obtained for each reflection is shown as solid lines in Fig. 4.24 (left) and the corresponding results are presented in Table 4.3. The errors are again the 1σ confidence intervals

Tab. 4.3.: Refined internal structure parameters for the MFP phase with $^{\Delta c}/_{c} = 0.15\%$

Atom	Wyckoff site	x/a	y/a	z/c	Δz (pm)
Sr	$1a$	0	0	0	–
Ti	$1b$	1/2	1/2	0.4966(3)	-1.34(16)
O1	$1b$	1/2	1/2	0.0096(11)	3.67(59)
O2	$2c$	1/2	0	0.5099(11)	3.80(63)

which are marked in the pairwise correlation maps of all parameters on the right in Fig. 4.24. They have been determined based on iterating the ADPs through all combinations within the 1σ confidence regions shown in Fig. 4.23 and repeating the fit to perform a proper error propagation. Again, the relative values of displacement are better known than the absolute values. Nevertheless, the uncertainties in the atomic positions are in the sub-picometer regime and therefore very low.

The determined structure of the MFP phase is indeed polar and corresponds to that of the well known ferroelectrics $BaTiO_3$ and $PbTiO_3$. This is remarkable, since, in contrast to these, $SrTiO_3$ does not show a ferroelectric phase when cooling to low temperatures: a paraelectric to ferroelectric phase transition sets in at 40 K but remains incomplete down to 0 K [Li+06]. Still, the MFP phase is not a proper ferroelectric material because a polarization reversal is not possible: as soon as the field is removed (or reversed), the strain field collapses and the structure relaxes to the cubic, centrosymmetric state within seconds.

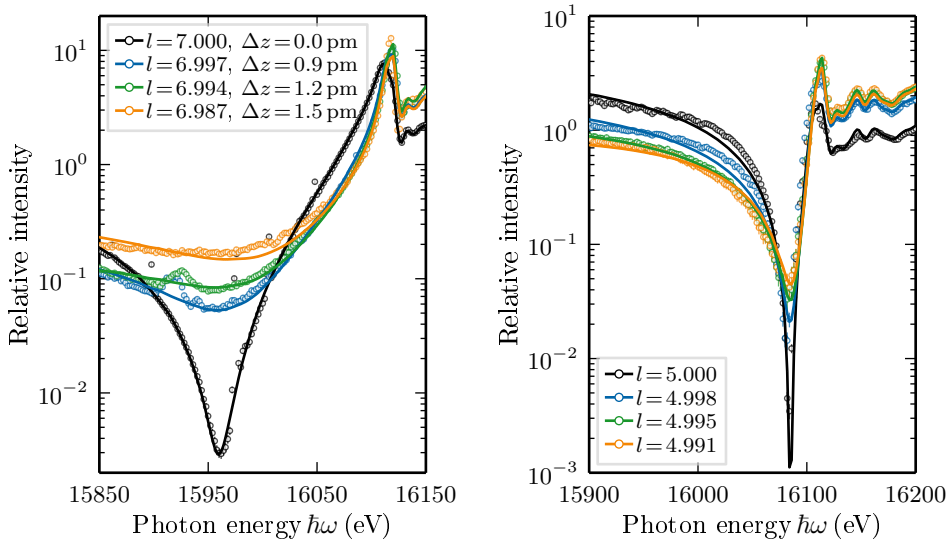

Fig. 4.25.: RXD spectra of the 007 (left) and 205 (right) reflections of differently strained volumes in the $SrTiO_3$ crystal after formation of the MFP phase. Strain has been selected by measuring the energy dependence of different positions of the rocking curves as marked in Fig. 4.26 and indicated by the actual value of the Miller-Index, l. The solid lines represent the best fit with the resulting z-displacement of titanium given in the legend.

Relation of strain and displacement

A remaining question is how the displacement develops throughout the transition region between MFP and bulk STO where the strain is continuously decreasing and finally going to zero. To answer it, several positions in the diffraction pattern can be selected for fixed **K** energy scans including the bulk peak to check for possible displacement also in the bulk (see Fig. 4.26). For these positions, the energy dependence of two reflections – 007 and 205 – has been measured. The results are shown in Fig. 4.25 together with the calculated curves. A refinement of all positions based on two reflections is less stable. Therefore, the atomic displacements have been coupled corresponding to the results obtained above, for a strain of 0.15%. Assuming then a proportional movement of the atoms, only one structural parameter needs to be determined. The resulting unit cells are drawn (with enhanced displacements) for each measured position on the top left in Fig. 4.26 whereas the corresponding values of z-displacement of titanium with respect to strain are presented on the right. One can see already a significant displacement for the smallest strain that could be selected. Therefore, all of the strained volume is polar. Also the strain overproportionally grows with increasing displacement. A closer look suggests a cubic dependence $x_{33} = {}^{\Delta c}/_{c} \propto (\Delta z)^3$. A hypothetic explanation is based on two assumptions:

i) In the case of electrostriction, which is a property of all insulators, the strain depends quadratically on the polarization P_i that, again, is proportional to the displacement.

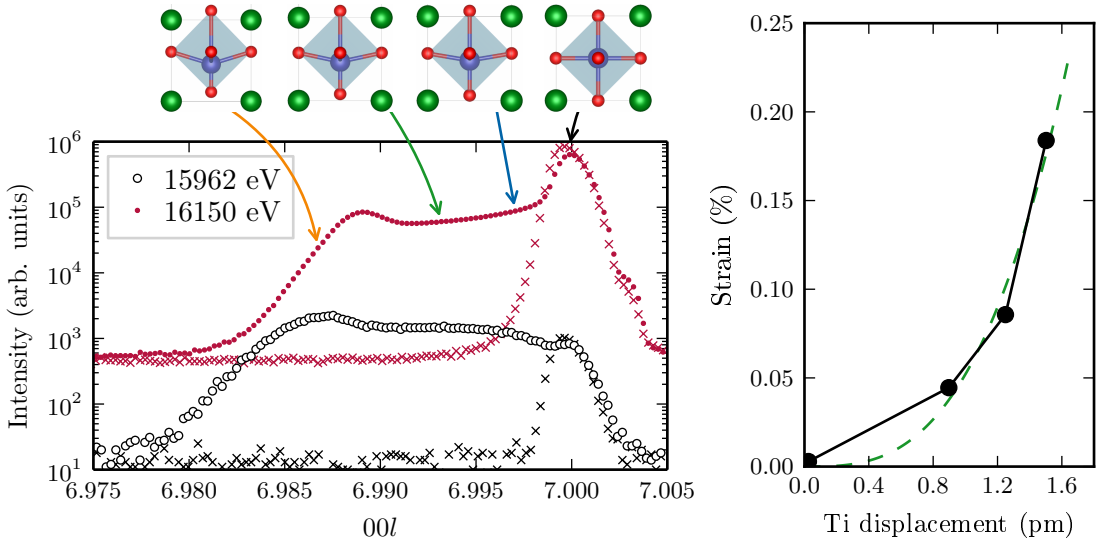

Fig. 4.26.: Left: l (or K_z) scans of the 007 reflection before (crosses) and after (circles) the forming process of the MFP phase and for two different energies. The secondary maximum that is ascribed to the MFP phase develops at lower l. Remarkably, the peak ratios are very different at the two energies which can only be explained by different atomic positions for the both cases. Arrows mark the positions where fixed **K** energy scans have been recorded for the 007 as well as for the 205 reflection. The unit cells on top show the results of fitting these scans by enhancing the displacements by a factor of 10 for better visibility. Right: The corresponding strain dependence of displacement (black dots) which reflects a cubic relation (green broken line).

This gives in field direction $x_{33} = q_{3333}P_3P_3$ where q_{ijkl} is the tensor of electrostrictive coefficients.

ii) The elastic interaction with bulk STO allows larger strain with higher distance from the bulk which correlates with higher displacement.

Both dependencies would multiply to the observed cubic behavior. However, it is necessary to test these assumptions which motivates future investigations.

Resonant suppression of Bragg reflections as a potential tool for structure determination

The presented method analyzes the changes in energy dependence of Bragg intensity that is defined by an amplitude difference of partial waves scattered by different atoms. As structure modifications change the weighting in this difference, qualitative changes, such as a shift of the minimum, can be observed. Here this allowed a structure refinement with high detail.

The energy dependence of Bragg reflections has been used to extract structural information before. In all cases substantial limitations exist in comparison to the present development.

To avoid ambiguities in the refinement, fixed structural models were presupposed or only one structural parameter was assumed to be unknown [MP00; Kol+10]. Often, the analysis required inverting ("switching") the structure [Ree+04; Azi+10] in order to measure the Friedel pair contrast. Furthermore, in all cases the impact of Debye-Waller factors was neglected and the obtained resolution was much lower than here, where destructive interference is exploited for the first time.

In principle, the employed resonant suppression of Bragg reflections can universally be combined with all diffraction based x-ray techniques. Since it relies on rather weak reflections, limitations are found where the intensity is generally not abundant. However, it may be the only tool to get high-resolution crystallographic positions especially in a restricted geometry where only few reflections can be accessed or their absolute intensities cannot be compared. Furthermore, the method represents a uniquely sensitive probe for structural dynamics *in-situ*, such as switching ferroelectric films or polarization changes in pyro- and piezoelectrics. Practical advantages are that the measurements can be performed in the pre-edge region allowing straightforward, model-independent calculations and that the kinematic approximation of diffraction, neglecting extinction effects, is valid as the reflections are weak.

The question remains whether the method can be applied in many cases or if STO is a specially suitable structure. So which prerequisites does it entail and how likely is it to find suitable reflections? The Ewald-sphere containing available reflections grows with higher photon energies, larger unit cells and lower symmetry. Likewise grows the probability to find a suitable reflection. On the other hand, high energies require heavy atoms to allow resonant measurements and large unit cells lead to a large number of independent atoms which could render a full refinement of all parameters exceedingly difficult.

Still, a large set of structures fulfills these conditions and are candidates for the application of the method. Among this set, each material needs to be assessed individually using a brute force calculation of all reflections in a certain range of momentum transfer. Here, the figure of merit is the relative change of intensity $\Delta I/I$ with respect to the variation of an interesting parameter. To estimate the proportion of substances that would allow a similar study, a large random set of structures has been evaluated which was taken from the *Crystallography Open Database* (COD) [Gra+11] and fulfills the following characteristics:

- a unit cell smaller than $2000\,\text{Å}^3$,
- a limited number of four different elements,
- at least one element heavier than potassium.

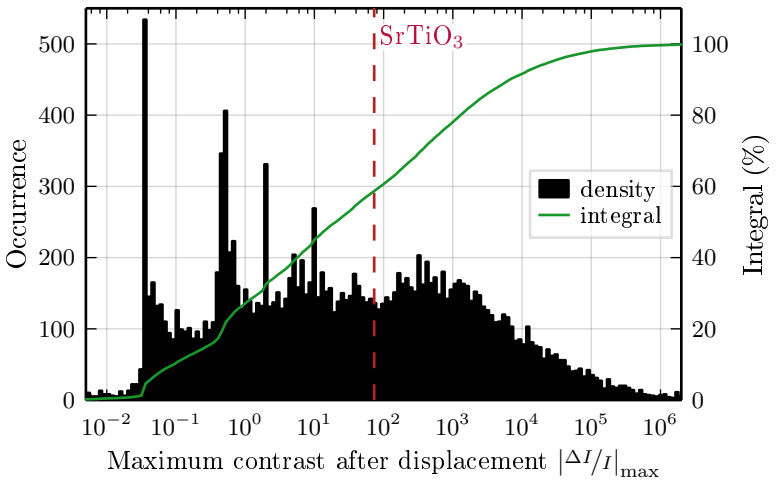

Fig. 4.27.: Histogram of maximum observed relative intensity changes due to mean square displacement calculated for a large set of 16,118 structures randomly selected from the COD. The dashed line marks the present case of $SrTiO_3$.

For this set, RXD spectra in the $5 \ldots 100\,\mathrm{keV}$ range of all reflections having a momentum transfer lower than $|\mathbf{K}| \leq 18\,\text{Å}^{-1}$ and showing reasonable intensity have been calculated before and after imposing an isotropic mean square displacement of $U_{\mathrm{iso}} = 0.0001\,\text{Å}^2$ onto the heaviest atom. The resulting distribution of contrast in comparison to the present case of STO is shown in Fig. 4.27. The obtained values extend over a wide range showing that the method cannot routinely be applied to all selected structures. On the other hand, $SrTiO_3$ is only an average representative in terms of contrast. Almost half of the processed samples have reflections that show a larger response to the dynamic displacement. In conclusion, the method is a promising way to answer remaining questions in x-ray structure analysis.

4.3. Single crystals – forbidden reflections and point defects

The last example of application of resonant diffraction makes use of the anisotropy – the wavevector and polarization dependence – of scattering which can be observed in the near edge region and may result in additional reflections. For these "forbidden" reflections, the non-resonant structure amplitude equals zero. They are purely resonant and can appear only in crystals of non-symmorphic space groups, where glide planes or screw axes cause extinctions that are removed due to different anisotropies of the atomic scattering amplitude at energies close to an absorption edge. The anisotropy has been introduced in the theory part (see Section 2.1.3) and was developed into a series of tensors with increasing rank that allow to impose crystallographic symmetry. It can be shown that structural defects and the accompanying atomic displacements can add a degree of anisotropy by an additional dependence on wavevector and, this way, raise the tensor rank of intrinsic scattering. For example, it may lead to a dipole-dipole contribution to the third rank (dipole-quadrupole) tensor. This can be caused by: i) dynamic displacement (thermal motion, phonons) [Ovc+10; KGD02b] or ii) static displacement caused by point defects [DO02; DO00]. Since lower orders of wavevector dependence (e. g. zero order: dipole-dipole scattering) are usually stronger, they can result in a very strong, additional contribution to forbidden reflections that are only allowed for higher orders. Hence, this represents another very sensitive access to atomic displacement in crystals much different in kind than the one presented in previous chapters. In particular, the analysis of reduced scattering tensor symmetry very strongly depends on the local structure and gives a distinct response to the spectra of Bragg intensity whereas the former method is purely crystallographic meaning that it only carries average information. This also means that in this approach, where the tensor rank is increased, it is possible to study the response of the surrounding lattice to the displacement. On the other hand, forbidden reflections are much weaker than those which are allowed for scalar scattering. Therefore, they can only be measured on single crystals.

4.3.1. Additional anisotropies – expansion of displacement dependence

To expose the sensitivity to displacement, we need to recall expansion of the (nonlinear) wavevector dependence of the scattering amplitude. It is followed by an expansion of the (again nonlinear) dependence of the phase factor on the momentum transfer $\mathbf{K}$ for small displacement. Since, wavevectors and the vector of momentum transfer are related ($\mathbf{K} = \mathbf{k} - \mathbf{k}'$), the tensors describing the corresponding dependencies are linked. Here, this concept is outlined for the special case of a dipole-dipole (rank 2) contribution which is raised to contribute to a rank 3 reflection.

Combining Eq. (2.14) and Eq. (2.21), gives another form of the tensor series resulting from the expansion of the wavevector dependence (2.20). The form factor of atom j can then be written as

$$f_j^{\alpha\beta}(\mathbf{k},\mathbf{k}',\hbar\omega) = f_{0,j}\delta^{\alpha\beta} + D_j^{\alpha\beta} + \mathrm{i}\left(k_\gamma I_j^{\alpha\beta\gamma} - k'_\gamma I_j^{*\beta\alpha\gamma}\right) + k_\gamma k'_\delta Q_j^{\alpha\beta\gamma\delta} + \ldots, \tag{4.5}$$

where the indices α and β correspond to the components of the two polarization vectors. Let us consider now the small displacement $\mathbf{u}_j$ from the ideal position as it was introduced in Section 2.2.3: $(\mathbf{r}_j \rightarrow \mathbf{r}_j^0 + \mathbf{u}_j)$. The product of atomic scattering amplitude and phase factor contributing to the structure amplitude (see Eq. (2.45)) then takes the form

$$f_j^{\alpha\beta}\,\mathrm{e}^{\mathrm{i}\mathbf{K}\mathbf{r}_j} = f_j^{\alpha\beta}(\mathbf{u}_j)\,\mathrm{e}^{\mathrm{i}\mathbf{K}\mathbf{u}_j}\,\mathrm{e}^{\mathrm{i}\mathbf{K}\mathbf{r}_j^0}. \tag{4.6}$$

The important difference between this equation and the derivation of the Debye-Waller factors in Section 2.2.3 is that the scattering amplitude is considered to change upon small displacement $\mathbf{u}_j$. This is important if the local structure of the resonant atom changes due to the displacement and therefore has an impact on the near-edge fine structure. If there is a collective movement, as in the case of acoustic phonons, this dependence can be neglected. We will see in the following that it becomes especially important if it results in an increase of tensor rank and therefore can be the only contribution leading to the observation of certain Bragg reflections.

For a small displacement, the exponential function can be developed into a taylor series:

$$\mathrm{e}^{\mathrm{i}\mathbf{K}\mathbf{u}_j} \approx 1 + \mathrm{i}\mathbf{K}\mathbf{u}_j - \frac{1}{2}(\mathbf{K}\mathbf{u}_j)^2 + \ldots. \tag{4.7}$$

This way, each order of $\mathbf{K} = \mathbf{k} - \mathbf{k}'$ adds a rank to each of the tensors of the series in Eq. (4.5) and thereby results in different behavior under change of basis and, hence, different symmetry. Furthermore, the dependence of the scattering amplitude on the small displacement can be developed into powers of u_j [DO00]:

$$f_j^{\alpha\beta}(\mathbf{u}_j) = f_j^{\alpha\beta}(0) + f_{jl}^{1,\alpha\beta}u_j^l + f_{jlm}^{2,\alpha\beta}u_j^l u_j^m + \ldots, \tag{4.8}$$

where the symmetry and the rank are not changed since there is no dependence on an external vector, e. g. $\mathbf{K}$. The product in Eq. (4.6) will now contain a large sum of terms proportional to different powers of $\mathbf{K}$, defining the symmetry under change of basis, and powers of $\mathbf{u}_j$ which determine the behavior under averaging over all unit cells. From Eq. (2.45) follows

$$F^{\alpha\beta} = \sum_j \langle f_j^{\alpha\beta}(u_j)\,\mathrm{e}^{\mathrm{i}\mathbf{K}\mathbf{u}_j}\rangle\,\mathrm{e}^{\mathrm{i}\mathbf{K}\mathbf{r}_j},$$

where $\langle\ \rangle$ denotes the average over all unit cells.

For clarity, let us now consider a specific example where the rank of the dipole-dipole tensor $D_j^{\alpha\beta}$ is increased by one due to the linear $\mathbf{K}$ dependence in Eq. (4.7), neglecting higher orders.

This is an interesting case since there are forbidden reflections that can be observed only when taking into account third rank scattering tensors or higher. In this case, the second rank dipole-dipole contribution can still contribute due to displacement. As the dipole-dipole term is much stronger, this contribution can even dominate the Bragg intensity. For this case, we get

$$D_j^{\alpha\beta} \to \mathrm{i}\langle D_j^{\alpha\beta}(\mathbf{u}_j)\mathbf{K}\mathbf{u}_j\rangle = \mathrm{i}\left[D_j^{\alpha\beta}(0)K_\gamma\langle u_j^\gamma\rangle + D_{jl}^{1,\alpha\beta}K_\gamma\langle u_j^\gamma u_j^l\rangle + D_{jlm}^{2,\alpha\beta}K_\gamma\langle u_j^\gamma u_j^l u_j^m\rangle + \dots\right]. \tag{4.9}$$

Some terms of this sum vanish for averaging over all unit cells depending on the local symmetry of displacement with respect to $\mathbf{K}$. If the displacement is caused by thermal vibrations, it is normal-distributed and (as shown in Section 2.2.3) only the term quadratic in $\mathbf{u}_j$, thus having a linear dependence in $D(\mathbf{u}_j)$, remains after averaging. This is the so-called *thermal motion induced* (TMI) contribution of atom j forbidden reflections:

$$D_{j,\mathrm{TMI}}^{\alpha\beta} = \mathrm{i}D_{jl}^{1,\alpha\beta}K_\gamma\langle u_j^\gamma u_j^l\rangle \simeq \mathrm{i}\frac{\partial D_j^{\alpha\beta}}{\partial u_j^l}K_\gamma\langle u_j^\gamma u_j^l\rangle =: \mathrm{i}D_{j,\mathrm{TMI}}^{\alpha\beta\gamma}K_\gamma. \tag{4.10}$$

If the displacement is due to defects, its symmetry corresponds to the site symmetry of the resonant atom and has to be assessed for each specific case. It is, in general, also not normal-distributed and, due to the relaxation of the surrounding structure, a nonlinearity of the scattering amplitude with respect to displacement can be expected. Therefore, the whole sum in Eq. (4.9) is collected for u_j^γ and attributed to the *point defect induced* (PDI) contribution

$$D_{j,\mathrm{PDI}}^{\alpha\beta} = \mathrm{i}\langle D_j^{\alpha\beta}(\mathbf{u}_j)u_j^\gamma\rangle K_\gamma =: \mathrm{i}D_{j,\mathrm{PDI}}^{\alpha\beta\gamma}K_\gamma. \tag{4.11}$$

Computing Eq. (4.11) is difficult and relies on the knowledge of the relaxed local structure around the defect which can be obtained, e. g., via *density functional theory* (DFT). In practice, PDI contribution can be separated from the TMI by reducing the temperature.

Since $D_{j,\mathrm{TMI}}^{\alpha\beta\gamma}$ and $D_{j,\mathrm{PDI}}^{\alpha\beta\gamma}$ transform as third rank tensors, they mix with $I_j^{\alpha\beta\gamma}$. Like the dipole-dipole tensor $D^{\alpha\beta}$, they are symmetric with respect to permutation of the first two indices (α,β) in the case of non-magnetic materials. To point out the interference with $I_j^{\alpha\beta\gamma}$, it is developed into symmetric $(+)$ and antisymmetric $(-)$ part:

$$I_j^{\alpha\beta\gamma} = \underbrace{\frac{1}{2}(I_j^{\alpha\beta\gamma} + I_j^{*\beta\alpha\gamma})}_{I_{j+}^{\alpha\beta\gamma}} + \underbrace{\frac{1}{2}(I_j^{\alpha\beta\gamma} - I_j^{*\beta\alpha\gamma})}_{I_{j-}^{\alpha\beta\gamma}}.$$

Now, including TMI and PDI terms, Eq. (4.5) (up to third rank) takes the form

$$f_j^{\alpha\beta}(\mathbf{k},\mathbf{k}',\hbar\omega) = f_{0,j}\delta^{\alpha\beta} + D_j^{\alpha\beta} + \mathrm{i}\left[K_\gamma\left(I_{j+}^{\alpha\beta\gamma} + D_{j,\mathrm{PDI}}^{\alpha\beta\gamma} + D_{j,\mathrm{TMI}}^{\alpha\beta\gamma}\right) + K_\gamma^+ I_{j-}^{\alpha\beta\gamma}\right]\dots, \tag{4.12}$$

where $\mathbf{K}^+ = \mathbf{k} + \mathbf{k}'$ was defined. It can be seen that the TMI and PDI terms only contribute to the symmetric part of the third rank tensor. This represents a unique access to study

atomic displacement due to thermal motion and point defects. They can cause an additional contribution to third rank forbidden reflections that, in general, exhibits a different energy dependence than the intrinsic part ($I_{j+}^{\alpha\beta\gamma}$). Together with the temperature dependence of the TMI contribution, this allows a separate analysis of the different origins of forbidden reflection spectra. In the same way, the increase of rank of higher order contributions ($I, Q, \dots$) can be derived. Also, increasing the rank by more than 1, based on higher orders in the expansion of the phase factor 4.7 is possible. However, the presented contribution of the dipole-dipole scattering process to third rank forbidden reflections corresponds to the lowest order and therefore is usually the strongest that can be accessed experimentally. Apart from that, there are nonresonant forbidden reflections based on anisotropic charge density (or displacement) [CM66]. This can also be derived from Eqs. (4.5,4.7) based on the scalar term of the scattering amplitude and quadratic or higher terms of the $\mathbf{K}$ vector dependence. However, in the nonresonant case, there is negligible energy dependence and therefore no spectroscopic information about the nature of the anisotropy (static/dynamic displacement, electron density, etc.) can be obtained.

4.3.2. Hydrogen jumps in RbH_2PO_4

This technique has been used to study hydrogen jumps in the room temperature (paraelectric) phase of rubidium dihydrogen phosphate RbH_2PO_4 (RDP). RDP is closely related to KH_2PO_4 (KDP) as they are chemically very similar and they have isomorphous crystal structures both in the paraelectric as well as in the ferroelectric (low-temperature) phase [KN80]. KDP crystals are better studied since they are more known and popular in laser technology for their electro-optical properties and second harmonic generation. However, there are still open questions in regard to the mechanisms of hydrogen bonds [Las+05] and the para- to ferroelectric phase transition which are present in both structures. A unique structural feature in the paraelectric phase of KDP and RDP crystals are the hydrogen atoms which half-occupy two minima of a double well potential between two oxygen atoms [AlK+78]. Crystallographically, this is expressed by a Wyckoff site with 2 very close points and an occupancy of 1/2. This is shown in Fig. 4.28 (left). Between the two minima, hydrogen jumps are possible by tunneling or thermal excitation [Nel88], where the tunneling frequency in RDP is lower due to larger separation of the minima [Pee74]. This indetermination of the hydrogen atom position is lifted during transition to the ferroelectric phase at (146 K) (see right in Fig. 4.28). Even above the phase transition temperature, it is expected that instantaneous local configurations already show lower symmetry caused by a rotation of the [PO_4] tetrahedra [MHM04]. Although the time- and volume average is symmetric, these defects should be accessible by x-ray scattering since the hydrogen jumps take place on much longer timescale ($\approx 10^{-12}$ s, [SI96]) than that of x-ray interactions ($\approx 10^{-15}$ s) [Muk+10a; Aki+14].

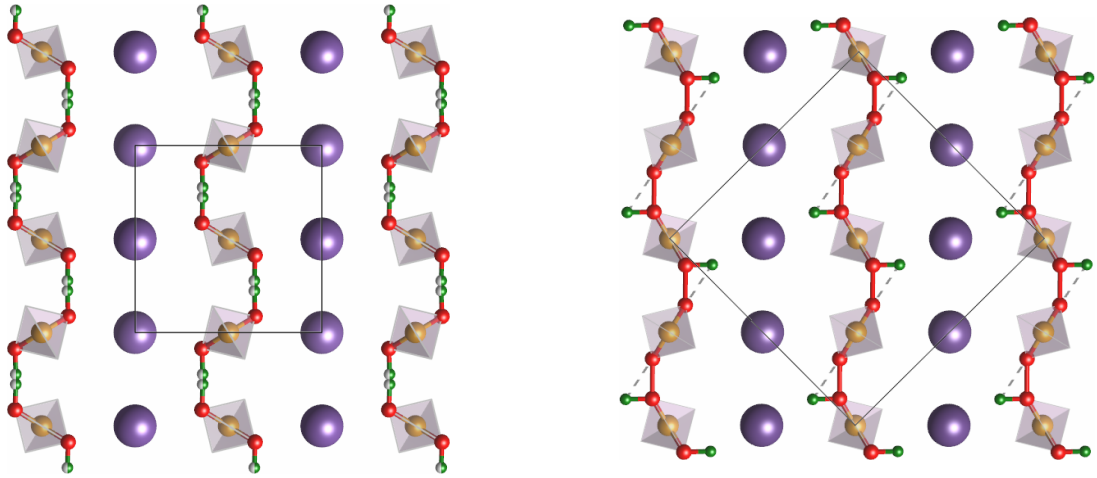

Fig. 4.28.: Projection of the structure of a cut of the RbH_2PO_4 on the a-b plane for $0 < z < 0.25\,c$ to highlight hydrogen bonded chains of [PO_4] tetrahedra. Left: tetragonal, paraelectric phase ($T > 146\,\mathrm{K}$) with space group ($I\bar{4}2d$). Right: orthogonal, ferroelectric phase ($T < 146\,\mathrm{K}$), space group ($Fdd2$). Atoms from small to large: H, O, P, Rb. Unit cells are drawn in solid, gray lines. In the paraelectric phase, hydrogen is statistically delocalized on two points of the same Wyckoff site resulting in half occupancy of each of them. During the para- to ferroelectric phase transition, this symmetry is broken and the unit cell is doubled in volume. Data taken from [MHM04].

There are several possibilities for the local geometry of the defects and most probable models have been pointed out [Las+05]. Based on a determined position of hydrogen in one of the equivalent minima of the double well potential, several scenarios of configurations for the neighboring hydrogen atoms exist, some of which are shown in Fig. 4.29. Statistically, two hydrogen atoms are attributed to each [PO_4] tetrahedron. Hence, there are 6 configurations to distribute the hydrogen around the tetrahedron which was first formulated by Slater [Sla41]. Two of these configurations correspond to the "polar" situation where the [PO_4] tetrahedra are connected with the hydrogen atom on the same side with respect to the c axis resulting in a net polarization with a local structure related to the low-temperature, ferroelectric phase. The other 4 ("Slater"-) configurations result in a polarization which is parallel to the a-b plane. A more complex model was proposed by Takagi [Tak48] where the possibility of asymmetric distribution of hydrogen is taken into account, such that pairs of tetrahedra are defined having one and three hydrogen atoms attached. These have been shown to exhibit a higher formation energy and, therefore, are less probable and not taken into account here.

The reduced symmetry for polar and Slater configurations is a good example on how defects can be investigated using resonant forbidden Bragg reflections. For the paraelectric phase, the set $\mathcal{R} = \{hhl \mid 2h + l = 4n + 2\}$ describes forbidden reflections where the two rubidium atoms that are linked by the diagonal glide plane contribute with opposite sign [Muk+10b] resulting in a set of extinctions. Due to the site $\bar{4}$ site symmetry, $D^{\alpha\beta}_{\mathrm{Rb}}$ has 2 whereas $I^{\alpha\beta\gamma}_{\mathrm{Rb}}$ has 4 independent components (see Appx. A.2). For this reason, the extinctions rules for $\mathcal{R}$ can

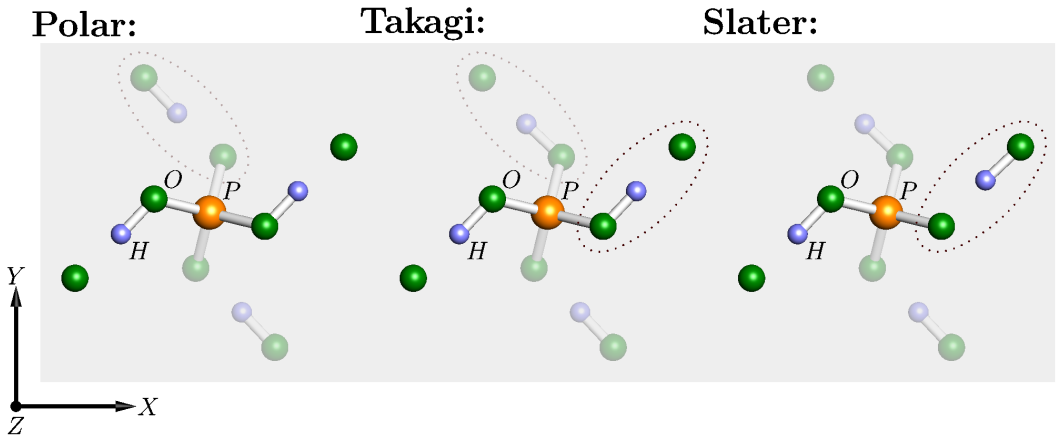

Fig. 4.29.: Defects that are usually considered in KDP and related, hydrogen bonded crystals. The semitransparent gray plane indicates the z-position of phosphorus. Dashed ellipses highlight changes with respect to the neighboring defect. Polar and Slater defect follow the "ice-rule" which states that hydrogen in evenly distributed on each of the [PO_4] tetrahedra whereas Takagi defects involve larger configurations of two adjacent tetrahedra and uneven distribution of hydrogen. The polar configurations exhibit a net moment in the c direction while for Slater configurations the in-plane symmetry is broken.

only be broken when taking into account linear wavevector dependence and therefore third rank tensor contributions – in particular, the components I^{xxz}_{Rb}, I^{xzx}_{Rb} and I^{zxx}_{Rb}. In terms of symmetric and antisymmetric parts with respect to permutation of the first two indices, the structure amplitude of this set becomes

$$F^{\alpha\beta}_{\{hkl\in\mathcal{R}\}} = 8\mathrm{i}\begin{pmatrix} I^{xxz}_{\mathrm{Rb}+}K_z & 0 & I^{xzx}_{\mathrm{Rb}+}K_x + I^{xzx}_{\mathrm{Rb}-}K^+_x \\ 0 & I^{xxz}_{\mathrm{Rb}+}K_z & -I^{xzx}_{\mathrm{Rb}+}K_y - I^{xzx}_{\mathrm{Rb}-}K^+_y \\ I^{xzx}_{\mathrm{Rb}+}K_x - I^{xzx}_{\mathrm{Rb}-}K^+_x & -I^{xzx}_{\mathrm{Rb}+}K_y + I^{xzx}_{\mathrm{Rb}-}K^+_y & 0 \end{pmatrix}, \tag{4.13}$$

omitting the Debye-Waller factor for now. This representation corresponds to crystal lattice units and has been obtained using the phenomenological code pyasf [Ric16a], while the notation in the software is different from the one used here. The local symmetry of the rubidium site is reduced in polar or Slater defects such that also dipole-dipole (second rank) components may contribute to the structure amplitude of the reflections in $\mathcal{R}$. The same is true for the ferroelectric phase at low temperatures which relates to domains of polar defects and therefore the structure amplitude will contain dipole-dipole components. But since the average symmetry of randomly distributed defects in the paraelectric phase stays unchanged, the average dipole-dipole tensor is not affected. However, from the correlation between the defect and the displacement of the resonant atom, it follows an additional contribution to the symmetric dipole-quadrupole tensor due to the $\mathbf{K}$ vector dependence in the phase factor as it was outlined before (see Eq. (4.12) and [Muk+10a]).

Measurement of forbidden reflection spectra

The experimental efforts to study the different contributions to forbidden reflections of the set $\mathcal{R}$ have been focused on the 006 and the 550 Bragg reflections with respect to the tetragonal lattice. This choice allows a separate study of both polar and Slater defects since they depend on different tensor components. In particular, we consider incoming polarization that is polarized perpendicular to the plane of scattering (σ) since this is the norm at synchrotron beamlines. The outgoing polarization can then be both parallel (π) and σ polarized (see Fig. 2.2 for illustration). For a fixed reflection, the structure amplitude depends on the rotation around the $\mathbf{K}$ vector which is denoted by the angle ψ and defines the orientation of the crystal with respect to polarization and wavevectors. This way, we obtain for the 006 reflection

$$\begin{aligned} F_{006}^{\sigma\sigma} &= -\,8\mathrm{i}|\mathbf{k}| I_{\mathrm{Rb}+}^{xxz} \sin(\theta_{\mathrm{B}}) \cos(2\psi) \\ F_{006}^{\sigma\pi} &= \quad 8\mathrm{i}|\mathbf{k}| \sin(2\psi) \left(I_{\mathrm{Rb}+}^{xxz} \sin^2(\theta_{\mathrm{B}}) - I_{\mathrm{Rb}-}^{zxx} \cos(\theta_{\mathrm{B}})^2 \right). \end{aligned} \tag{4.14}$$

where θ_{B} is the angle between wavevector and lattice planes and $\psi = 0$ corresponds to the case where the lattice vector [100] is directed perpendicular to the scattering plane. Similarly we get for the 550 reflection

$$\begin{aligned} F_{550}^{\sigma\sigma} &= -\,4\mathrm{i}|\mathbf{k}| I_{\mathrm{Rb}+}^{zxx} \sin(\theta_{\mathrm{B}}) \sin(2\psi) \\ F_{550}^{\sigma\pi} &= \quad 4\mathrm{i}|\mathbf{k}| (I_{\mathrm{Rb}-}^{zxx} \cos^2(\theta_{\mathrm{B}}) \cos^2(\psi) - I_{\mathrm{Rb}+}^{zxx} \sin^2(\theta_{\mathrm{B}}) \cos(2\psi)). \end{aligned} \tag{4.15}$$

To verify the calculations of azimuthal dependence of the Bragg intensity, measurements have been performed at a fixed energy near the rubidium K-edge (see Fig. 4.30). It should be reiterated that the symmetric components can carry additional TMI and PDI contributions which involve a displacement of the resonant atom (rubidium) in the direction denoted by the third index of the tensor (see Eqs. (4.10, 4.11, 4.12)). Therefore, the 006 reflection can be utilized to study defects and thermal motion resulting in a displacement in the z direction whereas the 550 reflection is sensitive to displacement in the x direction.

The study involves a characterization of the temperature dependence of the reflections. The temperature dependence of the contributions to the forbidden reflections caused by intrinsic dipole-dipole or dipole-quadrupole transitions is conventional, meaning that their intensity decreases with temperature in accordance with the Debye-Waller factor. On the other hand, the TMI part grows with temperature and therefore shows an an anomalous temperature dependence. Also the PDI part can be expected to depend on temperature as the hydrogen configurations manifest themselves in form of a phase transition at low temperatures. Fig. 4.31 shows the measured intensity spectra of both 006 and 550 reflections as a function of temperature near the maximum of the azimuthal dependence in Fig. 4.30.

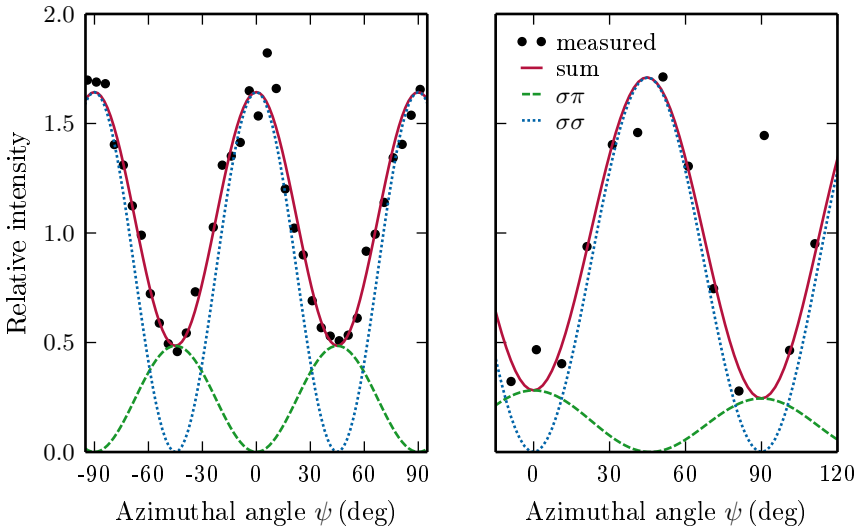

Fig. 4.30.: Measured azimuthal dependencies of the 006 (left) and 550 (right) forbidden reflections from the paraelectric phase at room temperature and a photon energy of 15196 eV (black dots). The curves calculated according to Eqs. (4.14,4.15) for σ and π polarized scattered beams are shown as broken lines. The $\psi = 0$ azimuthal position refers to the situation where the scattering plane is parallel to the (100) lattice planes for the 006 reflection or rather to the (001) lattice planes for the 550 reflection. The measurement is described by the incoherent sum of both polarizations (solid red line).

The measurements were carried out at the resonant scattering undulator beamline P09 at PETRA III (Deutsches Elektronen-Synchrotron (DESY)) [Str+13] using the six-circle diffractometer, a Si-111 double crystal monochromator and a pair of mirrors for focusing and higher harmonic rejection. Two RDP single crystals were grown in the Institute of Crystallography (Russian Academy of Sciences) and cut along (001) and (110) planes to provide access to the interesting reflections. The crystals were mounted into the closed-cycle helium cryostat that was installed at the diffractometer. Temperature dependence of the lattice parameters as well as the thermal expansion of the setup were characterized beforehand to correct the positions of the Bragg reflections and the sample automatically. The incident photon beam was σ-polarized to the (vertical) scattering plane.

There were two main difficulties complicating the experiment. Given the high photon energy which was needed to perform resonant diffraction at the rubidium edge and the weak forbidden reflections, the measurements were often dominated by multiple reflections (Renninger effect). The amount of multiple reflections grows with volume of the unit cell and the surface of the Ewald sphere ($\propto (\hbar\omega)^2$). As a result, it was practically impossible to find an azimuthal position to perform energy dependent diffraction free from Renninger effect. Therefore, several positions in a small range of azimuthal angle have been used to filter out this effect. In contrast to forbidden reflections, it is highly sensitive to the azimuthal position. The second problem was the fast degradation of the crystals under the powerful synchrotron beam. Figure 4.32 (left) shows the time dependence of the 550 reflection intensity at two temperatures. One can

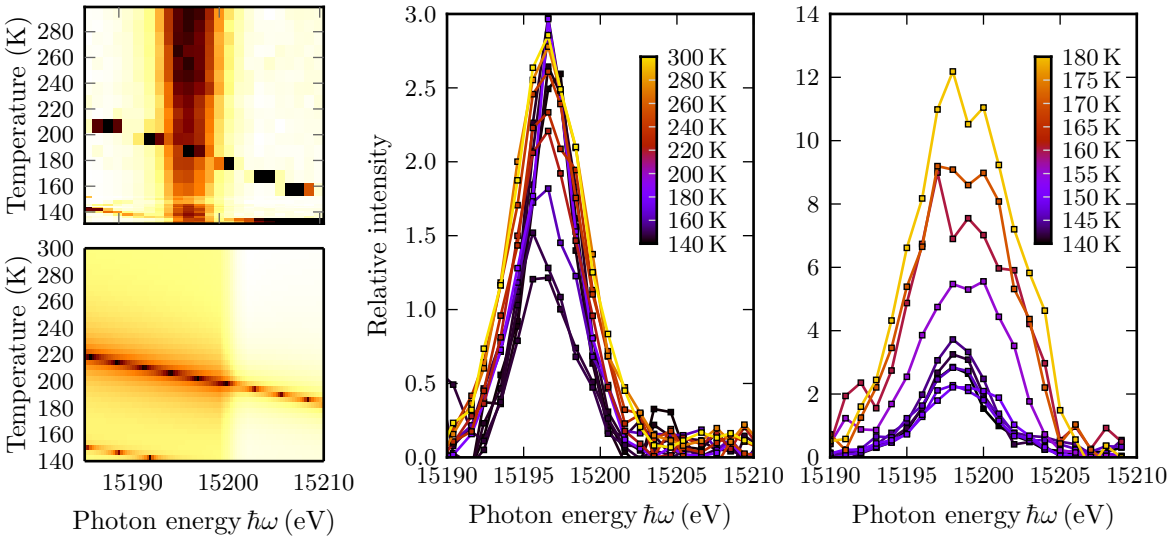

Fig. 4.31.: The integrated intensity of the 006 reflection as a function of energy and temperature (top left) showing a strong influence of multiple reflections ("Renninger effect") as revealed by calculations of the latter (bottom left). The forbidden reflection is visible as maximum at constant energy ($\approx 15196\,\mathrm{eV}$), whereas Renninger reflections occur at different energy for each temperature, since their position depends on the lattice parameters. Energy spectra of the resonant reflections 006 (middle) and 550 (right) filtered for Renninger effect at various temperatures showing that there is a minimum in intensity at about 148 K. Above the phase transition temperature, the 550 reflection exhibits a significantly higher energy width than the 006 reflection.

see that the reflection degradation is stronger at lower temperature. During the measurements the samples have been cooled and heated several times. This way, healing of the crystals at higher temperatures was observed indicating that two competing processes are taking place. To minimize the effect of radiation damage on the measured spectra, the beam has been slightly defocused and attenuated. Furthermore, different positions on the sample surface were illuminated for data acquisition and the intensity has been corrected for radiation damage according to the time of illumination and the bi-exponential time dependence which was shown in Fig. 4.32.

The resulting temperature dependence obtained this way is shown on the right in Fig. 4.32. To correct for the conventional temperature dependence in x-ray diffraction, the integrated intensities have been divided by the Debye-Waller factor taken from literature [KN80]. It can be seen that both reflections feature a decrease of integrated intensity with decreasing temperature as long as remaining in the paraelectric phase. This gives evidence for the TMI part of forbidden reflections. Furthermore, a step-like increase of the intensity can be observed when cooling below the phase transition temperature. This enhancement can be understood based on the reduced site symmetry of the rubidium atom in the ferroelectric phase.

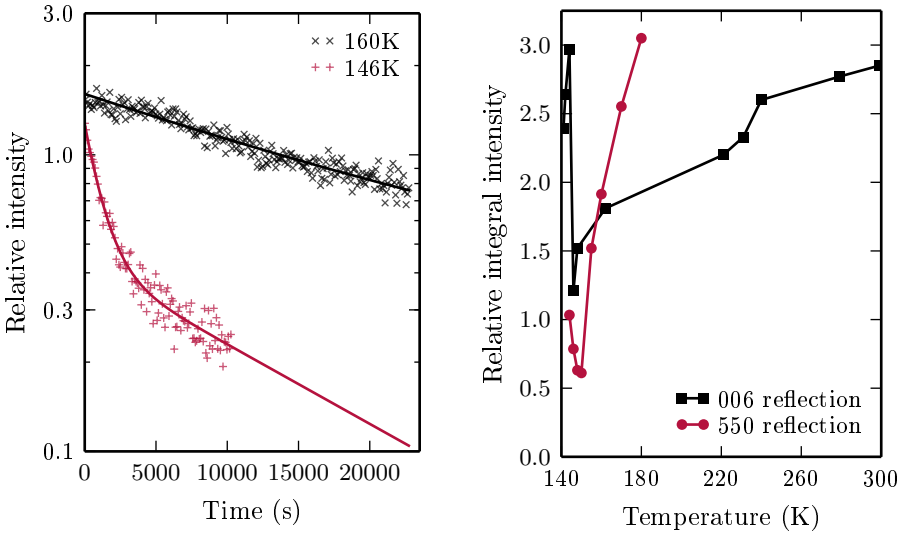

Fig. 4.32.: Left: Time dependence of Bragg intensity for different temperatures: manifestation of radiation damage to the crystal structure competing with healing processes at higher temperature. Solid lines indicate the bi-exponential fit which was used to correct for radiation damage. Right: Temperature dependence of integrated intensity for the 006 and 550 Bragg reflections after correcting for radiation damage according to the exposure time.

Analysis of forbidden reflections spectra – paraelectric phase

To identify the origins of anisotropy that lead to the observation of the forbidden reflections, an interpretation of the energy dependence is necessary next to the study of thermal behavior. It could be seen in Fig. 4.32 that the 550 reflection intensity grows much faster with temperature than for the 006 reflection. The corresponding spectra in Fig. 4.30 also show qualitative differences.

Referring to the structure amplitudes of 006 and 550 in Eqs. (4.14,4.15), there are two tensor components which contain contribution due to defects:

$$I^{xxz}_{\mathrm{Rb}+} \rightarrow I^{xxz}_{\mathrm{Rb}+} + a_1 D^{xxz}_{\mathrm{Rb,PDI}} + a_2 D^{xxz}_{\mathrm{Rb,TMI}} \qquad \text{and}$$
$$I^{zxx}_{\mathrm{Rb}+} \rightarrow I^{zxx}_{\mathrm{Rb}+} + b_1 D^{zxx}_{\mathrm{Rb,PDI}} + b_2 D^{zxx}_{\mathrm{Rb,TMI}},$$

respectively. The former is sensitive to displacement in z and the latter to displacement in x/y-direction. The unknown coefficients, a_1, a_2, b_1 and b_2, have been introduced which describe the occurrence of the defects and will be subject to fitting. We discussed before the symmetry of polar and Slater defects (see Fig. 4.29). Based on this it can already be concluded that the polar defects cause a displacement in the z-direction whereas Slater defects are those which mainly cause a deformation of the environment in the x/y plane. For both polar and Slater defects, there are several manifestations which all result the same third rank PDI tensor component after weighting with the corresponding displacement $\mathbf{u}_j$. The computation of the tensor components for both PDI and TMI components has been performed at the *Moscow*

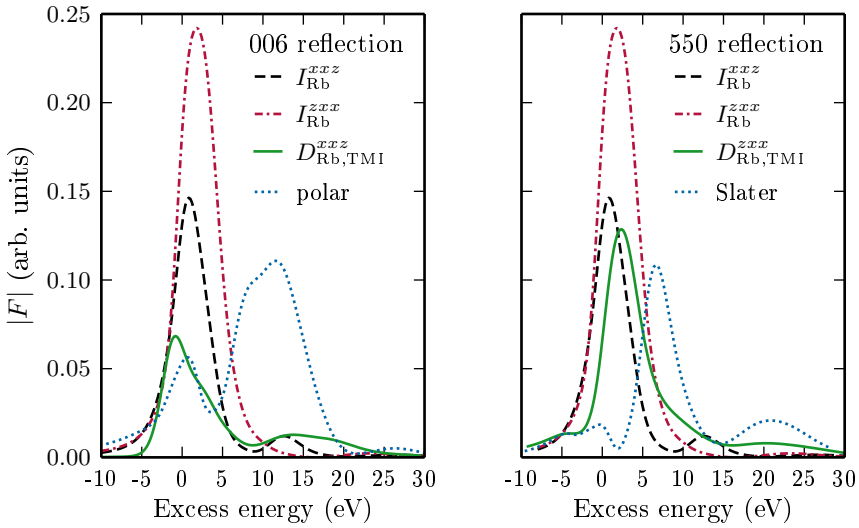

Fig. 4.33.: The modulus of the dipole-quadrupole, TMI and PDI (including polar and Slater) contributions to the third rank structure amplitude of the 006 (left) and 550 (right) reflections. The data is shown as a function of energy corresponding to the difference of photon energy to edge position (15196 eV). The contributions are scaled aiming to see their shape and the position in energy.

State University (MSU) and a detailed description has been published [Aki+14; Ric+14]. Nevertheless, the essence shall be discussed here.

For the calculation of the TMI contributions, only the linear approximation, Eq. (4.10), has been taken into account which relates to an exclusive movement of the resonant atom while the surrounding atoms are fixed. Although a detailed study of the TMI effect has shown that it is provided by thermal displacements of atoms in several coordination spheres, the main contribution arises from the displacement of the resonant atom itself. To calculate the linear response of the dipole-dipole tensor $D^{\alpha\beta}$ in Eq. (4.10) the partial derivatives are obtained by calculating the change of the dipole-dipole tensor components upon small, finite displacement (≈ 0.001 of the unit cell dimension) of the resonant atom while the other atoms remain fixed.

To model the PDI contributions due to polar and Slater defects, the relaxed local structure, which forms after specification of the hydrogen positions, is needed. This has been done at the MSU using the DFT code VASP [KF96] and results in a displacement of rubidium $\mathbf{u}_{\mathrm{Rb}}$. Based on the new local structure, the dipole-dipole tensor $D^{\alpha\beta}_{\mathrm{Rb}}(\mathbf{u}_{\mathrm{Rb}})$ can be calculated using, e. g., FDMNES [Jol01]. Multiplied with the displacement $\mathbf{u}_{\mathrm{Rb}}$ and averaged over all realizations of the defect that are allowed by symmetry, the PDI contribution to the third rank tensor $D^{\alpha\beta\gamma}_{\mathrm{Rb,PDI}}$ (see Eq. (4.11)) is obtained. This way, it could be verified that polar defects contribute to the $I^{xxz}_{\mathrm{Rb+}}$ and Slater defects to the $I^{zxx}_{\mathrm{Rb+}}$ tensor. The calculated spectra are shown in Fig. 4.33.

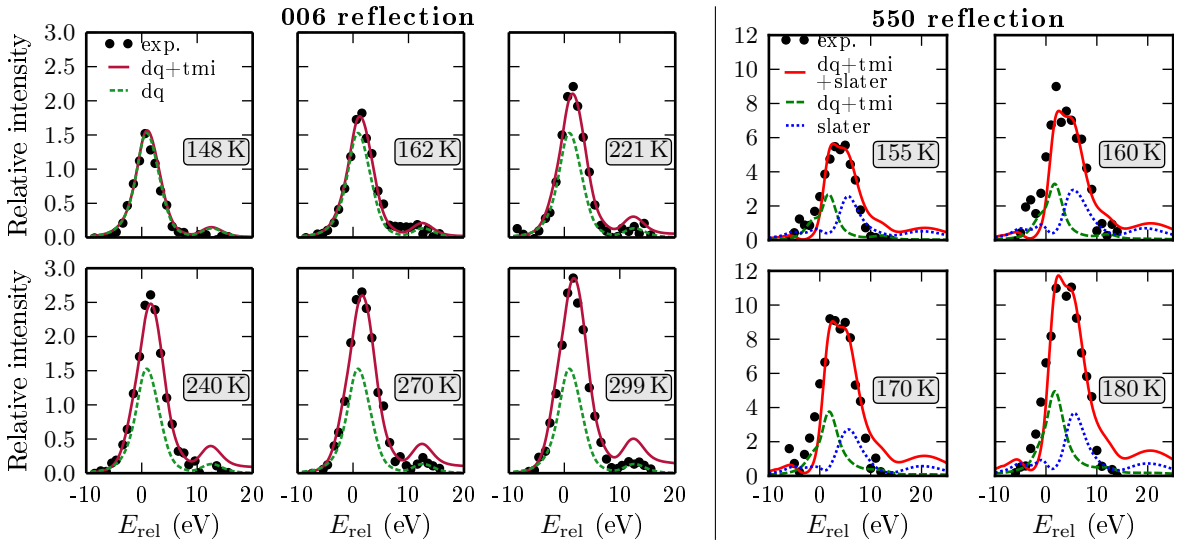

Fig. 4.34.: Analysis of the energy dependencies of the different Bragg reflections with respect to a changing temperature. Columns 1 to 3: 006 reflection. Columns 4,5: 550 reflection. The profiles have been fitted with a coherent sum of the various contributions to the third rank tensor (dipole-quadrupole scattering, TMI and PDI terms) to the measurement through variation of the coefficients a_1, a_2, b_1 and b_2. A Slater type PDI contribution was observed in the spectra of the 550 reflection.

It can be seen that the peaks corresponding to thermal motion or to intrinsic dipole-quadrupole scattering are found roughly at the same energy whereas the PDI contributions produce additional intensity at higher energies. This allows to conclude about the presence of defects already, since the spectra of 006 and 550 reflection have different widths (see Fig. 4.31). As the measured spectra of the 006 reflection have a narrow distribution on energy, one can conclude that they can be described based on TMI and intrinsic dipole-quadrupole contributions only. No evidence of polar defects is obvious. For the 550 reflection, the width of the simulated spectra for temperatures between 160 K and 180 K is much lower than that in the experimental curves. This discrepancy can be explained by the influence of the Slater term. However, the measured intensity depends on the coherent sum of all contributions which is why a conclusion based on the plotted modulus cannot be drawn yet. The result of fitting the coherent sum of the calculated contributions to the measured spectra based on the variation of the coefficients (a_1, a_2, b_1, b_2) is shown in Fig. 4.34. A temperature dependence of the PDI contribution to the form factor of the forbidden reflections may exist because the number of defects changes with temperature. It is obvious that the measurements of the 006 reflection can be explained considering only dipole-quadrupole scattering together with the TMI part. In contrast, the spectra of the 550 reflection are broadened, indicating the contribution of Slater-type defects that show only a weak temperature dependence. The resulting coefficients are presented in Fig. 4.35 on relative scale. Absolute values could not be given here, since the intrinsic dipole-quadrupole is overlapped be the thermal motion induced (TMI) part. Therefore, a reference is missing, but it can be stated that the defect induced (PDI) contribution has an effect on a similar scale as the TMI part. The occurrence of Slater defects next to polar ones

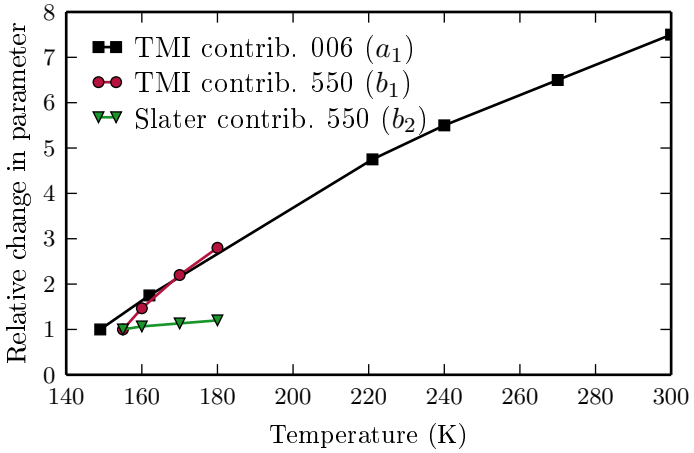

Fig. 4.35.: Coefficients weighting the different contributions to the third rank tensor as they were obtained by fitting the measurements (see Fig. 4.34) as a function of temperature. As expected, the TMI part grows with temperature whereas the Slater type contributions hardly depend on temperature in the given range.

has been observed recently in KDP using the same method [Beu+15]. The absence of polar configurations in the present work merits further investigations. A more detailed measurement of the spectra would be possible by using a higher order monochromator (Si-311 or 511) to increase the energy resolution and by using a parallel, unfocused beam to keep the radiation damage low. Also a characterization of the PDI contribution from Slater configurations over a larger temperature range would allow to give estimates on the activation energies as it was done in [Beu+15].

5. Conclusion and Outlook

The present thesis outlines and expands the opportunities for crystal structure analysis that are gained in materials science with the consideration of *resonant x-ray diffraction* (RXD) techniques. Thereby, the efforts were focused on studies of the crystallographic charge density. The benefits of RXD result from a combination of two established branches of x-ray structure analysis methods – diffraction and spectroscopy. Therefore, there are essentially two ways of convergence of the two methods, both of which have been followed in this work. On the one hand, the possibilities of diffraction can be enhanced by the variation of atomic scattering amplitudes providing additional of information. On the other hand, spectroscopy can be performed in diffraction mode which, instead of averaging, yields a weighted sum of atomic absorption spectra allowing to isolate spectra of atoms on specific crystallographic positions.

The set of RXD methods was extended in this work both by establishing a new technique, based on the targeted suppression of reflections, and by further development of existing techniques. These have been employed to answer recent questions of crystallography in several examples. The applications were concentrated on the study of structural modifications of crystals where an approximate model already existed. For instance, different ways were presented to determine slight atomic displacement from higher-symmetry positions using RXD. Other applications are the localization of foreign atoms or characterization of defects. The results therefore can be categorized into methodological developments and crystal structure refinement.

In particular, it has been shown that *diffraction anomalous fine structure* (DAFS) can be applied to study the local environment of only those resonant atoms which are contained in the crystalline fraction of a polycrystalline sample. This was done for titanium environments in a complex layered material, hydrazinium titanate (LHT, see Section 4.1.2), that exhibits a high degree of disorder. X-ray spectroscopy showed evidence of unusual titanium coordination geometries that have been ascribed to disordered, non-crystalline regions in the substance [Bri+11]. An abundance of 5-fold coordinated titanium [TiO_5] including short titanyl bonds (Ti=O) at the interface regions between crystallites has been assumed to explain the observed spectral features. In contrast to that, the presented DAFS measurements clearly show that the same features are expressed in absorption spectra of the purely crystalline parts of LHT. This contradicts with the existing structural model and should be examined in more detail. Using DAFS spectra of several reflections and better counting statistics, it will be possible to

conclude about the number of inequivalent titanium sites as well as the coordination geometry for each of them.

In addition to that, the intercalation of a foreign atom into LHT was investigated for the example of selenium. DAFS measurements on the absorption edge of the impurity can yield two answers in such situation. Firstly, the location of the foreign atom with respect to the crystal lattice can be determined from the coarse energy dependence of a set of Bragg reflections (at least 3). Secondly, the bond lengths can be extracted from fine structure oscillations. In the present case, several possible solutions for the selenium positions were found, while two of them stand out. In all cases, the position was found between the titanate sheets in proximity of the hydrazinium ion.

As a second material class, polar thin films have been analyzed for their atomic and domain structure. For the latter, the violation of Friedels law in resonant diffraction was used. It allows to distinguish opposing reflections and therefore to resolve inversion domains of polar materials. This way, the absolute polarization of ultra thin, epitaxial $BaTiO_3$ films has been determined. Secondly, the dynamics of domain wall motion in dependence of applied DC voltage has been characterized. This showed a strong asymmetry with respect to changing sign of the voltage indicating an influence of pinning of domain walls.

Closely related, the atomic structure of polar $SrTiO_3$ films has been studied. In particular, these were strained, singlecrystalline layers that are forming on cubic $SrTiO_3$ substrates under influence of an external electric field after several hours (see Section 4.2.2). Using a new resonant x-ray diffraction technique based on targeted, resonant suppression of diffraction (RSD), it was possible to show that these strained layers have a polar atomic structure corresponding to that of $BaTiO_3$. This finding explains piezoelectric and pyroelectric properties that have been observed in the new structure. Moreover, the polar atomic displacements could be determined with a precision of approximately 1 pm. Since it does only rely on the relative intensity variations of a few reflections with changing wavelength, the new method has the potential to give atomic positions with unprecedented resolutions for crystalline materials in a restricted geometry. These comprise thin films, nanorods and other low-dimensional systems. The general applicability of the method for other materials has been discussed. Currently, a refinement of several unknown structural parameters requires the measurement of the energy dependence of different reflections. This complication may be overcome in the future by an analysis of intensity variations due to Renninger effect which occur upon rotation around the scattering vector in a small region.

Another very sensitive approach to study atomic displacements is based on the violation of crystallographic selection rules as it can occur in *anisotropy in anomalous scattering* (AAS).

This results in appearance of 'forbidden' reflections that can only be observed in a small energy range near the absorption edge. Nowadays, there are several software packages that allow to compute these very pronounced spectra *ab-initio*, e. g. based on the atomic structure. However, the spectra can be dominated by contributions from local deviations from the average (ideal) crystal structure. These exist due to both dynamic displacement (thermal motion) as well as static displacement (defects). The mechanism of thermal motion and point defect induced forbidden reflections has been described in Section 4.3. The two contributions can be disentangled by characterization of their energy and temperature dependence. The technique was applied to study transient hydrogen configurations in single crystals of the hydrogen bonded material rubidium dihydrogen phosphate RbH_2PO_4 (RDP). The transient configurations occur locally since hydrogen is statistically occupying two minima of a symmetric double well potential between two oxygen atoms. It was found that thermal motion is the largest contribution to the considered forbidden reflections but that a complete description of their spectra is only possible when including defects. The kind of defect which has been detected this way involves a deformation of the $[PO_4]$ tetrahedra in the *a*-*b* plane therefore being nonpolar in average. The absence of polar defects stands in contrast to recent observations made in the isomorphous material KH_2PO_4 (KDP) and motivates further studies.

Two of the presented methods are still new – AAS and RSD. Their application is rather time consuming and they deserve further development to become accessible for the broad community of material scientists. On the other hand, the method DAFS is nowadays well understood and recent algorithms allow a data analysis that does not require manual adjustment of parameters. Therefore, an automated implementation of the measurement and the reduction of data is now feasible for powder samples. As a result, the fine structure function for each resonant atom is obtained. The basis for that has been compiled in Section 3.3.2. Remarkably, a review article on this topic has been published during completion of this thesis [KFM16]. While there are no dedicated end stations to powder DAFS, an adaptation of *extended XAFS* (EXAFS) beam lines require only little modifications.

A. Supplementary information

A.1. The EXAFS function

In the extended energy region and normalized to the jump height of the smooth imaginary part of the scattering amplitude, the fine structure function (see Section 3.3.2) can be interpreted in terms of spherical wave photoelectron diffraction from the surrounding structure [Sor+94; FWC98] through the so-called EXAFS-equation (for single scattering):

$$\frac{\tilde{\chi}}{f_s''}(k_\mathrm{e}) = \sum_j^N \frac{S_0^2}{k_\mathrm{e} r_j^2} \left| f_j^\mathrm{e}(k_\mathrm{e}) \right| \mathrm{e}^{\mathrm{i}\left(2k_\mathrm{e} r_j + \phi_j^\mathrm{e}(k_\mathrm{e}) + 2\delta_c(k_\mathrm{e})\right)} \mathrm{e}^{-2\sigma_j^2 k_\mathrm{e}^2} \mathrm{e}^{-2r_j/\Lambda(k_\mathrm{e}^2)}. \tag{A.1}$$

Here, j denotes a certain scattering path each described by an effective length r_j, an effective Debye-Waller factor σ_j and the photoelectron scattering amplitude described by $(|f_j^\mathrm{e}|, \phi_j^\mathrm{e})$. The additional phase shift δ_c stems from the absorbing atom and is equal for all paths. Furthermore, Λ takes account of limited mean free path and core hole lifetime, and S_0 is a scaling factor. The wavenumber of the photoelectron is calculated based on the de Broglie wavelength from the energy surplus with respect to the edge energy E_0 as

$$k_\mathrm{e} = \sqrt{2m\,(E - E_0)}. \tag{A.2}$$

A.1.1. Comparison with density functional theory calculations

In Section 4.2.2, the atomic structure of *migration induced, field-stabilized, polar* (MFP) (MFP) phase, that forms under incluence of an electric field, has been determined. The results were obained for a fixed value of strain $^{\Delta c}/_{c} = 0.15\,\%$. To compare the obtained atomic displacements for the MFP phase with theory, electronic structure calculations using *density functional theory* (DFT) have been performed. The effects caused by the external electric field have been emulated by imposing relative atomic displacements $\Delta z/c$ of titanium and oxygen in field direction as they were experimentally found for the MFP phase according to Table 4.3. This was followed by geometrical relaxation of the MFP unit cell size yielding its strain as well as its polarization. The results are given in Table A.1. The technical details of the DFT simulations include

- software package: VASP [KF96],
- *projector-augmented wave* (PAW) technique for electronic structure calculations [KJ99],
- PBE parameterization [PBE96],
- total energies have converged better than $10^{-10}\,\mathrm{eV}$,
- maximum kinetic energy of 450 eV for the plane-wave basis set,
- Γ-centered $12 \times 12 \times 12$ Monkhorst-Pack k-point meshes with spacings less than $0.02 \times 2\pi\mathrm{\AA}^{-1}$

For the evaluation of strain, relative atomic positions were kept fixed and the cell geometry was relaxed within the space group to forces less than $10^{-5}\,\mathrm{eV/\AA}$. The change in polarization has been assessed within the framework of Berry-phase treatment [KV93]. The strain obtained

Tab. A.1.: Changes in lattice parameters for the MFP phase obtained by means of DFT after imposing relative atomic displacements as found in the experiment (see Table 4.3). Strain parameters including Poisson's ratio ν, as well as electronic (Δp_{elec}) and ionic (Δp_{ion}) dipole moment per unit cell caused by the atomic displacements are presented.

	a (Å)	c (Å)	$\Delta a/a$	$\Delta c/c$	ν	Δp_{ion} (eÅ)	Δp_{elec} (eÅ)	Δp_{tot} (eÅ)
STO	3.947261	3.947261	-	-	-	-	-	-
MFP	3.945461	3.955710	-0.0456%	0.2136%	0.214	-0.508	0.940	0.432

by energy minimization is slightly larger but still close to the measured value of 0.15 %. This

can be explained, e. g., with the elastic interaction of the MFP phase with the bulk. The Poisson's ratio is not affected by this interaction and even better matches the values that were observed before in [Han+13].

A.2. Hydrogen jumps in RbH_2PO_4

In RDP, rubidium occupies a Wyckoff site with symmetry $\bar{4}$. As a consequence, the second $\left(D_{\mathrm{Rb}}^{\alpha\beta}\right)$ and third $\left(I_{\mathrm{Rb}}^{\alpha\beta\gamma}\right)$ rank tensors take the form:

$$D_{\mathrm{Rb}}^{\alpha\beta} = \begin{pmatrix} D_{\mathrm{Rb}}^{xx} & 0 & 0 \\ 0 & D_{\mathrm{Rb}}^{xx} & 0 \\ 0 & 0 & D_{\mathrm{Rb}}^{zz} \end{pmatrix},$$

$$I_{\mathrm{Rb}}^{\alpha\beta\gamma} = \underbrace{\begin{pmatrix} 0 & 0 & I_{\mathrm{Rb}}^{xzx} \\ 0 & 0 & I_{\mathrm{Rb}}^{yzx} \\ I_{\mathrm{Rb}}^{zxx} & I_{\mathrm{Rb}}^{zyx} & 0 \end{pmatrix}}_{\gamma=x}, \underbrace{\begin{pmatrix} 0 & 0 & I_{\mathrm{Rb}}^{yzx} \\ 0 & 0 & -I_{\mathrm{Rb}}^{xzx} \\ I_{\mathrm{Rb}}^{zyx} & -I_{\mathrm{Rb}}^{zxx} & 0 \end{pmatrix}}_{\gamma=y}, \underbrace{\begin{pmatrix} I_{\mathrm{Rb}}^{zxx} & I_{\mathrm{Rb}}^{yzx} & 0 \\ I_{\mathrm{Rb}}^{yzx} & -I_{\mathrm{Rb}}^{zxx} & 0 \\ 0 & 0 & 0 \end{pmatrix}}_{\gamma=z},$$

where γ denotes the wavevector component and α, β correspond to polarization vector components of incoming and scattered x-ray beam, respectively.

```
%pylab inline
import pyasf
import sympy as sp
```

```
struct = pyasf.unit_cell(186) # corresponds to P63 m c
```

```
Setting up space group 186...
Hexagonal
```

```
z_N = sp.Symbol("z_N", real=True, positive=True) # variable for z position of nitrogen
```

```
struct.metric_tensor # shows hexagonal metric of GaN
```

```
Matrix([
[   a**2, -a**2/2,    0],
[-a**2/2,    a**2,    0],
[      0,       0, c**2]])
```

```
struct.add_atom("Ga1", ["1/3","2/3",0], isotropic=False, charge=3)
struct.add_atom("N1", ["1/3","2/3",z_N])
```

```
struct.subs[z_N] = 0.337 # provide numeric values in .subs
struct.subs[struct.a] = 3.181
struct.subs[struct.c] = 5.184
```

```
struct.AU_positions # asymmetric unit
```

```
{'Ga1': array([1/3, 2/3, 0], dtype=object),
 'N1': array([1/3, 2/3, z_N], dtype=object)}
```

```
struct.U["Ga1"] # atomic displacement parameters
```

```
Matrix([
[U_Ga1_11, U_Ga1_12, U_Ga1_13],
[U_Ga1_12, U_Ga1_22, U_Ga1_23],
[U_Ga1_13, U_Ga1_23, U_Ga1_33]])
```

```
struct.get_tensor_symmetry() # based on space group generators
struct.build_unit_cell() # produce all equivalent atoms of the orbit
```

```
struct.U["Ga1"] # after application of symmetry
```

```
Matrix([
[  U_Ga1_22, U_Ga1_22/2,         0],
[U_Ga1_22/2,   U_Ga1_22,         0],
[         0,          0, U_Ga1_33]])
```

```
struct.positions["N1"] # Orbit of nitrogen
```

```
[array([1/3, 2/3, z_N], dtype=object),
 array([2/3, 1/3, z_N + 1/2], dtype=object)]
```

```
struct.calc_structure_factor((2,2,2)) # calculates up to rank 3 but only returns scalar
```

```
2*f_Ga1_0*exp(-32*pi**2*U_Ga1_22/a**2 - 8*pi**2*U_Ga1_33/c**2)
+ f_N*exp(2*I*pi*(2*z_N + 2))*exp(-32*pi**2*U_N1_22/a**2 - 8*pi**2*U_N1_33/c**2)
+ f_N*exp(2*I*pi*(2*z_N + 3))*exp(-32*pi**2*U_N1_22/a**2 - 8*pi**2*U_N1_33/c**2)
```

```
print struct.F_DD.shape, struct.F_DQin.shape # shapes of higher orders (long expressions)
```

```
(3, 3) (3, 3, 3)
```

```
"""
    doing numeric evaluation using table values from rexs package
    (neglecting debye waller factor)
"""
# define energy range in eV
Energy = np.linspace(10000,11000,1001)
F1 = struct.DAFS(Energy, (2,2,2), Temp=False, table="Sasaki")
F2 = struct.DAFS(Energy, (4,4,4), Temp=False, table="Sasaki")
plt.semilogy(Energy, abs(F1)**2)
plt.semilogy(Energy, abs(F2)**2)
```

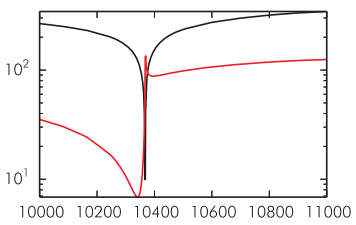

Fig. A.1.: (See Section 3.3.2) An example code in Python that shows how to use the pyasf package [Ric16a] to analyze tensor symmetry in gallium nitride, to calculate the energy dependence of Bragg reflections based on tabulated data or to do other crystallographic calculations.

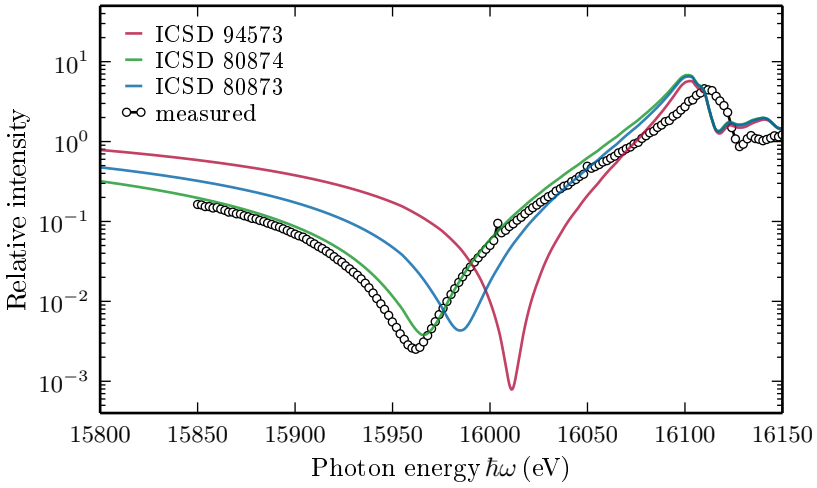

Fig. A.2.: (See Section 4.2.2) Calculated energy dependencies near resonant suppression of diffraction (RSD) for the 007 reflection of different structure entries of the *Inorganic Crystal Structure Database* (ICSD) [M H04] that correspond to $SrTiO_3$ at room temperature. One can see different predictions one of them lying near the measured curve. The strong differences motivated a refinement of the anisotropic Debye-Waller Factors that are different for each entry.

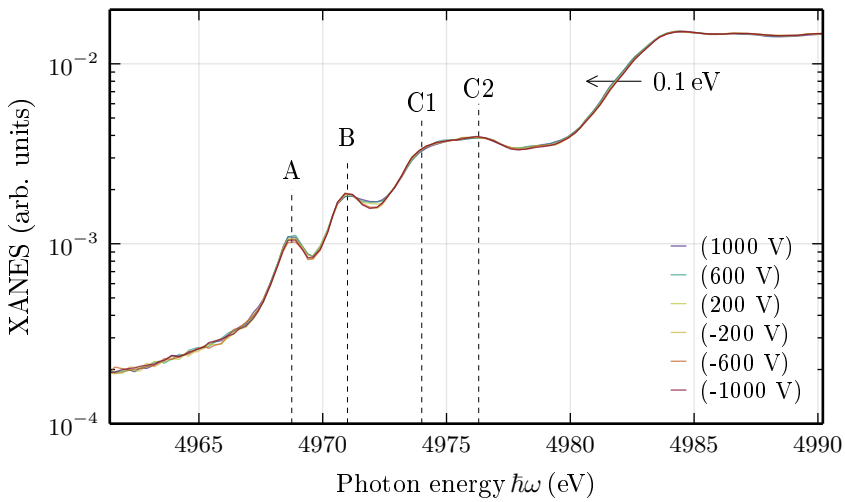

Fig. A.3.: (See Section 4.2.2) Grazing incidence *x-ray absorption near edge spectroscopy* (XANES) measurements on the anode side of the $SrTiO_3$ single crystal in the titanium pre-edge region during forming of the MFP phase (changing voltage from $-1000\,\mathrm{V}$ to $1000\,\mathrm{V}$). Slight changes can be seen: a small edge shift of $\approx 1\,\mathrm{eV}$ and additional density between peaks B and C1.

Abbreviations

AAS *anisotropy in anomalous scattering*. 8, 10, 13, 116, 117

ADP atomic displacement parameter. 91, 93, 95, 96

AFM *atomic force microscopy*. 80, 83, 84

BTO barium titanate $BaTiO_3$. 55, 57, 58, 79–83, 87

COD *Crystallography Open Database*. 99, 100

DAFS *diffraction anomalous fine structure*. 7, 9, 13, 21, 36, 51, 53, 55, 57, 59–62, 65–67, 69–75, 77, 115–117

DESY Deutsches Elektronen-Synchrotron. 69, 108

DFT *density functional theory*. 103, 111, 120

DWBA *distorted wave Born approximation*. 27

ESRF European Synchrotron Radiation Facility. 83, 90

EXAFS *extended XAFS*. 36, 48, 49, 68, 69, 72, 73, 77, 91, 117, 119

FTIR *fourier transform infrared spectroscopy*. 68

ICSD *Inorganic Crystal Structure Database*. 123

KDP KH_2PO_4. 104, 106, 113

KK Kramers-Kronig. 25, 52–57, 66, 74

LDR *logarithmic dispersion relations*. 7, 55, 57, 58

LHT Layered Hydrazinium Titanate. 68–71, 73, 76, 77

LSMO lanthanum strontium manganite. 82

MAD *multi-wavelength anomalous dispersion*. 13

MFP *migration induced, field-stabilized, polar*. 87, 90, 94–98, 120

MSKK *multiply subtractive Kramers-Kronig*. 25

MSU *Moscow State University*. 110, 111

PDI *point defect induced*. 103, 107, 110–113

PFM *piezoresponse force microscopy*. 80, 83

PLD *pulsed laser deposition*. 80

PSD position sensitive detector. 63, 74

RDP rubidium dihydrogen phosphate RbH_2PO_4. 104, 117, 121

REXS *resonant elastic x-ray scattering*. 17

RMS *resonant magnetic scattering*. 13

RXD *resonant x-ray diffraction*. 12, 14, 15, 19, 43, 45, 47, 51, 55, 59, 60, 69, 70, 73, 79–81, 97, 100, 115

SEM *scanning electron microscopy*. 80

STO strontium titanate $SrTiO_3$. 87–91, 94, 97–100

TMI *thermal motion induced*. 103, 104, 107, 110–113

XAFS *x-ray absorption fine structure.* 19, 21, 36, 51, 59–61, 65, 70, 71, 94

XANES *x-ray absorption near edge spectroscopy.* 68, 69, 71, 72, 94, 123

XRD *x-ray diffraction.* 61, 63

Nomenclature

$\mathbf{A}$ vector potential of the x-ray radiation.
A_0 field amplitude of the incoming photon.
α angle between incoming beam and sample surface (if not index).

β angle between scattered beam and sample surface (if not index).

c vacuum speed of light.
$\tilde{\chi}$ fine structure function.

d thickness of the sample.

e elementary charge.
E_ξ energy of state $|\xi\rangle$.
$\boldsymbol{\varepsilon}$ polarization vector of the photon.

f scattering factor or scattering amplitude of an atom.
f', f'' real and imaginary part of the resonant dispersion correction to the scattering factor.
F complex structure amplitude.

Γ level width of the core electron.

$\hbar$ reduced Planck constant.

I intensity of the scattered x-ray beam.
I_0 intensity of the incoming x-ray beam.

$\mathbf{k}$ wave-vector of the photon.
k magnitude of the wave-vector $k = |\mathbf{k}|$.
$\mathbf{K}$ wavevector transfer or scattering vector: $\mathbf{K} = \mathbf{k} - \mathbf{k}'$.

m electron mass.
$h_i = (h, k, l)$ Miller indices.
μ linear absorption coefficient.

ω angular frequency of the photon.

$\mathbf{p}$ momentum of the electron.

$\mathbf{r}$ position vector (e. g. of an atom).

σ_{int} integral scattering cross section.

θ_{B} Bragg angle: angle between lattice planes and x-ray beams.

$\mathbf{u}$ atomic displacement vector, $\mathbf{r} = \mathbf{r}^0 + \mathbf{u}$.

Acknowledgement

I want to express my deep gratitude to everybody who contributed to this work.

In particular, I want to thank Prof. Dirk C. Meyer for introducing me to the topic of x-ray crystallography and for entrusting me with the project on resonant diffraction where I could benefit from his years of experience and his pioneering works on the topic.

I am very grateful and honored that the second review of my thesis will be conducted by Prof. Vladimir E. Dmitrienko. I enjoyed the collaboration with him and Prof. Elena N. Ovchinnikova and profited from their ideas in the field of x-ray diffraction. In particular, I want to thank for assignment of the experimental work regarding rubidium dihydrogen phosphate. In this context, I also want to express my gratitude to all their colleagues that were involved in this work and whom I met during my stay in Moscow.

I am particularly thankful to Dr. Dmitri Novikov who was a constant source of advice throughout my time as PhD and thanks to whom I made various valuable and important acquaintances. He was a support during many days and nights of experiments and enabled me to gather a lot of experience both in and outside DESY. He also was an invaluable help for the completion of this thesis and always motivated me to look a little deeper if the data did not seem promising.

I want to express special thanks to my group ("solid state spectroscopy") in Freiberg without whom my PhD time would not have been as enjoyable. The atmosphere in the group was always friendly and characterized by the desire to exchange knowledge and expertise in the very different fields. This is why I always felt at home during my visits to Freiberg. I am grateful to Dr. Matthias Zschornak for repeatedly explaining the theoretical aspects of x-ray spectroscopy, proofreading this thesis and for inspiring ideas for experimental projects. I highly appreciate the discussions both in oral and written form that I had with Dr. Hartmut Stöcker and Mr. Erik Mehner. They have been especially helpful while planning the diverse and challenging experimental setups in this work. I also want to thank Mrs. Melanie Nentwich for her diligence in our joint projects, her efforts on the data analysis and for reading parts of my thesis with great rigor. For the outstanding support during different beamtimes and for sample preparation, I additionally thank Dr. Juliane Hanzig and Mr. Thomas Köhler. Last but not least, I am grateful for many interesting discussion with Dr. Tilmann Leisegang, Mr. Falk

Meutzner and Mrs. Tina Nestler, as well as for help from Dr. Claudia Funke, Mrs. Stefanie Schmidt and Mrs. Alexandra Gleißner regarding the coordination of projects.

Furthermore, I want to thank Dr. Sergey Britvin, Jun.-Prof. Roman Gumeniuk, Dr. Enver Kh. Mukhamedzhanov, Dr. Andrey Zenkevich and Mrs. Ksenia Maksimova for providing ideas, samples and help for experiments. For excellent support as local contacts during different beamtimes, I am grateful to Dr. Jörg Strempfer, Dr. Sonia Francoual, Dr. Simon Brown, Dr. Carsten Bähtz, Dr. Oier Bikondoa and Dr. Jan Hilhorst.

I am especially grateful to all the colleagues and friends that I met at DESY, for their help as well as for a pleasant work atmosphere and activities outside work: Ulla Vainio, Matthias Schwartzkopf, Torsten Golz, Denise Erb, Christoph Wollstein, Ligia Martín, André Rothkirch, Wojciech Roseker, Stephan Botta, Torsten Laurus, Jan Perlich, Tatyana Guryeva, Rainer Gehrke, Tobias Lapsien, Heiko Schulz–Ritter, Jana Raabe, Katrin Ederer, Raphael Grifone, Ksenia Maksimova, Ilja Schostak, Dina Sheyfer, Juliane Reinhardt, Artur Lobanov, Oskar Hartbrich, Eike von Seggern and many more. I also want to thank the DESY/Volkspark football group for many nice games that helped me to clear my mind.

My deepest gratitude goes to my parents, Gudrun and Volker, that always have been supporting me even though I could not spend much time with them in the last years, and to Maria for sharing all moments – good or bad – during this time. Without them I would not have found the strength to complete this work.

Bibliography

[Abr+95] Y. A. ABRAMOV et al. "The chemical bond and atomic displacements in $SrTiO_3$ from X-ray diffraction analysis". In: *Acta Crystallographica Section B* 51.6 (Dec. 1995), pp. 942–951. DOI: 10.1107/S0108768195003752 (cit. on pp. 91, 92).

[AD75] C. A. ASHLEY and S. DONIACH. "Theory of extended x-ray absorption edge fine structure (EXAFS) in crystalline solids". In: *Phys. Rev. B* 11 (4 Feb. 1975), pp. 1279–1288. DOI: 10.1103/PhysRevB.11.1279 (cit. on p. 48).

[Aki+14] K. A. AKIMOVA et al. "Methods for calculating the resonant part of the atomic factor in crystals with partial filling of the crystallographic position". In: *Journal of Surface Investigation. X-ray, Synchrotron and Neutron Techniques* 8.2 (Mar. 2014), pp. 384–390. DOI: 10.1134/s1027451014020268 (cit. on pp. 104, 111).

[AlK+78] A. R. AL-KARAGHOULI et al. "A precision neutron diffraction study of tetragonal RbH_2PO_4". In: *Acta Crystallographica Section B* 34.3 (Mar. 1978), pp. 1040–1042. DOI: 10.1107/S0567740878004811 (cit. on p. 104).

[AM11] J. ALS-NIELSEN and D. MCMORROW. *Elements of Modern X-ray Physics*. Wiley-Blackwell, Mar. 2011. DOI: 10.1002/9781119998365 (cit. on pp. 33, 40, 63).

[Arn+82] U. W. ARNDT et al. "Optimized anomalous dispersion in crystallography: a synchrotron X-ray polychromatic simultaneous profile method". In: *Nature* 298.5877 (Aug. 1982), pp. 835–838. DOI: 10.1038/298835a0 (cit. on p. 13).

[Aro+06] M. I. AROYO et al. "Bilbao Crystallographic Server. II. Representations of crystallographic point groups and space groups". In: *Acta Crystallographica Section A* 62.2 (Mar. 2006), pp. 115–128. DOI: 10.1107/S0108767305040286 (cit. on p. 34).

[Ash+15] G. ASHIOTIS et al. "The fast azimuthal integration Python library: *pyFAI*". In: *Journal of Applied Crystallography* 48.2 (Apr. 2015), pp. 510–519. DOI: 10.1107/S1600576715004306 (cit. on p. 63).

[Att90] J. P. ATTFIELD. "Determination of valence and cation distributions by resonant powder X-ray diffraction". In: *Nature* 343.6253 (Jan. 1990), pp. 46–49. DOI: 10.1038/343046a0 (cit. on p. 48).

[Aut06] A. AUTHIER. "Introduction to the properties of tensors". In: *Physical properties of crystals*. International Union of Crystallography (IUCr), Oct. 2006, pp. 3–33. DOI: 10.1107/97809553602060000628 (cit. on p. 35).

[Avn76] Y. AVNI. "Energy spectra of X-ray clusters of galaxies". In: *Astrophysical Journal* 210 (Dec. 1976), p. 642. DOI: 10.1086/154870 (cit. on pp. 75, 93).

[Azi+10] C. AZIMONTE et al. "Polar atomic displacements in multiferroics observed via anomalous x-ray diffraction". In: *Phys. Rev. B* 81 (1 Jan. 2010), p. 012103. DOI: 10.1103/PhysRevB.81.012103 (cit. on p. 99).

[BB05] C. H. BOOTH and F. BRIDGES. "Improved self-absorption correction for fluorescence measurements of extended x-ray absorption fine-structure". In: *Physica Scripta* 2005.T115 (2005), p. 202. DOI: 10.1238/physica.topical.115a00202 (cit. on p. 45).

[BB72] F. de BERGEVIN and M. BRUNEL. "Observation of magnetic superlattice peaks by X-ray diffraction on an antiferromagnetic NiO crystal". In: *Physics Letters A* 39.2 (1972), pp. 141–142. ISSN: 0375-9601. DOI: 10.1016/0375-9601(72)91054-7 (cit. on p. 13).

[BB81] F. de BERGEVIN and M. BRUNEL. "Diffraction of X-rays by magnetic materials. I. General formulae and measurements on ferro- and ferrimagnetic compounds". In: *Acta Crystallographica Section A* 37.3 (May 1981), pp. 314–324. DOI: 10.1107/S0567739481000739 (cit. on p. 13).

[BC92] S. BRENNAN and P. L. COWAN. "A suite of programs for calculating x-ray absorption, reflection, and diffraction performance for a variety of materials at arbitrary wavelengths". In: *Review of Scientific Instruments* 63.1 (1992), pp. 850–853. DOI: 10.1063/1.1142625 (cit. on p. 48).

[BDN03] M. BENFATTO, S. DELLA LONGA, and C. R. NATOLI. "The *MXAN* procedure: a new method for analysing the XANES spectra of metalloproteins to obtain structural quantitative information". In: *Journal of Synchrotron Radiation* 10.1 (Jan. 2003), pp. 51–57. DOI: 10.1107/S0909049502018137 (cit. on p. 49).

[Beu+15] G. BEUTIER et al. "Proton configurations in the hydrogen bonds of KH_2PO_4 as seen by resonant x-ray diffraction". In: *Phys. Rev. B* 92 (21 Dec. 2015), p. 214116. DOI: 10.1103/PhysRevB.92.214116 (cit. on p. 113).

[BJ09] O. BUNĂU and Y. JOLY. "Self-consistent aspects of x-ray absorption calculations". In: *Journal of Physics: Condensed Matter* 21.34 (Aug. 2009), p. 345501. DOI: 10.1088/0953-8984/21/34/345501 (cit. on p. 49).

[Blü12] S. BLÜGEL. "A02: Scattering Theory: Born Series". In: *43rd IFF Spring School: "Scattering Methods for Condensed Matter Research: Towards Novel Applications at Future Sources"*. Ed. by M. ANGST et al. Vol. 33. Schriften des Forschungszentrums Jülich / Reihe Schlüsseltechnologien / Key Technologies. Jülich: Forschungszentrum Jülich GmbH, JCNS, PGI, ICS, IAS, Mar. 5, 2012, A2.1–A2.29. ISBN: 978-3-89336-759-7 (cit. on p. 27).

[Blu85] M. BLUME. "Magnetic scattering of x-rays (invited)". In: *Journal of Applied Physics* 57.8 (1985), pp. 3615–3618. DOI: 10.1063/1.335023 (cit. on p. 15).

[Blu94] M. BLUME. "Resonant anomalous X-ray scattering: theory and applications". In: ed. by G. MATERLIK, C. SPARKS, and K. FISCHER. North-Holland Amsterdam, 1994. Chap. Magnetic effects in anomalous dispersion. ISBN: 978-0444820259 (cit. on pp. 15, 24, 50).

[BLW92] F. BRIDGES, G. LI, and X. WANG. "Monochromator-induced glitches in EXAFS data I. Test of the model for linearly tapered samples". In: *Nuclear Instruments and Methods in Physics Research Section A: Accelerators, Spectrometers, Detectors and Associated Equipment* 320.3 (1992), pp. 548–555. ISSN: 0168-9002. DOI: 10.1016/0168-9002(92)90949-5 (cit. on p. 43).

[BPB51] J. M. BIJVOET, A. F. PEERDEMAN, and A. J. van BOMMEL. "Determination of the Absolute Configuration of Optically Active Compounds by Means of X-Rays". In: *Nature* 168.4268 (Aug. 1951), pp. 271–272. DOI: 10.1038/168271a0 (cit. on p. 12).

[Bri+11] S. N. BRITVIN et al. "Layered Hydrazinium Titanate: Advanced Reductive Adsorbent and Chemical Toolkit for Design of Titanium Dioxide Nanomaterials". en. In: *Journal of the American Chemical Society* 133.24 (June 2011), pp. 9516–9525. ISSN: 0002-7863, 1520-5126. DOI: 10.1021/ja202053q (cit. on pp. 68, 72, 115).

[Bro+01] S. BROWN et al. "Instrument developments for magnetic and high-resolution diffraction at the XMaS beamline". In: *Nuclear Instruments and Methods in Physics Research Section A: Accelerators, Spectrometers, Detectors and Associated Equipment* 467-468 (July 2001), pp. 727–732. DOI: 10.1016/s0168-9002(01)00479-x (cit. on p. 90).

[Bro+06] P. J. BROWN et al. "Intensity of diffracted intensities". In: *International Tables Online*. International Union of Crystallography (IUCr), Oct. 2006, pp. 554–595. DOI: 10.1107/97809553602060000600 (cit. on p. 48).

[Bru+02] P. BRUZZONI et al. "Kramers–Kronig transforms calculation with a fast convolution algorithm". In: *Electrochimica Acta* 48.4 (2002), pp. 341–347. ISSN: 0013-4686. DOI: 10.1016/S0013-4686(02)00677-1 (cit. on p. 25).

[Car06] N. CARRON. *An Introduction to the Passage of Energetic Particles through Matter*. Informa UK Limited, Nov. 2006. DOI: 10.1201/9781420012378 (cit. on p. 26).

[Cau56] Y. CAUCHOIS. "Distribution spectrale observee dans une region d'absorption propre de divers cristaux". In: *Comptes Rendus de l'Académie des Sciences* 242.1 (1956), pp. 100–102 (cit. on p. 13).

[Cen+09] C. CEN et al. "Oxide Nanoelectronics on Demand". In: *Science* 323.5917 (Feb. 2009), pp. 1026–1030. DOI: 10.1126/science.1168294 (cit. on p. 87).

[Cha95] C. T. CHANTLER. "Theoretical Form Factor, Attenuation, and Scattering Tabulation for Z=1–92 from E=1–10 eV to E=0.4–1.0 MeV". In: *Journal of Physical and Chemical Reference Data* 24.1 (1995), pp. 71–643. DOI: 10.1063/1.555974 (cit. on p. 48).

[CHK97] D. CULLEN, J. HUBBELL, and L. KISSEL. *EPDL97: the evaluated photo data library '97 version*. Tech. rep. Sept. 1997. DOI: 10.2172/295438 (cit. on p. 48).

[Cho04] K. J. CHOI. "Enhancement of Ferroelectricity in Strained $BaTiO_3$ Thin Films". In: *Science* 306.5698 (Nov. 2004), pp. 1005–1009. DOI: 10.1126/science.1103218 (cit. on p. 83).

[CKP30] D. COSTER, K. S. KNOL, and J. A. PRINS. "Unterschiede in der Intensität der Röntgenstrahlen-reflexion an den beiden 111-Flächen der Zinkblende". In: *Zeitschrift für Physik* 63.5-6 (May 1930), pp. 345–369. DOI: 10.1007/bf01339610 (cit. on p. 12).

[CL70] D. T. CROMER and D. LIBERMAN. "Relativistic Calculation of Anomalous Scattering Factors for X-Rays". In: *The Journal of Chemical Physics* 53.5 (1970), pp. 1891–1898. DOI: 10.1063/1.1674266 (cit. on p. 48).

[CM66] R. COLELLA and A. MERLINI. "A study of the (222) "forbidden" reflection in germanium and silicon". In: *physica status solidi (b)* 18.1 (1966), pp. 157–166. ISSN: 1521-3951. DOI: 10.1002/pssb.19660180118 (cit. on p. 104).

[Col77] S. COLLOCOTT. "Numerical solution of Kramers-Kronig transforms by a fourier method". In: *Computer Physics Communications* 13.3 (Sept. 1977), pp. 203–206. DOI: 10.1016/0010-4655(77)90014-5 (cit. on p. 25).

[Cro+97] J. O. CROSS et al. "Separated Anomalous Scattering Amplitudes for the Inequivalent Cu Sites in $YBa_2Cu_3O_{7-\delta}$ using DAFS". In: *Le Journal de Physique IV* 7.C2 (Apr. 1997), pp. C2–745–C2–747. ISSN: 1155-4339. DOI: 10.1051/jp4:1997224 (cit. on p. 57).

[Cro+98] J. O. CROSS et al. "Inclusion of local structure effects in theoretical x-ray resonant scattering amplitudes using *ab initio* x-ray-absorption spectra calculations". In: *Phys. Rev. B* 58 (17 Nov. 1998), pp. 11215–11225. DOI: 10.1103/PhysRevB.58.11215 (cit. on p. 48).

[CW93] D. COX and A. WILKINSON. "Powder diffraction studies using anomalous dispersion". In: Jan. 1993 (cit. on p. 60).

[DJN05] S. DI MATTEO, Y. JOLY, and C. R. NATOLI. "Detection of electromagnetic multipoles by x-ray spectroscopies". In: *Phys. Rev. B* 72 (14 Oct. 2005), p. 144406. DOI: 10.1103/PhysRevB.72.144406 (cit. on p. 50).

[Dmi83] V. E. DMITRIENKO. "Forbidden reflections due to anisotropic X-ray susceptibility of crystals". In: *Acta Crystallographica Section A* 39.1 (Jan. 1983), pp. 29–35. DOI: 10.1107/S0108767383000057 (cit. on p. 13).

[DO00] V. E. DMITRIENKO and E. N. OVCHINNIKOVA. "Resonant X-ray diffraction: 'forbidden' Bragg reflections induced by thermal vibrations and point defects". In: *Acta Crystallographica Section A* 56.4 (July 2000), pp. 340–347. DOI: 10.1107/S0108767300003421 (cit. on pp. 101, 102).

[DO02] V. E. DMITRIENKO and E. N. OVCHINNIKOVA. "Resonant X-Ray Diffraction: Forbidden Bragg Reflections Induced by Atomic Displacements". In: *Structural Chemistry* 13.3 (2002), pp. 397–404. ISSN: 1572-9001. DOI: 10.1023/A:1015884528271 (cit. on p. 101).

[DS96] R. J. DEJUS and M. SANCHEZ DEL RIO. "XOP: A graphical user interface for spectral calculations and x-ray optics utilities". In: *Review of Scientific Instruments* 67.9 (1996), pp. 3356–3356. DOI: 10.1063/1.1147376 (cit. on p. 42).

[Egg+06] T. EGGERT et al. "The spectral response of silicon X-ray detectors". en. In: *Nuclear Instruments and Methods in Physics Research Section A: Accelerators, Spectrometers, Detectors and Associated Equipment* 568.1 (Nov. 2006), pp. 1–11. ISSN: 01689002. DOI: 10.1016/j.nima.2006.07.011 (cit. on p. 69).

[Egg04] T. EGGERT. "Die spektrale Antwort von Silizium-Röntgendetektoren". PhD thesis. Universität München, 2004 (cit. on p. 69).

[Fab+15] F. FABRIZI et al. "Identification of inversion domains in $KTiOPO_4$ via resonant X-ray diffraction". In: *Acta Cryst Sect A* 71.4 (May 2015), pp. 361–367. DOI: 10.1107/s2053273315007238 (cit. on p. 80).

[Fei82] J. FEINBERG. "Self-pumped, continuous-wave phase conjugator using internal reflection". In: *Opt. Lett.* 7.10 (Oct. 1982), pp. 486–488. DOI: 10.1364/OL.7.000486 (cit. on p. 79).

[FKL13] W. FRIEDRICH, P. KNIPPING, and M. LAUE. "Interferenzerscheinungen bei Röntgenstrahlen". In: *Annalen der Physik* 346.10 (1913), pp. 971–988. ISSN: 1521-3889. DOI: 10.1002/andp.19133461004 (cit. on p. 12).

[Fra+95] R. FRAHM et al. "X-ray undulator beamline BW1 at DORIS III". In: *Review of Scientific Instruments* 66.2 (1995), pp. 1677–1680. DOI: 10.1063/1.1146466 (cit. on p. 69).

[Fri13] G. FRIEDEL. "Sur les symétries cristallines que peut révéler la diffraction des rayons Röntgen". In: *CR Acad Sci* 157 (1913), pp. 1533–1536 (cit. on pp. 12, 80).

[Fri20] H. FRICKE. "The K-Characteristic Absorption Frequencies for the Chemical Elements Magnesium to Chromium". In: *Phys. Rev.* 16 (3 Sept. 1920), pp. 202–215. DOI: 10.1103/PhysRev.16.202 (cit. on p. 12).

[FW68] P. A. FLEURY and J. M. WORLOCK. "Electric-Field-Induced Raman Scattering in $SrTiO_3$ and $KTaO_3$". In: *Physical Review* 174.2 (Oct. 1968), pp. 613–623. DOI: 10.1103/physrev.174.613 (cit. on p. 87).

[FWC98] R. C. FORREY, J. W. WOO, and K. CHO. "Model for Astrophysical X-Ray Absorption Fine Structure". In: *The Astrophysical Journal* 505.1 (Sept. 1998), pp. 236–243. DOI: 10.1086/306133 (cit. on p. 119).

[Gay+11] R. GAYNUTDINOV et al. "Homogeneous switching in ultrathin ferroelectric films". In: *Journal of Physics: Condensed Matter* 24.1 (Dec. 2011), p. 015902. DOI: 10.1088/0953-8984/24/1/015902 (cit. on p. 80).

[Gay+13] R. GAYNUTDINOV et al. "Polarization switching kinetics in ultrathin ferroelectric barium titanate film". en. In: *Physica B: Condensed Matter* 424 (Sept. 2013), pp. 8–12. ISSN: 09214526. DOI: 10.1016/j.physb.2013.04.056 (cit. on p. 84).

[Gla75] A. M. GLAZER. "Simple ways of determining perovskite structures". In: *Acta Cryst Sect A* 31.6 (Nov. 1975), pp. 756–762. DOI: 10.1107/s0567739475001635 (cit. on p. 95).

[Gor+16] S. GORFMAN et al. "Simultaneous resonant x-ray diffraction measurement of polarization inversion and lattice strain in polycrystalline ferroelectrics". In: *Sci. Rep.* 6 (Feb. 2016), p. 20829. DOI: 10.1038/srep20829 (cit. on pp. 80, 85).

[Gra+11] S. GRAZULIS et al. "Crystallography Open Database (COD): an open-access collection of crystal structures and platform for world-wide collaboration". In: *Nucleic Acids Research* 40.D1 (Nov. 2011), pp. D420–D427. DOI: 10.1093/nar/gkr900 (cit. on p. 99).

[Gru+05] A. GRUVERMAN et al. "Direct studies of domain switching dynamics in thin film ferroelectric capacitors". In: *Applied Physics Letters* 87.8 (Aug. 2005), p. 082902. ISSN: 0003-6951, 1077-3118. DOI: 10.1063/1.2010605 (cit. on p. 84).

[Gum+10] R. GUMENIUK et al. "Boron induced change of the Eu valence state in $EuPd_3B_x$ ($0 \leq x \leq 0.53$): A theoretical and experimental study". In: *Phys. Rev. B* 82 (23 Dec. 2010), p. 235113. DOI: 10.1103/PhysRevB.82.235113 (cit. on pp. 60, 61).

[Hae+04] J. H. HAENI et al. "Room-temperature ferroelectricity in strained $SrTiO_3$". In: *Nature* 430.7001 (Aug. 2004), pp. 758–761. DOI: 10.1038/nature02773 (cit. on p. 87).

[Hah06] T. HAHN, ed. *International Tables for Crystallography*. International Union of Crystallography, Oct. 2006. DOI: 10.1107/97809553602060000100 (cit. on p. 34).

[Han+13] J. HANZIG et al. "Migration-induced field-stabilized polar phase in strontium titanate single crystals at room temperature". In: *Phys. Rev. B* 88 (2 July 2013), p. 024104. DOI: 10.1103/PhysRevB.88.024104 (cit. on pp. 87, 94, 121).

[Han+15] J. HANZIG et al. "Dielectric to pyroelectric phase transition induced by defect migration". In: *New Journal of Physics* 17.2 (Feb. 2015), p. 023036. DOI: 10.1088/1367-2630/17/2/023036 (cit. on p. 87).

[Hel00] M. HELLIWELL. "Anomalous scattering for small-molecule crystallography". In: *J Synchrotron Radiat* 7.3 (May 2000), pp. 139–147. DOI: 10.1107/s090904950000296x (cit. on p. 48).

[HGD93] B. HENKE, E. GULLIKSON, and J. DAVIS. "X-Ray Interactions: Photoabsorption, Scattering, Transmission, and Reflection at E=50-30,000 eV, Z=1-92". In: *Atomic Data and Nuclear Data Tables* 54.2 (1993), pp. 181–342. ISSN: 0092-640X. DOI: 10.1006/adnd.1993.1013 (cit. on p. 48).

[Hig+10] M. J. HIGHLAND et al. "Polarization Switching without Domain Formation at the Intrinsic Coercive Field in Ultrathin Ferroelectric $PbTiO_3$". In: *Phys. Rev. Lett.* 105.16 (Oct. 2010). DOI: 10.1103/physrevlett.105.167601 (cit. on p. 83).

[Hil+14] J. HILHORST et al. "Full-field X-ray diffraction microscopy using polymeric compound refractive lenses". In: *Journal of Applied Crystallography* 47.6 (Dec. 2014), pp. 1882–1888. DOI: 10.1107/S1600576714021256 (cit. on p. 80).

[Hod+95] J. L. HODEAU et al. "Site selectivity of DAFS analysis on hexaferrite at Fe K edge by using both monochromatic optics and energy dispersive optics". In: *Nuclear Instruments and Methods in Physics Research Section B: Beam Inter-*

actions with Materials and Atoms 97.1-4 (May 1995), pp. 115–118. ISSN: 0168-583X. DOI: 10.1016/0168-583X(94)00365-3 (cit. on p. 57).

[Hru+13] S. O. HRUSZKEWYCZ et al. "Imaging Local Polarization in Ferroelectric Thin Films by Coherent X-Ray Bragg Projection Ptychography". In: *Physical Review Letters* 110.17 (Apr. 2013), p. 177601. DOI: 10.1103/PhysRevLett.110.177601 (cit. on p. 80).

[HT81] W. A. HENDRICKSON and M. M. TEETER. "Structure of the hydrophobic protein crambin determined directly from the anomalous scattering of sulphur". In: *Nature* 290.5802 (Mar. 1981), pp. 107–113. DOI: 10.1038/290107a0 (cit. on pp. 13, 48).

[Iev+14] A. V. IEVLEV et al. "Ionic field effect and memristive phenomena in single-point ferroelectric domain switching". In: *Nature Communications* 5 (July 2014). ISSN: 2041-1723. DOI: 10.1038/ncomms5545 (cit. on p. 84).

[IT71] Y. ISHIBASHI and Y. TAKAGI. "Note on Ferroelectric Domain Switching". In: *Journal of the Physical Society of Japan* 31.2 (Aug. 1971), pp. 506–510. DOI: 10.1143/jpsj.31.506 (cit. on p. 83).

[Ito+99] M. ITOH et al. "Ferroelectricity Induced by Oxygen Isotope Exchange in Strontium Titanate Perovskite". In: *Phys. Rev. Lett.* 82 (17 Apr. 1999), pp. 3540–3543. DOI: 10.1103/PhysRevLett.82.3540 (cit. on p. 87).

[Jac99] J. D. JACKSON. *Classical electrodynamics*. Wiley, 1999 (cit. on pp. 15, 38).

[JG03] J. JUNQUERA and P. GHOSEZ. "Critical thickness for ferroelectricity in perovskite ultrathin films". In: *Nature* 422.6931 (Apr. 2003), pp. 506–509. DOI: 10.1038/nature01501 (cit. on p. 79).

[Jol01] Y. JOLY. "X-ray absorption near-edge structure calculations beyond the muffin-tin approximation". In: *Phys. Rev. B* 63 (12 Mar. 2001), p. 125120. DOI: 10.1103/PhysRevB.63.125120 (cit. on pp. 49, 51, 111).

[Jol03] Y. JOLY. "Calculating X-ray absorption near-edge structure at very low energy". In: *Journal of Synchrotron Radiation* 10.1 (Jan. 2003), pp. 58–63. DOI: 10.1107/S0909049502017211 (cit. on p. 51).

[Jon41] R. C. JONES. "A New Calculus for the Treatment of Optical SystemsI. Description and Discussion of the Calculus". In: *J. Opt. Soc. Am.* 31.7 (July 1941), pp. 488–493. DOI: 10.1364/JOSA.31.000488 (cit. on p. 16).

[Joy+12] D. JOYNER et al. *Open Source Computer Algebra Systems: SymPy*. 3/4. New York, NY, USA: ACM, Jan. 2012, pp. 225–234. DOI: 10.1145/2110170.2110185 (cit. on p. 50).

[JP99] W. JAUCH and A. PALMER. "Anomalous zero-point motion in $SrTiO_3$: Results from γ-ray diffraction". In: *Phys. Rev. B* 60 (5 Aug. 1999), pp. 2961–2963. DOI: 10.1103/PhysRevB.60.2961 (cit. on p. 92).

[Kaw+14] T. KAWAGUCHI et al. "Revisit to diffraction anomalous fine structure". In: *J Synchrotron Radiat* 21.6 (Oct. 2014), pp. 1247–1251. DOI: 10.1107/s1600577514015148 (cit. on p. 56).

[KF96] G. KRESSE and J. FURTHMÜLLER. "Efficient iterative schemes for *ab initio* total-energy calculations using a plane-wave basis set". In: *Phys. Rev. B* 54 (16 Oct. 1996), pp. 11169–11186. DOI: 10.1103/PhysRevB.54.11169 (cit. on pp. 111, 120).

[KFM16] T. KAWAGUCHI, K. FUKUDA, and E. MATSUBARA. "Site- and phase- selective x-ray absorption spectroscopy based on phase-retrieval calculation". In: *Journal of Physics: Condensed Matter* (Dec. 2016). DOI: 10.1088/1361-648x/aa53bb (cit. on p. 117).

[KG07] S. KALININ and A. GRUVERMAN, eds. *Scanning Probe Microscopy*. Springer Nature, 2007. DOI: 10.1007/978-0-387-28668-6 (cit. on p. 85).

[KGD02a] A. KIRFEL, J. GRYBOS, and V. E. DMITRIENKO. "Phonon-electron interaction and vibration correlations in germanium within a broad temperature interval". In: *Physical Review B* 66.16 (Oct. 2002). DOI: 10.1103/physrevb.66.165202 (cit. on p. 91).

[KGD02b] A. KIRFEL, J. GRYBOS, and V. E. DMITRIENKO. "Phonon-electron interaction and vibration correlations in germanium within a broad temperature interval". en. In: *Physical Review B* 66.16 (Oct. 2002). ISSN: 0163-1829, 1095-3795. DOI: 10.1103/PhysRevB.66.165202 (cit. on p. 101).

[Kha+15] B. KHANBABAEE et al. "Using time-resolved X-ray diffraction to test the piezoelectricity of the field-stabilized polar phase in $SrTiO_3$". In: *Acta Cryst Sect A* 71.a1 (Aug. 2015), s324–s325. DOI: 10.1107/s2053273315095121 (cit. on pp. 87, 94).

[KJ99] G. KRESSE and D. JOUBERT. "From ultrasoft pseudopotentials to the projector augmented-wave method". In: *Phys. Rev. B* 59 (3 Jan. 1999), pp. 1758–1775. DOI: 10.1103/PhysRevB.59.1758 (cit. on p. 120).

[KN80] N. S. J. KENNEDY and R. J. NELMES. "Structural studies of RbH_2PO_4 in its paraelectric and ferroelectric phases". In: *Journal of Physics C: Solid State Physics* 13.26 (Sept. 1980), pp. 4841–4853. DOI: 10.1088/0022-3719/13/26/008 (cit. on pp. 104, 109).

[Kok+10] J. KOKUBUN et al. "Pure dipole-quadrupole resonant scattering induced by the p-d hybridization of atomic orbitals in anatase TiO_2". en. In: *Physical Review B* 82.20 (Nov. 2010). ISSN: 1098-0121, 1550-235X. DOI: 10.1103/PhysRevB.82.205206 (cit. on p. 50).

[Kol+10] A. M. KOLPAK et al. "Interface-Induced Polarization and Inhibition of Ferroelectricity in Epitaxial $SrTiO_3$/Si". In: *Phys. Rev. Lett.* 105 (21 Nov. 2010), p. 217601. DOI: 10.1103/PhysRevLett.105.217601 (cit. on p. 99).

[KP92] A. KIRFEL and A. PETCOV. "Anisotropy of anomalous scattering in X-ray diffraction. II. Combining polarization-dependent transmission and diffraction, and an application to partial-structure analysis". In: *Acta Crystallographica Section A* 48.3 (May 1992), pp. 247–259. DOI: 10.1107/S0108767391011509 (cit. on p. 51).

[KPE91] A. KIRFEL, A. PETCOV, and K. EICHHORN. "Anisotropy of anomalous dispersion in X-ray diffraction". In: *Acta Crystallographica Section A* 47.3 (May 1991), pp. 180–195. DOI: 10.1107/S010876739001159X (cit. on p. 51).

[Kri96] M. A. KRIVOGLAZ. *X-Ray and Neutron Diffraction in Nonideal Crystals*. Ed. by V. G. BARYAKHTAR et al. Springer Science + Business Media, 1996. DOI: 10.1007/978-3-642-74291-0 (cit. on p. 91).

[Kuh13] W. F. KUHS. "Atomic displacement parameters". In: *Physical properties of crystals*. International Union of Crystallography (IUCr), Dec. 2013, pp. 231–245. DOI: 10.1107/97809553602060000908 (cit. on p. 89).

[KV93] R. D. KING-SMITH and D. VANDERBILT. "Theory of polarization of crystalline solids". In: *Phys. Rev. B* 47 (3 Jan. 1993), pp. 1651–1654. DOI: 10.1103/PhysRevB.47.1651 (cit. on p. 120).

[Las+05] J. LASAVE et al. "Slater and Takagi defects in KH_2PO_4 from first principles". In: *Physical Review B* 72.10 (Sept. 2005). DOI: 10.1103/physrevb.72.104104 (cit. on pp. 104, 105).

[Li+06] Y. L. LI et al. "Phase transitions and domain structures in strained pseudocubic (100) $SrTiO_3$ thin films". In: *Phys. Rev. B* 73 (18 May 2006), p. 184112. DOI: 10.1103/PhysRevB.73.184112 (cit. on p. 96).

[Lic+14] C. LICHTENSTEIGER et al. "Tuning of the Depolarization Field and Nanodomain Structure in Ferroelectric Thin Films". In: *Nano Letters* 14.8 (Aug. 2014), pp. 4205–4211. DOI: 10.1021/nl404734z (cit. on p. 79).

[Lin09] I. LINDAU. "X-ray data booklet". In: *X-RAY DATA BOOKLET* (2009) (cit. on pp. 42, 44).

[LLH06] H. LIPSON, J. I. LANGFORD, and H.-C. HU. "Trigonometric intensity factors". In: *International Tables Online*. International Union of Crystallography (IUCr), Oct. 2006, pp. 596–598. DOI: 10.1107/97809553602060000601 (cit. on pp. 64, 74).

[Lov+05] S. LOVESEY et al. "Electronic properties of crystalline materials observed in X-ray diffraction". In: *Physics Reports* 411.4 (2005), pp. 233–289. ISSN: 0370-1573. DOI: 10.1016/j.physrep.2005.01.003 (cit. on p. 50).

[LSP03] V. LUCARINI, J. J. SAARINEN, and K.-E. PEIPONEN. "Multiply subtractive generalized Kramers–Kronig relations: Application on third-harmonic generation susceptibility on polysilane". en. In: *The Journal of Chemical Physics* 119.21 (2003), p. 11095. ISSN: 00219606. DOI: 10.1063/1.1623477 (cit. on p. 25).

[M H04] M. HELLENBRANDT. "The Inorganic Crystal Structure Database (ICSD) – Present and Future". In: *Crystallography Reviews* 10.1 (Jan. 2004), pp. 17–22. DOI: 10.1080/08893110410001664882 (cit. on p. 123).

[Mat+99] W. MATZ et al. "ROBL – a CRG beamline for radiochemistry and materials research at the ESRF". In: *Journal of Synchrotron Radiation* 6.6 (Nov. 1999), pp. 1076–1085. DOI: 10.1107/S0909049599010663 (cit. on p. 90).

[Mat12] S. D. MATTEO. "Resonant x-ray diffraction: multipole interpretation". In: *Journal of Physics D: Applied Physics* 45.16 (Mar. 2012), p. 163001. DOI: 10.1088/0022-3727/45/16/163001 (cit. on p. 50).

[MC01] P. MACCHI and P. COPPENS. "Relativistic analytical wave functions and scattering factors for neutral atoms beyond Kr and for all chemically important ions up to I-". In: *Acta Cryst Sect A* 57.6 (Oct. 2001), pp. 656–662. DOI: 10.1107/s0108767301010182 (cit. on p. 48).

[Mer56] W. J. MERZ. "Switching Time in Ferroelectric $BaTiO_3$ and Its Dependence on Crystal Thickness". en. In: *Journal of Applied Physics* 27.8 (1956), p. 938. ISSN: 00218979. DOI: 10.1063/1.1722518 (cit. on p. 84).

[Mey+04] D. MEYER et al. "An electrical field-induced structural effect in strontium titanate at room temperature". In: *Applied Physics A* 80.3 (2004), pp. 515–522. ISSN: 1432-0630. DOI: 10.1007/s00339-004-3063-6 (cit. on p. 87).

[MHM04] S. MATTAUCH, G. HEGER, and K. H. MICHEL. "High resolution neutron and X-ray diffraction studies as a function of temperature and electric field of the ferroelectric phase transition of RDP". In: *Crystal Research and Technology* 39.12 (Dec. 2004), pp. 1027–1054. DOI: 10.1002/crat.200410289 (cit. on pp. 104, 105).

[Moe+12] P. MOETAKEF et al. "Carrier-Controlled Ferromagnetism in $SrTiO_3$". In: *Phys. Rev. X* 2.2 (June 2012). DOI: 10.1103/physrevx.2.021014 (cit. on p. 87).

[MP00] D. C. MEYER and P. PAUFLER. "Refinement of free structure parameters of a thin film when only one reflection is available". In: *Journal of Applied Crystallography* 33.2 (Apr. 2000), pp. 252–258. DOI: 10.1107/S0021889899016039 (cit. on p. 99).

[MS25] H. MARK and L. SZILARD. "Ein einfacher Versuch zur Auffindung eines selektiven Effektes bei der Zerstreuung von Röntgenstrahlen". In: *Zeitschrift für Physik* 33.1 (Dec. 1925), pp. 688–691. DOI: 10.1007/bf01328354 (cit. on p. 12).

[MS60] R. C. MILLER and A. SAVAGE. "Motion of 180° Domain Walls in Metal Electroded Barium Titanate Crystals as a Function of Electric Field and Sample Thickness". en. In: *Journal of Applied Physics* 31.4 (1960), p. 662. ISSN: 00218979. DOI: 10.1063/1.1735663 (cit. on p. 84).

[Muk+10a] E. K. MUKHAMEDZHANOV et al. "Resonant diffraction of synchrotron radiation in rubidium dihydrophosphate crystals". In: *Crystallography Reports* 55.2 (Mar. 2010), pp. 174–181. DOI: 10.1134/s1063774510020021 (cit. on pp. 104, 106).

[Muk+10b] E. K. MUKHAMEDZHANOV et al. "Resonant diffraction of synchrotron radiation in rubidium dihydrophosphate crystals". en. In: *Crystallography Reports* 55.2 (Mar. 2010), pp. 174–181. ISSN: 1063-7745, 1562-689X. DOI: 10.1134/S1063774510020021 (cit. on p. 105).

[Nel88] R. J. NELMES. "On the structural evidence for a direct proton tunnelling effect in the KH_2PO_4-type transition". In: *Journal of Physics C: Solid State Physics* 21.24 (Aug. 1988), pp. L881–L886. DOI: 10.1088/0022-3719/21/24/001 (cit. on p. 104).

[New14] M. NEWVILLE. "Fundamentals of XAFS". In: *Reviews in Mineralogy and Geochemistry* 78.1 (Jan. 2014), pp. 33–74. DOI: 10.2138/rmg.2014.78.2 (cit. on p. 36).

[New98] M. NEWVILLE. *DIFFKK*. 1998. URL: http://cars9.uchicago.edu/dafs/diffkk/ (cit. on p. 48).

[Ovc+10] E. N. OVCHINNIKOVA et al. "Numerical simulation of the forbidden Bragg reflection spectra observed in ZnO". In: *Journal of Physics: Condensed Matter* 22.35 (Sept. 2010), p. 355404. ISSN: 0953-8984, 1361-648X. DOI: 10.1088/0953-8984/22/35/355404 (cit. on p. 101).

[Pal+12] H. PALANCHER et al. "X-ray resonant powder diffraction". In: *The European Physical Journal Special Topics* 208.1 (2012), pp. 275–289. ISSN: 1951-6401. DOI: 10.1140/epjst/e2012-01624-1 (cit. on p. 60).

[Pao14] L. PAOLASINI. "Resonant and magnetic X-ray diffraction by polarized synchrotron radiation". In: *École thématique de la Société Française de la Neutronique* 13 (2014). Ed. by V. SIMONET et al., p. 03002. DOI: 10.1051/sfn/20141303002 (cit. on p. 50).

[PBE96] J. P. PERDEW, K. BURKE, and M. ERNZERHOF. "Generalized Gradient Approximation Made Simple". In: *Phys. Rev. Lett.* 77 (18 Oct. 1996), pp. 3865–3868. DOI: 10.1103/PhysRevLett.77.3865 (cit. on p. 120).

[Pee74] P. S. PEERCY. "Evaluation of the coupled proton—optic-mode model for KH_2PO_4 and RbH_2PO_4". In: *Physical Review B* 9.11 (June 1974), pp. 4868–4871. DOI: 10.1103/physrevb.9.4868 (cit. on p. 104).

[Pic+93] I. J. PICKERING et al. "Diffraction anomalous fine structure: a new technique for probing local atomic environment". In: *Journal of the American Chemical Society* 115.14 (1993), pp. 6302–6311. DOI: 10.1021/ja00067a052 (cit. on pp. 53, 59).

[Pol+12] M. J. POLKING et al. "Ferroelectric order in individual nanometre-scale crystals". In: *Nature Materials* 11.8 (July 2012), pp. 700–709. DOI: 10.1038/nmat3371 (cit. on p. 79).

[Pot+84] W. POTZEL et al. "Temperature dependence of hyperfine interactions and of anisotropy of recoil-free fraction: A Mössbauer study of the 93.3-keV resonance of ^{67}Zn in single crystals of zinc metal". In: *Phys. Rev. B* 30 (9 Nov. 1984), pp. 4980–4988. DOI: 10.1103/PhysRevB.30.4980 (cit. on p. 91).

[Pro+99] M. G. PROIETTI et al. "Diffraction-anomalous-fine-structure spectroscopy applied to the study of III-V strained semiconductors". In: *Phys. Rev. B* 59 (8 Feb. 1999), pp. 5479–5492. DOI: 10.1103/PhysRevB.59.5479 (cit. on p. 53).

[PWB98] K. F. PALMER, M. Z. WILLIAMS, and B. A. BUDDE. "Multiply subtractive Kramers–Kronig analysis of optical data". In: *Appl. Opt.* 37.13 (May 1998), pp. 2660–2673. DOI: 10.1364/AO.37.002660 (cit. on p. 25).

[RA00] J. J. REHR and R. C. ALBERS. "Theoretical approaches to x-ray absorption fine structure". In: *Rev. Mod. Phys.* 72 (3 July 2000), pp. 621–654. DOI: 10.1103/RevModPhys.72.621 (cit. on p. 48).

[Ree+04] S. J. van REEUWIJK et al. "Polarization switching in $BaTiO_3$ thin films measured by X-ray diffraction exploiting anomalous dispersion". In: *Journal of Applied Crystallography* 37.2 (Apr. 2004), pp. 193–199. DOI: 10.1107/S0021889803028395 (cit. on pp. 83, 85, 99).

[Reh+10] J. J. REHR et al. "Parameter-free calculations of X-ray spectra with FEFF9". In: *Phys. Chem. Chem. Phys.* 12 (21 2010), pp. 5503–5513. DOI: 10.1039/B926434E (cit. on p. 49).

[Ren37] M. RENNINGER. "„Umweganregung", eine bisher unbeachtete Wechselwirkungserscheinung bei Raumgitterinterferenzen". In: *Zeitschrift für Physik* 106.3 (1937), pp. 141–176. ISSN: 0044-3328. DOI: 10.1007/BF01340315 (cit. on p. 96).

[Rey86] R. C. REYNOLDS. "The Lorentz-Polarization Factor and Preferred Orientation in Oriented Clay Aggregates". In: *Clays and Clay Minerals* 34.4 (1986), pp. 359–367. DOI: 10.1346/ccmn.1986.0340402 (cit. on p. 63).

[Ric+14] C. RICHTER et al. "Mechanisms of the paraelectric to ferroelectric phase transition in RbH_2PO_4 probed by purely resonant x-ray diffraction". In: *Physical Review B* 89.9 (Mar. 2014). DOI: 10.1103/physrevb.89.094110 (cit. on p. 111).

[Ric10] C. RICHTER. "Stabilität von Mo/B_4C-Multilagenspiegeln fär Synchrotronstrahlung und resonante Röntgenstreuung an defekt- und kristallfeldinduzierten Elektronendichteanisotropien in Rutil und $BaTiO_3$". TU Freiberg, Diplomarbeit, 2010. Dipl. TU Freiberg, 2010, pp. 1–95 (cit. on pp. 15, 26).

[Ric16a] C. RICHTER. *pyasf - symbolic computing of anisotropic resonant scattering factor written in sympy*. 2016. URL: https://github.com/carichte/pyasf (cit. on pp. 50, 106, 122).

[Ric16b] C. RICHTER. *rexs - toolkit for evaluation of resonant x-ray scattering measurements*. 2016. URL: https://github.com/carichte/rexs (cit. on pp. 46, 49, 53).

[Rie69] H. M. RIETVELD. "A profile refinement method for nuclear and magnetic structures". In: *Journal of Applied Crystallography* 2.2 (June 1969), pp. 65–71. DOI: 10.1107/S0021889869006558 (cit. on p. 68).

[Roe65] D. M. ROESSLER. "Kramers-Kronig analysis of reflection data". In: *British Journal of Applied Physics* 16.8 (Aug. 1965), pp. 1119–1123. DOI: 10.1088/0508-3443/16/8/310 (cit. on p. 56).

[Rön98] W. C. RÖNTGEN. "Ueber eine neue Art von Strahlen". In: *Annalen der Physik* 300.1 (1898), pp. 1–11. ISSN: 1521-3889. DOI: 10.1002/andp.18983000102 (cit. on p. 12).

[RS08] R. RAMESH and D. G. SCHLOM. "Whither Oxide Electronics?" In: *MRS Bull.* 33.11 (Nov. 2008), pp. 1006–1014. DOI: 10.1557/mrs2008.220 (cit. on p. 87).

[Sas89] S. SASAKI. "Numerical tables of anomalous scattering factors calculated by the Cromer and Liberman's method". In: *KEK Report 88-14* (Feb. 1989) (cit. on pp. 21, 48).

[SC98] Z. SU and P. COPPENS. "Nonlinear Least-Squares Fitting of Numerical Relativistic Atomic Wave Functions by a Linear Combination of Slater-Type Functions for Atoms withZ= 1–36". In: *Acta Cryst Sect A* 54.5 (Sept. 1998), pp. 646–652. DOI: 10.1107/s0108767398003390 (cit. on p. 48).

[Sch07] F. SCHWABL. *Quantenmechanik (QM I)*. Springer-Lehrbuch. Springer Berlin Heidelberg, 2007. ISBN: 9783662223758. DOI: 10.1007/978-3-540-73675-2 (cit. on pp. 16, 17).

[Sch49] J. SCHWINGER. "On the Classical Radiation of Accelerated Electrons". In: *Phys. Rev.* 75 (12 June 1949), pp. 1912–1925. DOI: 10.1103/PhysRev.75.1912 (cit. on p. 39).

[SHC64] J. F. SCHOOLEY, W. R. HOSLER, and M. L. COHEN. "Superconductivity in Semiconducting $SrTiO_3$". In: *Phys. Rev. Lett.* 12.17 (Apr. 1964), pp. 474–475. DOI: 10.1103/physrevlett.12.474 (cit. on p. 87).

[SI96] H. SUGIMOTO and S. IKEDA. "Proton transfer in hydrogen-bonded crystalline". In: *Journal of Physics: Condensed Matter* 8.5 (Jan. 1996), pp. 603–618. DOI: 10.1088/0953-8984/8/5/010 (cit. on p. 104).

[Sla41] J. C. SLATER. "Theory of the Transition in KH_2PO_4". In: *The Journal of Chemical Physics* 9.1 (1941), p. 16. DOI: 10.1063/1.1750821 (cit. on p. 105).

[Sor+94] L. B. SORENSEN et al. "Diffraction anomalous fine structure: unifying x-ray diffraction and x-ray absorption with DAFS". In: *Resonant Anomalous X-Ray Scattering: Theory and Applications*. Ed. by G. MATERLIK, C. J. SPARKS, and K. FISCHER. Amsterdam: Elsevier Science, North-Holland, 1994, pp. 389–420 (cit. on p. 119).

[SP89] J. F. SCOTT and C. A. PAZ DE ARAUJO. "Ferroelectric Memories". In: *Science* 246.4936 (1989), pp. 1400–1405. ISSN: 0036-8075. DOI: 10.1126/science.246.4936.1400 (cit. on p. 79).

[SS65] W. C. STOECKER and J. W. STARBUCK. "Effect of Soller Slits on X-Ray Intensity in a Modern Diffractometer". In: *Review of Scientific Instruments* 36.11 (1965), pp. 1593–1598. DOI: 10.1063/1.1719399 (cit. on p. 69).

[Str+13] J. STREMPFER et al. "Resonant scattering and diffraction beamline P09 at PETRA-III". In: *Journal of Synchrotron Radiation* 20.4 (July 2013), pp. 541–549. DOI: 10.1107/S0909049513009011 (cit. on p. 108).

[Tak48] Y. TAKAGI. "Theory of the Transition in KH_2PO_4. (I)". In: *Journal of the Physical Society of Japan* 3.4 (July 1948), pp. 271–272. DOI: 10.1143/jpsj.3.271 (cit. on p. 105).

[Tan+04] P. TANG et al. "Electrooptic modulation up to 40 GHz in a barium titanate thin film waveguide modulator". In: *Opt. Express* 12.24 (2004), p. 5962. DOI: 10.1364/opex.12.005962 (cit. on p. 79).

[Tan+13] S. TAN et al. "Interface-induced superconductivity and strain-dependent spin density waves in FeSe/$SrTiO_3$ thin films". In: *Nature Materials* 12.7 (May 2013), pp. 634–640. DOI: 10.1038/nmat3654 (cit. on p. 79).

[Tan15] D. B. TANNER. "Use of x-ray scattering functions in Kramers-Kronig analysis of reflectance". In: *Phys. Rev. B* 91 (3 Jan. 2015), p. 035123. DOI: 10.1103/PhysRevB.91.035123 (cit. on p. 56).

[TCF10] A. K. TAGANTSEV, L. E. CROSS, and J. FOUSEK. *Domains in Ferroic Crystals and Thin Films*. Springer Nature, 2010. DOI: 10.1007/978-1-4419-1417-0 (cit. on p. 80).

[TG13] E. Y. TSYMBAL and A. GRUVERMAN. "Ferroelectric tunnel junctions: Beyond the barrier". en. In: *Nature Materials* 12.7 (July 2013), pp. 602–604. ISSN: 1476-1122. DOI: 10.1038/nmat3669 (cit. on p. 80).

[Tom92] P. E. TOMASZEWSKI. "Structural phase transitions in crystals. I. Database". In: *Phase Transitions* 38.3 (May 1992), pp. 127–220. DOI: 10.1080/01411599208222899 (cit. on p. 90).

[Tru+96] K. N. TRUEBLOOD et al. "Atomic Dispacement Parameter Nomenclature. Report of a Subcommittee on Atomic Displacement Parameter Nomenclature". In: *Acta Crystallographica Section A* 52.5 (Sept. 1996), pp. 770–781. DOI: 10.1107/S0108767396005697 (cit. on p. 34).

[TT85] D. H. TEMPLETON and L. K. TEMPLETON. "Tensor X-ray optical properties of the bromate ion". In: *Acta Crystallographica Section A* 41.2 (Mar. 1985), pp. 133–142. DOI: 10.1107/S0108767385000277 (cit. on p. 13).

[VD28] L. VEGARD and H. DALE. "VIII. Untersuchungen über Mischkristalle und Legierungen". In: *Zeitschrift für Kristallographie - Crystalline Materials* 67.1-6 (Jan. 1928). DOI: 10.1524/zkri.1928.67.1.148 (cit. on p. 61).

[Ved+98] R. V. VEDRINSKII et al. "Pre-edge fine structure of the 3d atom K x-ray absorption spectra and quantitative atomic structure determinations for ferroelectric perovskite structure crystals". In: *Journal of Physics: Condensed Matter* 10.42 (Oct. 1998), pp. 9561–9580. DOI: 10.1088/0953-8984/10/42/021 (cit. on p. 94).

[Viz+03] G. VIZDRIK et al. "Kinetics of ferroelectric switching in ultrathin films". en. In: *Physical Review B* 68.9 (Sept. 2003). ISSN: 0163-1829, 1095-3795. DOI: 10.1103/PhysRevB.68.094113 (cit. on p. 83).

[Wan+09] R. V. WANG et al. "Reversible Chemical Switching of a Ferroelectric Film". In: *Phys. Rev. Lett.* 102 (4 Jan. 2009), p. 047601. DOI: 10.1103/PhysRevLett.102.047601 (cit. on p. 83).

[Wat14] B. WATTS. "Calculation of the Kramers-Kronig transform of X-ray spectra by a piecewise Laurent polynomial method". en. In: *Optics Express* 22.19 (Sept. 2014), p. 23628. ISSN: 1094-4087. DOI: 10.1364/OE.22.023628 (cit. on p. 25).

[Wil96] K. WILLE. "Synchrotronstrahlung". In: *Physik der Teilchenbeschleuniger und Synchrotronstrahlungsquellen: Eine Einführung*. Wiesbaden: Vieweg+Teubner Verlag, 1996, pp. 35–49. ISBN: 978-3-663-11039-2. DOI: 10.1007/978-3-663-11039-2_2 (cit. on pp. 38–40).

[Woi+07] J. C. WOICIK et al. "Ferroelectric distortion in $SrTiO_3$ thin films on Si(001) by x-ray absorption fine structure spectroscopy: Experiment and first-principles calculations". In: *Phys. Rev. B* 75 (14 Apr. 2007), p. 140103. DOI: 10.1103/PhysRevB.75.140103 (cit. on p. 94).

[Won06] H. WONDRATSCHEK. "Basic concepts". In: *Space-group symmetry*. International Union of Crystallography (IUCr), Oct. 2006, pp. 720–725. DOI: 10.1107/97809553602060000514 (cit. on p. 34).

[YHK02] T. YAMANAKA, N. HIRAI, and Y. KOMATSU. "Structure change of $Ca_{1-x}Sr_xTiO_3$ perovskite with composition and pressure". In: *American Mineralogist* 87.8-9 (Aug. 2002), pp. 1183–1189. DOI: 10.2138/am-2002-8-917 (cit. on p. 91).

[YZ14] V. YA. SHUR and P. S. ZELENOVSKIY. "Micro- and nanodomain imaging in uniaxial ferroelectrics: Joint application of optical, confocal Raman, and piezoelectric force microscopy". en. In: *Journal of Applied Physics* 116.6 (Aug. 2014), p. 066802. ISSN: 0021-8979, 1089-7550. DOI: 10.1063/1.4891397 (cit. on p. 80).

[Zen+12] A. ZENKEVICH et al. "Pulsed laser deposition of ultrathin $BaTiO_3$/Fe bi-layers: Structural characterization and piezoelectric response". en. In: *Thin Solid Films* 520.14 (May 2012), pp. 4586–4589. ISSN: 00406090. DOI: 10.1016/j.tsf.2011.10.188 (cit. on p. 83).

[Zen+13] A. ZENKEVICH et al. "Electronic band alignment and electron transport in Cr/$BaTiO_3$/Pt ferroelectric tunnel junctions". In: *Applied Physics Letters* 102.6 (2013), p. 062907. DOI: 10.1063/1.4792525 (cit. on p. 80).

[Zen+14] A. ZENKEVICH et al. "Giant bulk photovoltaic effect in thin ferroelectric $BaTiO_3$ films". In: *Physical Review B* 90.16 (Oct. 2014). DOI: 10.1103/physrevb.90.161409 (cit. on pp. 80, 83).

[Zha+15] W. ZHANG et al. "Multifunctional, self-assembled oxide nanocomposite thin films and devices". In: *MRS Bull.* 40.09 (Sept. 2015), pp. 736–745. DOI: 10.1557/mrs.2015.198 (cit. on p. 79).

Publications as main or coauthor

[Han+15a] F. HANZIG et al. "Crystallization dynamics and interface stability of strontium titanate thin films on silicon". In: *J Appl Cryst* 48.2 (Mar. 2015), pp. 393–400. DOI: 10.1107/s160057671500240x.

[Han+15b] J. HANZIG et al. "Dielectric to pyroelectric phase transition induced by defect migration". In: *New Journal of Physics* 17.2 (Feb. 2015), p. 023036. DOI: 10.1088/1367-2630/17/2/023036.

[Kha+16] B. KHANBABAEE et al. "Large piezoelectricity in electric-field modified single crystals of SrTiO3". In: *Applied Physics Letters* 109.22 (Nov. 2016), p. 222901. DOI: 10.1063/1.4966892.

[Nen+14] M. NENTWICH et al. "Evaluation of structure models of Ho_2PdSi_3 using DAFS, inter alia at a satellite reflection". In: *J. Phys.: Conf. Ser.* 519 (May 2014), p. 012011. DOI: 10.1088/1742-6596/519/1/012011.

[Nen+16] M. NENTWICH et al. "Analysis of modulated Ho_2PdSi_3 crystal structure at Pd-K and Ho-L absorption edges using resonant elastic X-scattering". In: *Journal of Physics: Condensed Matter* 28.6 (2016), p. 066002.

[Ric+14] C. RICHTER et al. "Mechanisms of the paraelectric to ferroelectric phase transition in RbH_2PO_4 probed by purely resonant x-ray diffraction". In: *Physical Review B* 89.9 (2014), p. 094110. DOI: 10.1103/physrevb.89.094110.

[Ric+16] C. RICHTER et al. "Picometer polar displacements in $SrTiO_3$ determined by resonantly suppressed X-ray diffraction". In: *submitted* (2016).

[Stö+14] H. STÖCKER et al. "Surface-near modifications of $SrTiO_3$ local symmetry due to nitrogen implantation investigated by grazing incidence XANES". In: *Scripta Materialia* 86 (Sept. 2014), pp. 1–4. DOI: 10.1016/j.scriptamat.2014.02.014.

[Stö+16] H. STÖCKER et al. "Strontium titanate: From symmetry changes to functionality". In: *Crystal Research and Technology* (2016). ISSN: 1521-4079. DOI: 10.1002/crat.201600222.

[Zsc+14] M. ZSCHORNAK et al. "Probing a crystal's short-range structure and local orbitals by Resonant X-ray Diffraction methods". In: *Crystal Research and Technology* 49.1 (Jan. 2014), pp. 43–54. DOI: 10.1002/crat.201300430.